THE CERN LARGE HADRON COLLIDER: ACCELERATOR AND EXPERIMENTS

The TOTEM Experiment at the CERN Large Hadron Collider

The TOTEM Collaboration

ABSTRACT: The TOTEM Experiment will measure the total pp cross-section with the luminosity-independent method and study elastic and diffractive scattering at the LHC. To achieve optimum forward coverage for charged particles emitted by the pp collisions in the interaction point IP5, two tracking telescopes, T1 and T2, will be installed on each side in the pseudorapidity region $3.1 \leq |\eta| \leq 6.5$, and Roman Pot stations will be placed at distances of ± 147 m and ± 220 m from IP5. Being an independent experiment but technically integrated into CMS, TOTEM will first operate in standalone mode to pursue its own physics programme and at a later stage together with CMS for a common physics programme. This article gives a description of the TOTEM apparatus and its performance.

Keywords: Gaseous detectors; Solid state detectors; Particle tracking detectors; Analogue electronic circuits; Data acquisition circuits; Data acquisition concepts; Detector control systems; Digital electronic circuits; Electronic detector readout concepts; Electronic detector readout concepts; Front-end electronics for detector readout; Modular electronics; Optical detector readout concepts; Trigger concepts and systems; VLSI circuits; Detector cooling and thermo-stabilization; Detector design and construction; Overall mechanics design.

The TOTEM Collaboration

G. Anelli,[1] G. Antchev,[1] P. Aspell,[1] V. Avati,[1,9] M.G. Bagliesi,[5] V. Berardi,[4] M. Berretti,[5]
V. Boccone,[2] U. Bottigli,[5] M. Bozzo,[2] E. Brücken,[6] A. Buzzo,[2] F. Cafagna,[4] M. Calicchio,[4]
F. Capurro,[2] M.G. Catanesi,[4] P.L. Catastini,[5] R. Cecchi,[5] S. Cerchi,[2] R. Cereseto,[2]
M.A. Ciocci,[5] S. Cuneo,[2] C. Da Già,[11] E. David,[1] M. Deile,[1] E. Dimovasili,[1,9] M. Doubrava,[10]
K. Eggert,[1] V. Eremin,[12] F. Ferro,[2] A. Foussat,[1] M. Galuška,[10] F. Garcia,[6] F. Gherarducci,[5]
S. Giani,[1] V. Greco,[5] J. Hasi,[11] F. Haug,[1] J. Heino,[6] T. Hilden,[6] P. Jarron,[1] C. Joram,[1]
J. Kalliopuska,[6] J. Kaplon,[1] J. Kašpar,[1,7] V. Kundrát,[7] K. Kurvinen,[6] J.M. Lacroix,[1]
S. Lami,[5] G. Latino,[5] R. Lauhakangas,[6] E. Lippmaa,[8] M. Lokajíček,[7] M. Lo Vetere,[2]
F. Lucas Rodriguez,[1] D. Macina,[1] M. Macrí,[2] C. Magazzù,[5] G. Magazzù,[5] A. Magri,[2]
G. Maire,[1] A. Manco,[2] M. Meucci,[5] S. Minutoli,[2] A. Morelli,[2] P. Musico,[2] M. Negri,[2]
H. Niewiadomski,[1,9] E. Noschis,[1] G. Notarnicola,[4] E. Oliveri,[5] F. Oljemark,[6] R. Orava,[6]
M. Oriunno,[1] A.-L. Perrot,[1] K. Österberg,[6] R. Paoletti,[5] E. Pedreschi,[5] J. Petäjäjärvi,[6]
P. Pollovio,[2] M. Quinto,[4] E. Radermacher,[1] E. Radicioni,[4] S. Rangod,[1] F. Ravotti,[1] G. Rella,[4]
E. Robutti,[2] L. Ropelewski,[1] G. Ruggiero,[1] A. Rummel,[8] H. Saarikko,[6] G. Sanguinetti,[5]
A. Santroni,[2] A. Scribano,[5] G. Sette,[2] W. Snoeys,[1] F. Spinella,[5] P. Squillacioti,[5] A. Ster,[13]
C. Taylor,[3] A. Tazzioli,[5] D. Torazza,[2] A. Trovato,[2] A. Trummal,[8] N. Turini,[5] V. Vacek,[1,10]
N. Van Remortel,[6] V. Vinš,[10] S. Watts,[11] J. Whitmore,[9] and J. Wu[1]

[1]CERN, Genève, Switzerland

[2]Università di Genova and Sezione INFN, Genova, Italy

[3]Case Western Reserve University, Dept. of Physics, Cleveland, OH, U.S.A.

[4]INFN Sezione di Bari and Politecnico di Bari, Bari, Italy

[5]INFN Sezione di Pisa and Università di Siena, Italy

[6]Helsinki Institute of Physics and Department of Physical Sciences, University of Helsinki, Finland

[7]Institute of Physics of the Academy of Sciences of the Czech Republic, Praha, Czech Republic

[8]National Institute of Chemical Physics and Biophysics NICPB, Tallinn, Estonia

[9]Penn State University, Dept. of Physics, University Park, PA, U.S.A.

[10]On leave from Czech Technical University, Prague, Czech Republic

[11]Brunel University, Uxbridge, UK; now at the University of Manchester, U.K.

[12]On leave from Ioffe Physico-Technical Institute,
Polytechnicheskaya Str. 26, 194021 St-Petersburg, Russian Federation

[13]Individual participant from MTA KFKI RMKI, Budapest, Hungary

Corresponding author: Mario Deile (Mario.Deile@cern.ch)

Contents

Chapter 1

Introduction

The TOTEM experiment [1] — small in size compared to the others at the LHC — is dedicated to the measurement of the total proton-proton cross-section with the luminosity-independent method based on the Optical Theorem, which requires a detailed study of the elastic scattering cross-section down to a squared four-momentum transfer of $|t| \sim 10^{-3}\,\mathrm{GeV}^2$ and the measurement of the total inelastic rate. Furthermore, TOTEM's physics programme aims at a deeper understanding of the proton structure by studying elastic scattering with large momentum transfers, and via a comprehensive menu of diffractive processes — partly in cooperation with CMS [2], located at the same interaction point, IP5. Hence the TOTEM collaboration focusses on physics complementary to the programmes of the general-purpose experiments at the LHC, and therefore had to invest heavily in the design of detectors that will be capable of meeting the challenge of triggering and recording events in the very forward region. To perform these measurements, TOTEM requires a good acceptance for particles produced at very small angles with respect to the beam. TOTEM's coverage in the pseudo-rapidity range of $3.1 \leq |\eta| \leq 6.5$ ($\eta = -\ln \tan \frac{\theta}{2}$) on both sides of the interaction point is accomplished by two telescopes for inelastically produced charged particles (figure 1.1), and complemented by detectors in special movable beam-pipe insertions — so-called Roman Pots ("RP") — placed at about 147 m and 220 m from the interaction point, designed to detect leading protons at merely a few mm from the beam centre (figure 1.2).

The telescope closest to the interaction point (T1, centered at $z = 9\,\mathrm{m}$) consists of Cathode Strip Chambers CSC (section 5.2), while the second one (T2, centered at 13.5 m) exploits Gas Electron Multipliers GEM (section 5.3). The proton detectors in the Roman Pots (chapter 4) are silicon devices designed by TOTEM with the specific objective of reducing the insensitive area at the edge facing the beam to only a few tens of microns. High efficiency up to the physical detector border is an essential feature in view of maximising the experiment's acceptance for protons scattered elastically or diffractively at polar angles down to a few microradians at the IP. To measure protons at the lowest possible emission angles, special beam optics have been conceived to optimise proton detection in terms of acceptance and resolution (chapter 3).

The read-out of all TOTEM subsystems is based on the custom-developed digital VFAT chip with trigger capability (chapter 7). The data acquisition system (chapter 9) is designed to be compatible with the CMS DAQ to make common data taking possible at a later stage.
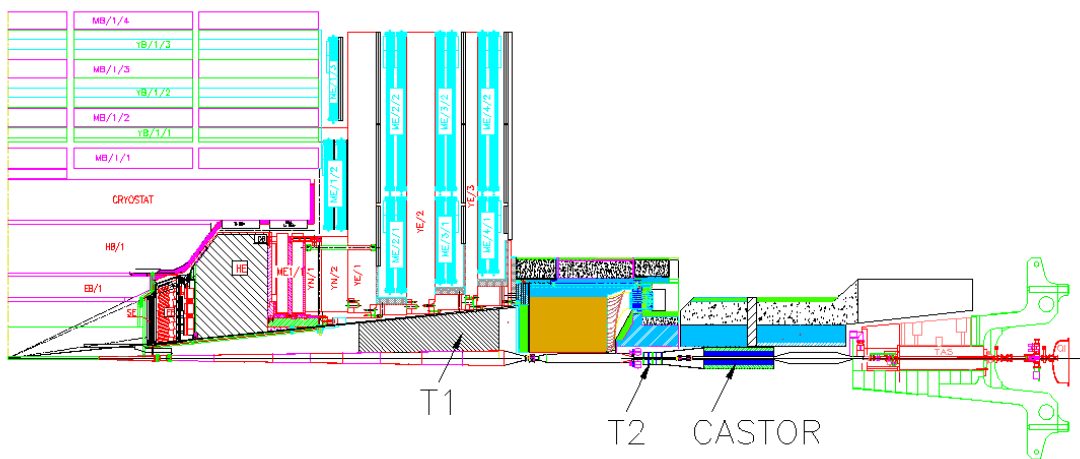
Figure 1.1: The TOTEM forward trackers T1 and T2 embedded in the CMS detector together with the planned CMS forward calorimeter CASTOR.
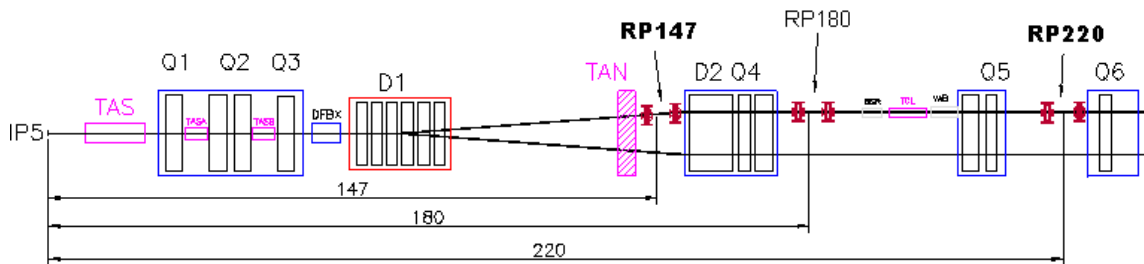
Figure 1.2: The LHC beam line on one side of interaction point IP5 and the TOTEM Roman Pots at distances of about 147 m (RP147) and 220 m (RP220). RP180 at 180 m is another possible location but presently not equipped.

Chapter 2

Physics objectives

The TOTEM apparatus with its unique coverage for charged particles at high rapidities (figure 2.1, left) is the ideal tool for studying forward phenomena, including elastic and diffractive scattering. Furthermore, energy flow and particle multiplicity of inelastic events peak in the forward region (figure 2.1 right; $\eta = 3$ corresponds to a polar angle $\theta = 100$ mrad.). About 99.5% of all non-diffractive minimum bias events and 84% of all diffractive events have charged particles within the acceptance of T1 or T2 and are thus triggerable with these detectors.

An important application is the luminosity-independent measurement of the total cross-section based on the Optical Theorem.
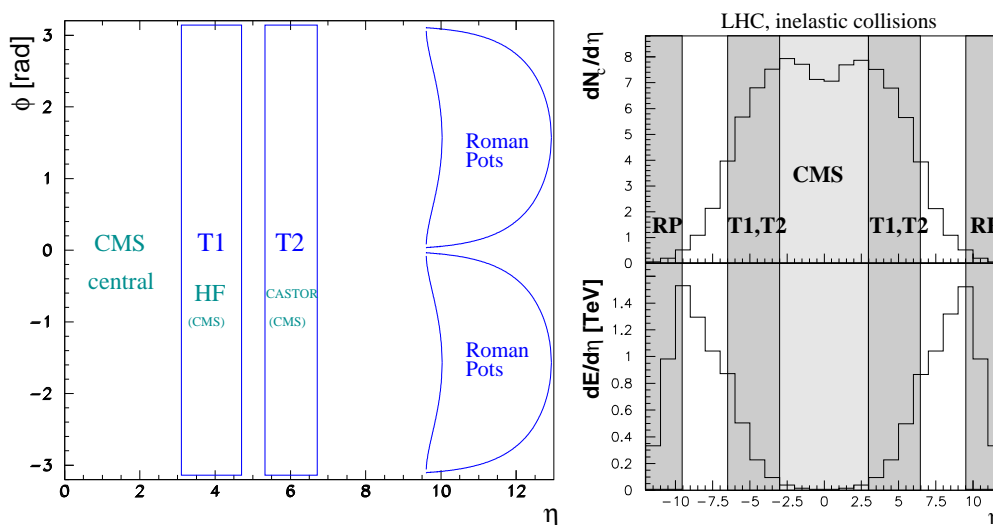
Figure 2.1: Left: coverage of different detectors in the pseudorapidity (η) - azimuthal angle (ϕ) plane. Right: charged particle multiplicity and energy flow as a function of pseudorapidity for inelastic events at $\sqrt{s} = 14$ TeV.
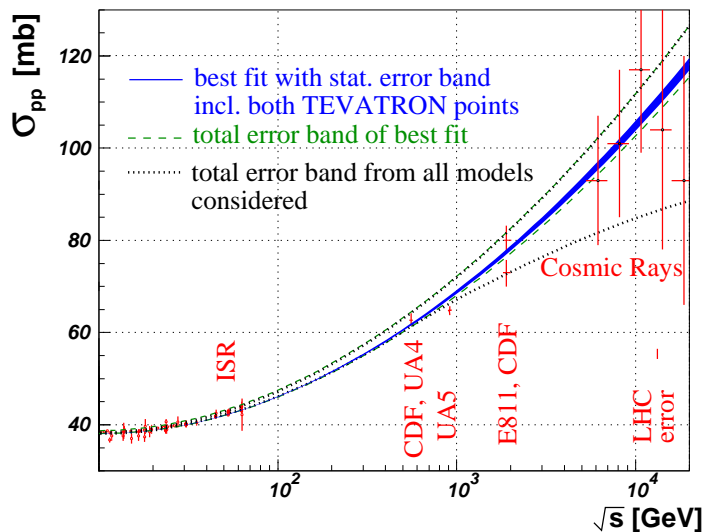
Figure 2.2: Fits from the COMPETE collaboration [5] to all available pp and $p\bar{p}$ scattering data with statistical (blue solid) and total (green dashed) error bands, the latter taking into account the discrepancy of the two Tevatron measurements. The outermost curves (dotted) give the total error band from all parameterisations considered.

2.1 Total pp cross-section

A precise measurement of the total pp cross-section σ_{tot} and of the elastic scattering over a large range in the squared four-momentum transfer t (section 2.2) is of primary importance for distinguishing between different models of soft proton interactions.

Figure 2.2 summarises the existing measurements of σ_{tot} from low energies up to collider and cosmic-ray energies. Unfortunately the large uncertainties of the cosmic-ray data and the 2.6 standard-deviations discrepancy between the two final results from the Tevatron [3, 4] make an extrapolation to higher energies uncertain, leaving a wide range for the expected value of the total cross-section at the LHC energy of $\sqrt{s} = 14\,\mathrm{TeV}$, typically from 90 to 130 mb, depending on the model used for the extrapolation.

TOTEM will measure σ_{tot} and the luminosity $\mathscr{L}$ simultaneously by taking advantage of the Optical Theorem:

$$\mathscr{L}\,\sigma_{tot}^2 = \frac{16\pi}{1+\rho^2} \cdot \left.\frac{dN_{el}}{dt}\right|_{t=0}.$$
(2.1)

With the additional relation

$$\mathscr{L}\,\sigma_{tot} = N_{el} + N_{inel}$$
(2.2)

one obtains a system of 2 equations which can be solved for σ_{tot} or $\mathscr{L}$. The parameter

$$\rho = \frac{\mathscr{R}[f_{el}(0)]}{\mathscr{I}[f_{el}(0)]},$$
(2.3)

– 4 –

where $f_{el}(0)$ is the forward nuclear elastic amplitude, has to be taken from external theoretical predictions, e.g. [5]. Since $\rho \sim 0.14$ enters only in a $1 + \rho^2$ term, its impact is small (see estimate in section 6.3.3).

Hence the quantities to be measured are the following:

- The inelastic rate N_{inel} consisting of non-diffractive minimum bias events ($\sim$65 mb at LHC) and diffractive events ($\sim$18 mb at LHC) which will be measured by T1 and T2.

- The total nuclear elastic rate N_{el} measured by the Roman Pot system.

- $dN_{el}/dt|_{t=0}$: The nuclear part of the elastic cross-section extrapolated to $t = 0$ (see section 2.2). The expected uncertainty of the extrapolation depends on the acceptance for elastically scattered protons at small $|t|$-values and hence on the beam optics.

For the rate measurements it is important that all TOTEM detector systems have trigger capability.

At an early stage with non-optimal beams, TOTEM will measure the total cross-section and the luminosity with a precision of about 5%. After having understood the initial measurements and with improved beams at $\beta^* = 1540$ m (cf. chapter 3), a precision around 1% should be achievable.

Even later, a measurement of ρ via the interference between Coulomb and hadronic contributions to the elastic scattering cross-section might be attempted at a reduced centre-of-mass energy of about 8 TeV [6]. The main interest of ρ lies in its predictive power for σ_{tot} at higher energies via the dispersion relation

$$\rho(s) = \frac{\pi}{2\sigma_{tot}(s)} \frac{d\sigma_{tot}}{d\ln s}. \tag{2.4}$$

2.2 Elastic pp scattering

Much of the interest in large-impact-parameter collisions centres on elastic scattering and soft inelastic diffraction. High-energy elastic nucleon scattering represents one of the collision processes in which very precise data over a large energy range have been gathered. The differential cross-section of elastic pp interactions at 14 TeV, as predicted by different models [7], is given in figures 2.3 and 2.4.

The dashed graphs show the cross-section of pure nuclear scattering, i.e. neglecting the influence of the Coulomb component, which would be justified for $|t| > 10^{-3}$ GeV^2 assuming the validity of the West and Yennie description [8] of the Coulomb-nuclear interference. However, it has been shown that this formula requires $\rho(t)$ to be t independent which is not fulfilled experimentally and theoretically inconsistent [9]. Hence a second set of graphs (continuous lines) is shown taking into account the Coulomb component with a formulation of the total amplitude based on the eikonal approach. This model also describes the influence of Coulomb scattering at higher values of $|t|$, which is visible in figure 2.4 above 0.25 GeV^2.

Increasing $|t|$ means looking deeper into the proton at smaller distances. Several t-regions with different behaviour can be distinguished:

- $|t| < 6.5 \times 10^{-4}$ GeV^2 (at $\sqrt{s}$=14 TeV): The Coulomb region where elastic scattering is dominated by photon exchange: $d\sigma/dt \sim 1/t^2$.
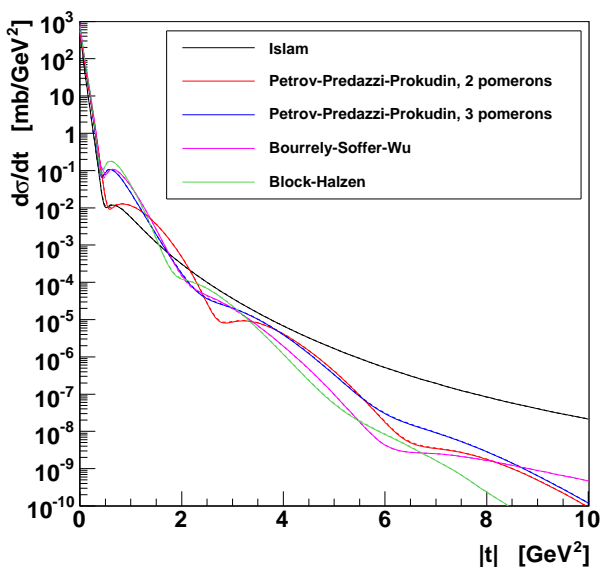
Figure 2.3: Differential cross-section of elastic scattering at $\sqrt{s} = 14\,\text{TeV}$ as predicted by various models [7]. On this scale, the cross-sections with and without the Coulomb component (continuous and dashed lines respectively) cannot be distinguished.
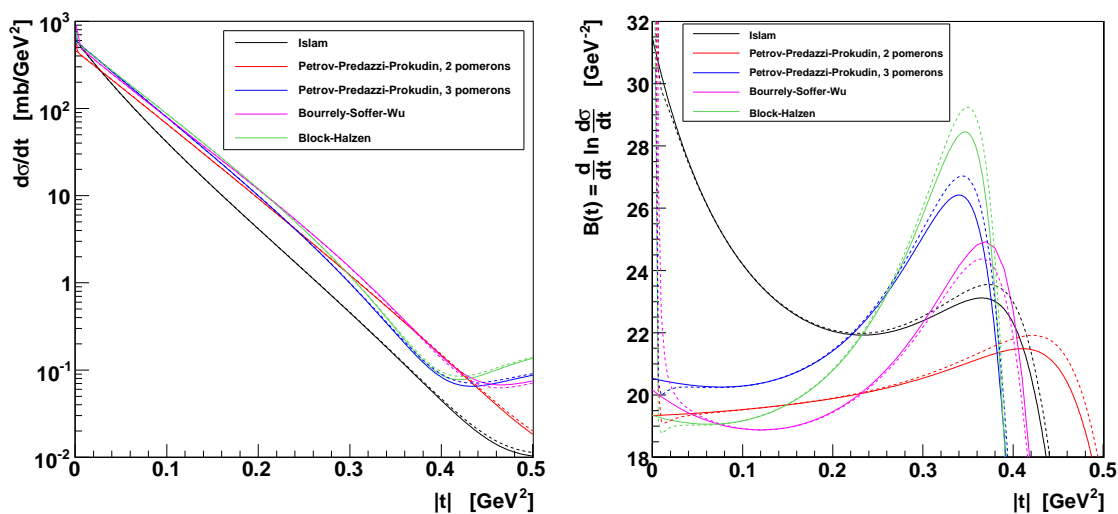
Figure 2.4: Left: differential cross-section of elastic scattering at 14 TeV as predicted by various models [7], focussing on the quasi-exponential domain at low $|t|$. Right: exponential slope of the differential cross-section. The deviations from a constant slope show how the cross-sections differ from a pure exponential shape. Continuous (dashed) lines: with (without) Coulomb interaction.

- $10^{-3}\,\text{GeV}^2 < |t| < 0.5\,\text{GeV}^2$: The nuclear region described in a simplified way by "single-Pomeron exchange"[1] with an approximately exponential cross-section $d\sigma/dt \sim \mathrm{e}^{-B|t|}$ (figure 2.4, left). This quasi-exponential domain is important for the extrapolation of the differential counting-rate dN_{el}/dt to $t = 0$, needed for the measurement of σ_{tot}. The t-dependence of the exponential slope $B(t) = \frac{d}{dt}\ln\frac{d\sigma}{dt}$ reveals slight model-dependent deviations from the exponential shape (figure 2.4, right). This theoretical uncertainty contributes to the systematic error of the total cross-section measurement (section 6.3.2).

- Between the above two regions, the nuclear and Coulomb scattering interfere, complicating the extrapolation of the nuclear cross-section to $t = 0$.

- $0.5\,\text{GeV}^2 < |t| < 1\,\text{GeV}^2$: A region exhibiting the diffractive structure of the proton.

- $|t| > 1\,\text{GeV}^2$: The domain of central elastic collisions at high $|t|$, described by perturbative QCD, e.g. in terms of triple-gluon exchange with a predicted cross-section proportional to $|t|^{-8}$. The model dependence of the predictions being very pronounced in this region, measurements will be able to test the validity of the different models.

With different beam optics and running conditions (chapter 3), TOTEM will cover the $|t|$-range from $2 \times 10^{-3}\,\text{GeV}^2$ to about $10\,\text{GeV}^2$.

2.3 Diffraction

Diffractive scattering comprises Single Diffraction, Double Diffraction, Central Diffraction (a.k.a. "Double Pomeron Exchange"), and higher order ("Multi Pomeron") processes. Together with the elastic scattering these processes represent about 50% of the total cross-section. Many details of these processes with close ties to proton structure and low-energy QCD are still poorly understood. The majority of diffractive events (figure 2.5) exhibits intact ("leading") protons in the final state, characterised by their t and by their fractional momentum loss $\xi \equiv \Delta p/p$. Depending on the beam optics (chapter 3) most of these protons can be detected in Roman Pot detectors far away from the interaction point. Already at an early stage, TOTEM will be able to measure ξ-, t- and mass-distributions in soft Double Pomeron and Single Diffractive events. The full structure of diffractive events with one or more sizeable rapidity gaps in the particle distributions (figure 2.5) will be optimally accessible when the detectors of CMS and TOTEM will be combined for common data taking with an unprecedented rapidity coverage, as discussed in [2].

---

[1]Nuclear elastic and diffractive scattering are characterised by the exchange of hadronic colour singlets, for which the Pomeron is one model.

Elastic Scattering

Φ

0

η

18 mb   ~30 mb

Single Diffraction
(SD)

Φ

0

η

9.4 mb   ~10 mb

Double Diffraction
(DD)

Φ

0

Δη

η

6.3 mb   ~7 mb
(for Δη > 3)

Double
Pomeron
Exchange
(DPE)

Φ

0

η

~1 mb

Single + Double
Diffraction
(SDD)

Φ

0

η

1.5 mb
(for Δη > 3)

Multi
Pomeron
Exchange

Φ

0

η
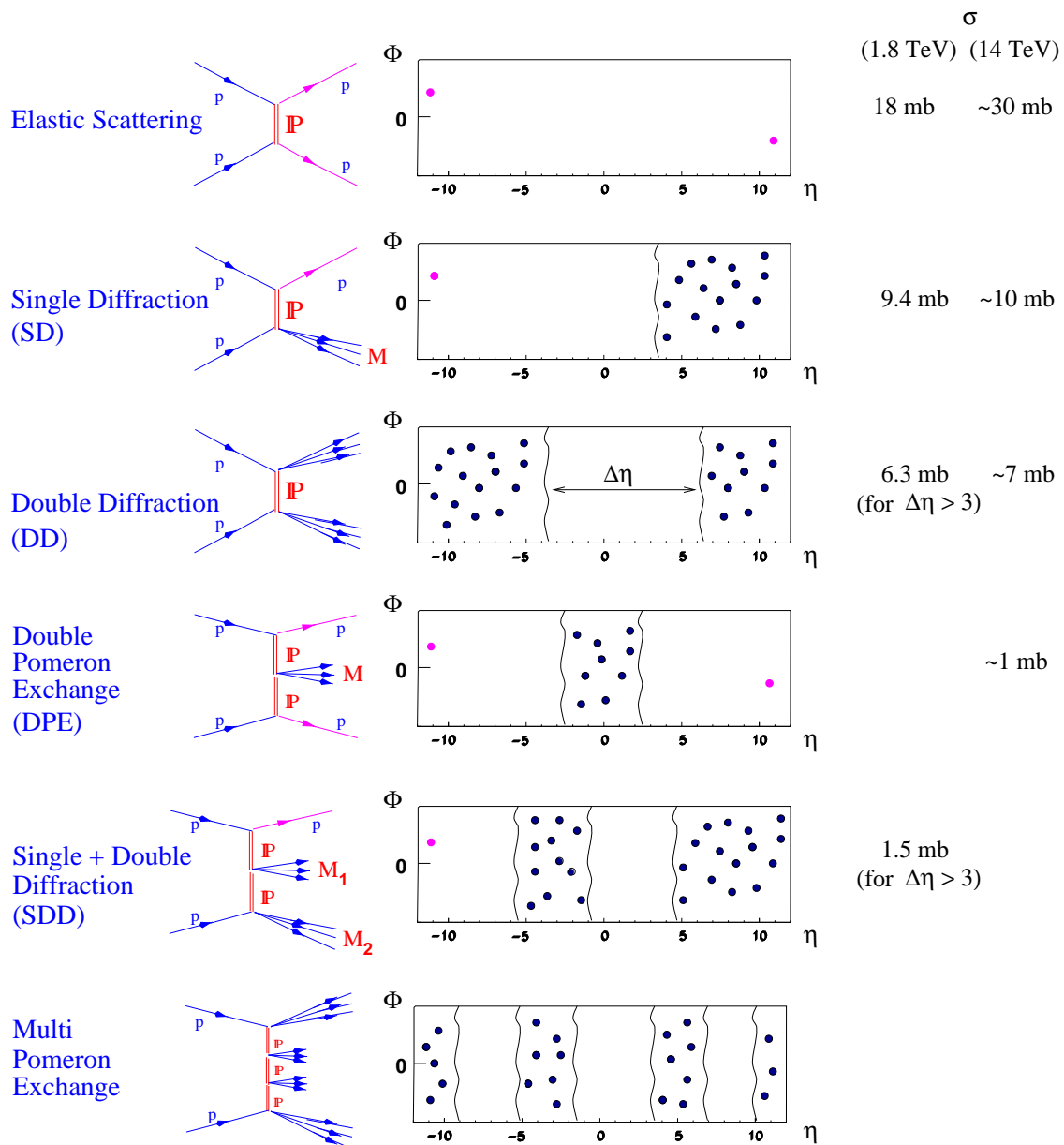
Figure 2.5: Diffractive process classes and their cross-sections measured at Tevatron and estimated for the LHC.

Chapter 3

Beam optics and running conditions

For the luminosity independent total cross-section measurement TOTEM has to reach the lowest possible values of the squared four momentum transfer $-t \sim p^2\Theta^2$ in elastic pp scattering.

Scattered particles close to the beam can be detected downstream on either side of the Interaction Point (IP) if the displacement at the detector location is large enough (at least $10\sigma_{\text{beam}}$ away from the beam center) and if the beam divergence ($\sim 1/\sqrt{\beta^*}$) at the IP is small compared to the scattering angle. In order to achieve these conditions special high beta optics are required: the larger the β^*, the smaller the beam divergence will be.

Two optics have been proposed: the ultimate one with $\beta^* = 1540\,\text{m}$, probably foreseen at a later stage, and another one with $\beta^* = 90\,\text{m}$. The latter uses the standard injection optics and the beam conditions typical for early LHC running: zero degree crossing-angle and consequently at most 156 bunches together with a low number of protons per bunch.

3.1 Properties of the high-β^* Optics

The properties of the optics can be expressed by the two optical functions L (effective length) and v (magnification) which, at a distance s from the IP, are defined by the betatron function $\beta(s)$ and the phase advance $\Delta\mu(s)$:

$$
\begin{aligned}
v(s) &= \sqrt{\frac{\beta(s)}{\beta^*}}\cos\Delta\mu(s) \\
L(s) &= \sqrt{\beta(s)\beta^*}\sin\Delta\mu(s) \\
\text{with } \Delta\mu(s) &= \int_0^s \frac{1}{\beta(s')}ds'
\end{aligned}
\tag{3.1}
$$

The transverse displacement $(x(s), y(s))$ of a proton at a distance s from the IP is related to its transverse origin (x^*, y^*) and its momentum vector (expressed by the horizontal and vertical scattering angles Θ_x^* and Θ_y^* and by $\xi = \Delta p/p$) at the IP via the above optical functions and the dispersion $D(s)$ of the machine:

$$
\begin{aligned}
y(s) &= v_y(s) \cdot y^* + L_y(s) \cdot \Theta_y^* \\
x(s) &= v_x(s) \cdot x^* + L_x(s) \cdot \Theta_x^* + \xi \cdot D(s)
\end{aligned}
\tag{3.2}
$$
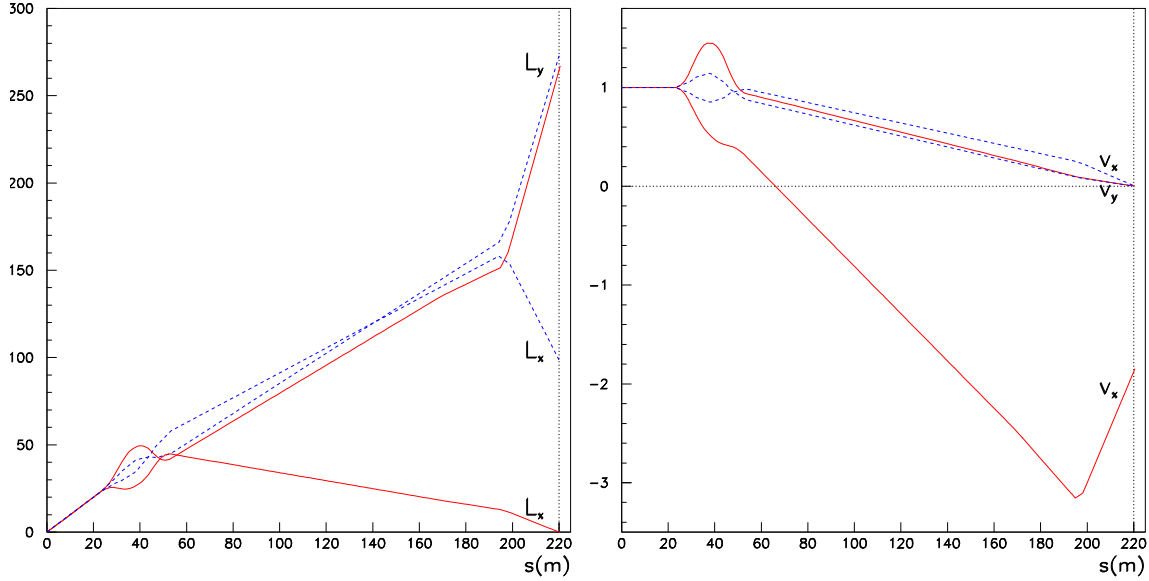
Figure 3.1: The optical functions for β^*=90 m (solid) and 1540 m (dashed) as function of the distance s to IP5: effective length L [in m] (left) and magnification v (right).

As a consequence of the high β^*, the beam size at the IP is large ($\sigma^*_{\text{beam}} \propto \sqrt{\beta^*}$). To eliminate the dependence on the transverse position of the proton at the collision point, the magnification has to be chosen close to zero (parallel-to-point focussing, $\Delta\mu = \pi/2$). At the same time, a large effective length ensures a sizeable displacement from the beam centre.

Having in mind the above optimisation for the position of the RP station RP220, two scenarios have been studied. Their optical functions are compared in figure 3.1. For $\beta^* = 1540$ m, the parallel-to-point focussing is achieved in both projections whereas for $\beta^* = 90$ m only in the vertical one. In both cases, the large L_y pushes the protons vertically into the acceptance of the RP detectors.

The minimum distance of a detector from the beam is proportional to the beam size:

$$y_{\min} = K\sigma_y^{\text{beam}} = K\sqrt{\varepsilon\beta_y(s)}\,, \tag{3.3}$$

where ε is the transverse beam emittance and K is around 10–15. Assuming perfect parallel-to-point focussing, the smallest detectable angle is:

$$\Theta^*_{y\ min} = K\sqrt{\frac{\varepsilon}{\beta^*_y}}\,. \tag{3.4}$$

The parallel-to-point focussing condition allows the measurement of both t components (t_x, t_y) for elastically scattered protons at $\beta^* = 1540$ m but only the vertical component at $\beta^* = 90$ m.

Both optics also offer the possibility of detecting diffractive protons almost independent of their momentum loss. To be able to measure the momentum loss ξ with an acceptable resolution, L_x has to vanish to eliminate the dependence on the horizontal scattering angle Θ^*_x (cf. eq. (3.2)). This condition can only be achieved with the $\beta^* = 90$ m optics (figure 3.1).
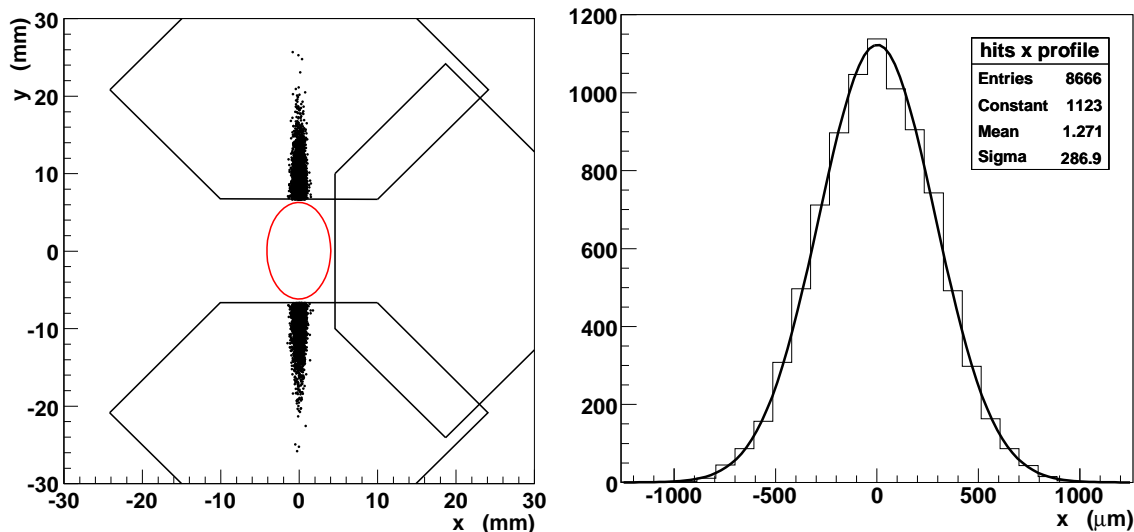
Figure 3.2: Left: hit distribution for elastic-scattering events in the detectors of RP220 with the $\beta^* = 90$ m optics; the $10\,\sigma_{\text{beam}}$ beam envelope is also shown. Right: hit distribution in the horizontal projection (x) at RP220.

3.2 Beam diagnostics

In addition to the luminosity measurement via the Optical Theorem, TOTEM can contribute more information to beam diagnostics, in particular with the $\beta^* = 90$ m optics. There, the horizontal hit positions of elastically scattered protons in the RP 220 m station depend only on the vertex position and not on the horizontal scattering angle. Thus the narrow hit distribution (figure 3.2) reflects well the horizontal beam position at the Roman Pot which can be used for an absolute calibration of the Beam Position Monitors on the micrometre level. Furthermore, this hit distribution gives access to the horizontal vertex distribution which can furthermore – assuming round beams — be exploited for an independent luminosity measurement based on beam parameters.

3.3 Running scenarios

The versatile physics programme of TOTEM requires different running scenarios that have to be adapted to the LHC commissioning and operation in the first years. A flexible trigger can be provided by the Roman Pot detectors and the T1 and T2 telescopes as discussed in chapter 8. TOTEM will take data under all optics conditions, adjusting the trigger schemes to the luminosity. The DAQ will allow trigger rates up to a few kHz without involving a higher level trigger.

The high-β^* runs (table 3.1) with 156 bunches, zero degree crossing-angle and maximum luminosity between 10^{29} and $10^{30}\,\text{cm}^{-2}\text{s}^{-1}$, will concentrate on low-$|t|$ elastic scattering, total cross-section, minimum bias physics and soft diffraction. A large fraction of forward protons will be detected even at the lowest ξ values.

Low-β^* runs (table 3.2) with more bunches and higher luminosity ($10^{32} – 10^{33}\,\text{cm}^{-2}\text{s}^{-1}$) will be used for large-$|t|$ elastic scattering and diffractive studies for $\xi > 0.02$. Hard diffractive events come within reach.

Table 3.1: Running Scenarios for high β^* (k: number of bunches, N: number of protons per bunch). The t ranges given correspond to the $\geq 50\%$ acceptance intervals.

β^* [m]	k	$N/10^{11}$	$\mathscr{L}$ [cm^{-2}s^{-1}]	$|t|$-range [GeV^2] @ $\xi = 0$	ξ-range
1540	$43 \div 156$	$0.6 \div 1.15$	$10^{28} \div 2 \times 10^{29}$	$0.002 \div 1.5$	< 0.2
90	156	$0.1 \div 1.15$	$2 \times 10^{28} \div 3 \times 10^{30}$	$0.03 \div 10$	< 0.2

Table 3.2: Running Scenarios for low β^* (k: number of bunches, N: number of protons per bunch)

β^* [m]	k	$N/10^{11}$	$\mathscr{L}$ [cm^{-2}s^{-1}]	$|t|$-range [GeV^2] @ $\xi = 0$	ξ-range
11	$936 \div 2808$	1.15	3×10^{32}	$0.6 \div 8$	$0.02 \div 0.2$
$0.5 \div 2$	$936 \div 2808$	1.15	10^{33}	$1 \div 10$	$0.02 \div 0.2$

Chapter 4

The Roman Pot system

4.1   System strategy and overview

The detection of very forward protons in movable beam insertions — called Roman Pots (RP) — is an experimental technique introduced at the ISR [10]. It has been successfully employed in other colliders like the S$\bar{\mathrm{p}}$pS, TEVATRON, RHIC and HERA. Detectors are placed inside a secondary vacuum vessel, called a pot, and moved into the primary vacuum of the machine through vacuum bellows. In this way, the detectors are physically separated from the primary vacuum which is thus preserved against an uncontrolled out-gassing of the detector's materials.

The challenging constraints of the LHC, such as the thin high-intensity beam, the Ultra High Vacuum and the high radiation fluxes have required the development of new Roman Pots. The main differences to RPs designed for earlier machines lie in the window technology of the pots, which have to be placed much closer to the beam, and in the driving mechanism, which must have high precision and radiation hardness.

Being symmetric with respect to IP5, TOTEM's RP system allows the reconstruction of protons on both sides of the interaction point. On each side, two stations of Roman Pots will be mounted on the beam pipe of the outgoing beam. Their positions have been defined in an interplay with the development of the special optics used by TOTEM, with constraints given by the space available between the LHC machine components. The centre of the first station ('RP147') is placed at 149.6 m from IP5, and the second ('RP220') at 217.3 m. Between the two stations, the dipole magnet D2 provides a dispersion difference which helps in proton momentum reconstruction. To have a lever arm for local track reconstruction and trigger selections by track angle, each RP station is composed of two units separated by a distance limited by integration constraints with the other beam elements (figure 4.1). The stations RP147 and RP220 span distances of 1.2 m and 5 m respectively. Each RP unit consists of 3 pots, 2 approaching the beam vertically and 1 horizontally. A schematic drawing of the beam-pipe of a RP unit with its insertions is shown in figure 4.2 (left). In summary, a total of 8 identical Roman Pot units or 24 individual pots are installed in the LHC.

The single horizontal pot in each unit, placed on the radially outer side of the LHC ring, serves two purposes. Firstly, it completes the acceptance for diffractively scattered protons whose momentum loss deviates them towards this pot. On the radially inner side of the LHC ring no detector is needed since only background protons arrive in that position. Secondly, the detectors in
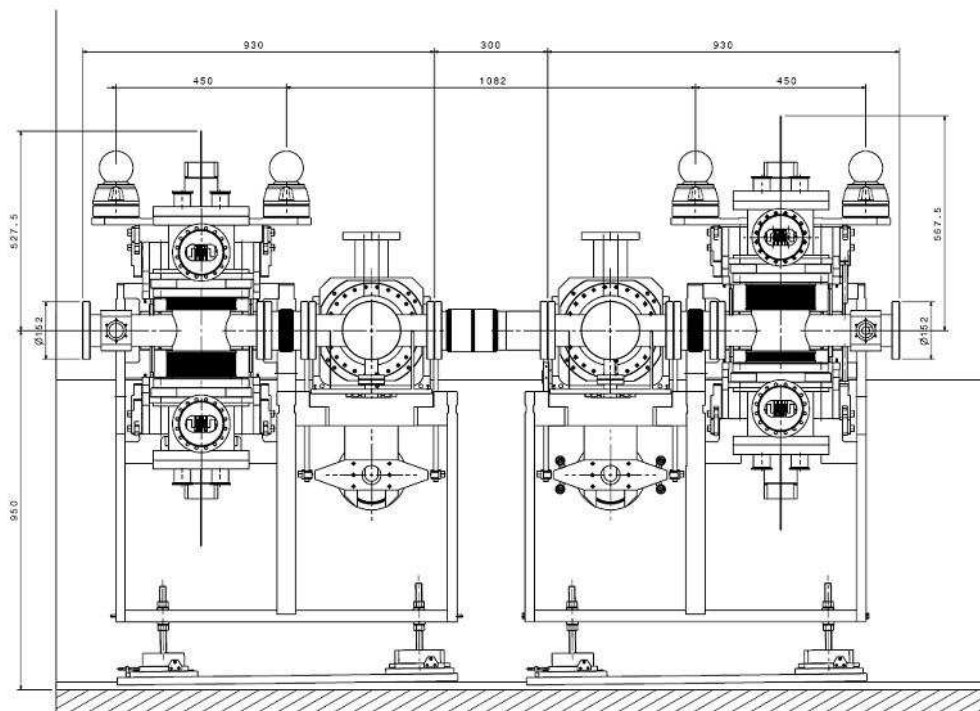
Figure 4.1: Design drawing of the station RP147, i.e. an assembly of two RP units. The other station, RP220, is identical apart from the bigger distance between the two units.
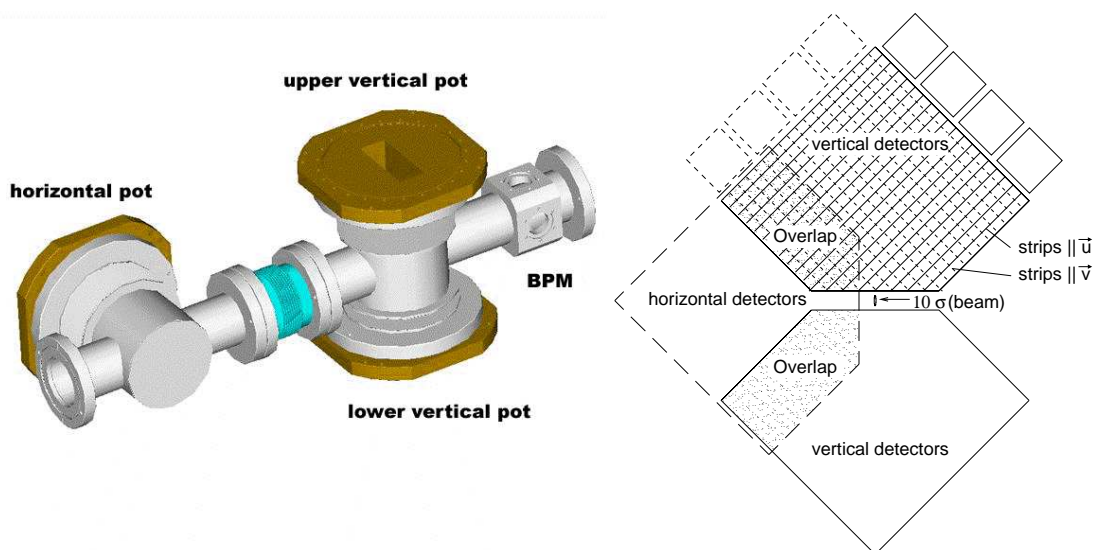
Figure 4.2: Left: the vacuum chambers of a RP unit accomodating the horizontal and the vertical pots and the Beam Position Monitor. Right: the overlap between the horizontal and vertical detectors.
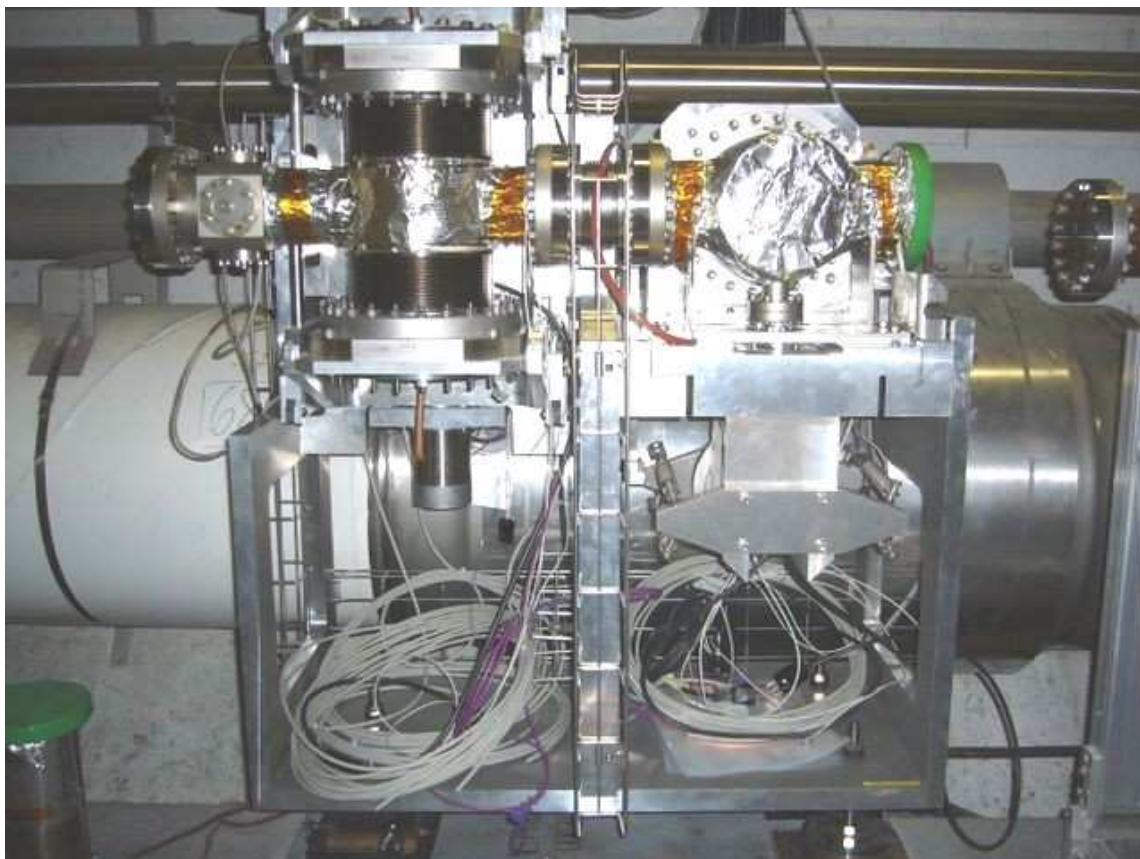
Figure 4.3: A unit of the first RP220 station installed in the LHC.

the horizontal pots overlap with the ones in the vertical pots, which correlates their positions via common particle tracks (see figure 4.2, right). This feature is used for the relative alignment of the three pots in a unit. For the absolute alignment, i.e. with respect to the beam, a Beam Position Monitor (BPM), based on a button feed-through technology, is integrated in the vacuum chamber of the vertical RP. A pre-calibration of the BPM relative to the pots is done in a metrology laboratory.

Each pot is equipped with a stack of 10 planes of novel "edgeless" silicon strip detectors (section 4.3). Half of them will have their strips oriented at an angle of $+45°$ with respect to the edge facing the beam, and the other half at an angle of $-45°$, measuring the coordinates u and v respectively. This configuration has the advantage that the hit profiles in the two projections are equivalent. The measurement of each track projection in five planes is advantageous for the reduction of uncorrelated background via programmable coincidences, requiring e.g. collinear hits in a majority of the planes.

Figure 4.3 shows a unit of an RP220 station after installation in the LHC.
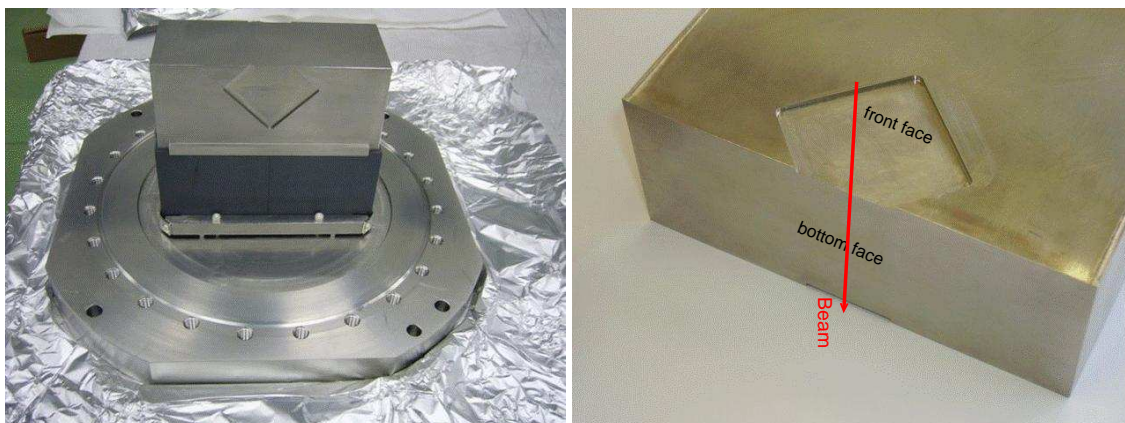
Figure 4.4: Left: the pot with the thin window and the Ferrite collar (black) needed to reduce the beam coupling impedance. Right: detailed view of the thin window; the front face is 0.5 mm thick, while the bottom face (towards the beam) is 0.15 mm thick.

4.2 Mechanical design of the Roman Pot

4.2.1 The vacuum chamber

Like all the 'warm' (i.e. non-cryogenic) vacuum equipment of the LHC, the RP vacuum chambers had to be baked out at 150°C. The supports of the two Roman pot vacuum chambers have been designed to allow a free dilatation during the bake out. Such a feature relieves the stress on the components and prevents permanent deformation. In addition, an interconnection bellow between the two vacuum chambers decouples the thermal deformations.

4.2.2 The pot and its thin window

The pot (figure 4.4) provides a volume with a secondary vacuum where the detectors and the services are enclosed. It has the shape of a 50 mm × 124 mm × 105 mm rectangular box, with 2 mm wall thickness, made of stainless steel (316LN). A support flange is attached to the box by electron beam welding. One side of the flange is connected to a bellow to close the machine vacuum volume (figure 4.5). The opposite side is connected to a second flange equipped with the detectors, which closes the secondary vacuum volume.

The RP window is composed of three parts: one facing the beam ("bottom face") and two orthogonal to the beam ("front and rear faces"). All faces have to be as thin as possible:

- The bottom face is a part of the insensitive space between the point of closest physical RP-to-beam approach and the efficient detector region. This insensitive space has to be kept small.

- The front and rear faces are traversed perpendicularly by the protons to be measured and by beam halo. To minimise signal proton deflections and showers, the window has to be kept thin.
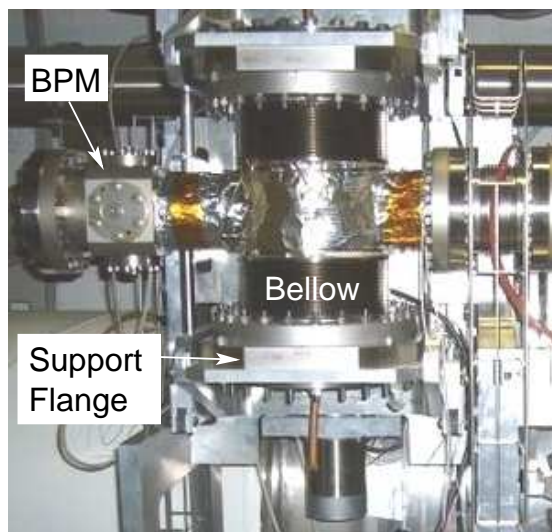
Figure 4.5: Detail of the RP220 station: the vertical pots attached to the vacuum tube by bellows.

Hence the window material, design and manufacturing technique have been optimised in view of achieving a minimum thickness and a flatness better than $50\,\mu$m, while maintaining UHV leak tightness and minimising deformations under pressure differences up to a safety-imposed limit of 1.5 bar. Comparative studies have shown that for the bottom face a thickness of 0.15 mm in stainless steel represents an optimum, while for the front and rear faces a thickness of 0.5 mm was chosen.

Several assembly procedures, like brazing, TIG and EB welding, have been investigated at CERN by the Assembly Technique group. The most satisfactory results have been obtained by brazing. The first step consists in brazing a thin window of stainless steel 316L on the bottom part of the pot. Successively the milling of the lateral sides is done, obtaining a 0.5 mm window. An excellent planarity down to $30\,\mu$m has been obtained on the prototypes.

Pressure cycles in the range ± 1 bar were applied, followed by vacuum leak tests. The maximum deformation was 0.4 mm at 1 bar, while no leaks were detected with a threshold of 2×10^{-12} mbar l/s. An ultimate hydraulic pressure test was done on two prototypes. One was loaded with a fast pressure rise, and it broke at 50 bar. The second was loaded more slowly, and the test was stopped at 80 bars without rupture (figure 4.6). For both cases, the pressure levels are many times higher than the 1.5 bar required for safety.

The pot together with the bellow creates a resonant RF cavity for the beam running along the axis of the Roman Pot. Measurements of the beam coupling impedance have been performed in the lab where a metallic wire was strung through the RP [11]. A vector network analyser generated current pulses to simulate the beam and measured the complex transmission coefficient. The bare RP (without any ferrites mounted) shows several resonances in its longitudinal beam-coupling impedance Z_L. The dominant line at 740 MHz has an impedance of 1.2 kΩ corresponding to a broad-band value $Z/n = 18$ mΩ with $n = f_{\text{resonance}}/f_{\text{LHC}}$ = 740 MHz / 11 kHz. This value was still well below but uncomfortably close to the LHC limit of $Z/n = 0.1\,\Omega$. However, a 2 mm thin collar of ferrites fixed on the external wall of the pot insertion (figure 4.4, left) removes all the resonances within the frequency domain relevant for the LHC, i.e. $0-1.5$ GHz.

Figure 4.6: Deformation of the thin window after the ultimate pressure test, stopped at 80 bar.

4.2.3 The movements

Each pot is independently moved by micro-stepping motors with angular steps of $(0.90 \pm 0.03)°$ per step, corresponding to 400 steps per turn. The transformation from the motor's rotational movement to the pot's translation movement is done by roller screws which provide high precision and zero backlashes.

A mechanical compensation system (figure 4.7) balances the atmospheric pressure load on the pot. The system relieves the stress on the driving mechanism, improving the movement accuracy and the safety of the operations. It is based on a separate vacuum system connected to the primary vacuum of the machine through a by-pass. The atmospheric pressure load on the pot-bellow system is $\sim$3000 N. With such a compensation system the stepper motor works only against the weight of the pot assembly ($\sim$100 N), leaving the possibility to achieve a better accuracy of the motor drive mechanism. With bellows on the compensation system larger than the pot bellows, a constant pulling load on the pots is guaranteed, and since the roller screws are a reversible mechanism, this feature is exploited to provide auto-retraction of the pots in case of a motor power cut.

The nominal mechanical pot-positioning resolution of the driving mechanism is 5 μm, but the final precision depends on the assembly of the motors and the roller screws. The stepper motors are equipped with angular resolvers which give the absolute position of each pot with respect to the nominal beam axis. Additional displacement inductive sensors (LVDT) provide the absolute position of each pot.

The driver units and the power supplies are placed in the counting room at up to 300 m cable distance, in a radiation protected area, where access is always possible, even with circulating beams.

4.3 "Edgeless" silicon detectors with current terminating structure

Due to their high energy, the LHC beams are very thin ($10\sigma \approx 0.8$ mm at RP220 for $\beta^* = 1540$ m). It is therefore mandatory that the silicon detectors, housed in the RPs, approach the beam centre
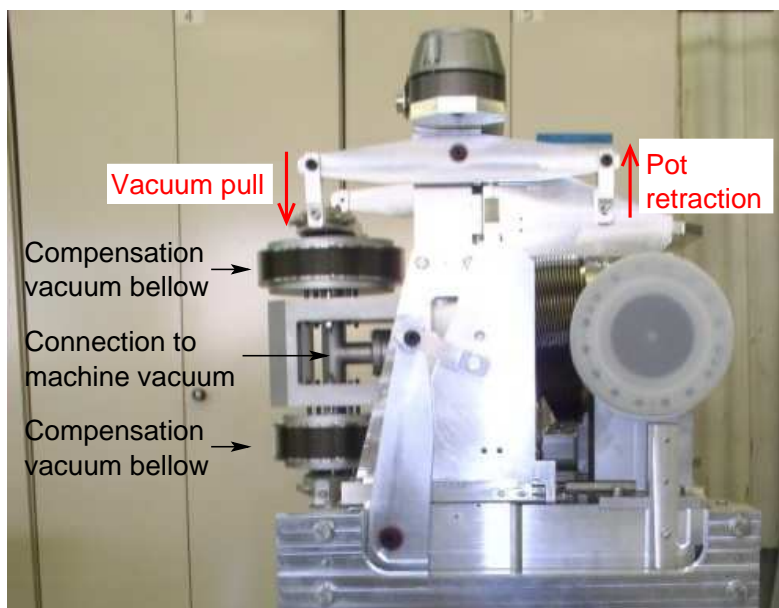
Figure 4.7: The vacuum compensation system.

to a distance as small as 1 mm. Consequently the detectors have to be fully efficient up to their mechanical edge.

Silicon detectors fabricated with standard planar technology require terminating structures to reduce electric field maxima at the detector periphery to prevent the surface irregularities on the chip cut from affecting the device performance, and to reduce the breakdown probability. They are generally a sequence of floating guardrings surrounding the sensitive part of the device and adding an external dead volume. This ring structure, called "voltage terminating structure", controls the potential distribution between the detector's sensitive area and the cut edge to have a vanishing potential drop at the chip cut. The insensitive margin increases with the number of rings, and for high voltage applications, as is the case for silicon detectors used in harsh radiation environments, it can be more than 1 mm wide. For the TOTEM experiment the reduction of this dead space is vital.

These requirements first led to tests with silicon detectors operated at cryogenic temperatures ($\sim 110\,\mathrm{K}$, [12]) and finally triggered the development of a new terminating structure that allows detectors fabricated with standard planar technology to reach full sensitivity within less than $100\,\mu\mathrm{m}$ from the cut edge and to operate with high bias at room temperature [13].

4.3.1 The concept of current terminating structures

For segmented devices with this new so-called "Current Terminating Structure (CTS)", the potential applied to bias the device has to be applied also across the cut edges via a guardring running along the die cut and surrounding the whole sample. This external guardring, also called "Current Terminating Ring (CTR)" collects the current generated in the highly damaged region at the cut edge, avoiding its diffusion into the sensitive volume, and is separated from the biasing electrode (BE). In this manner the sensitive volume can start at less than $50\,\mu\mathrm{m}$ from the cut edge. To prevent
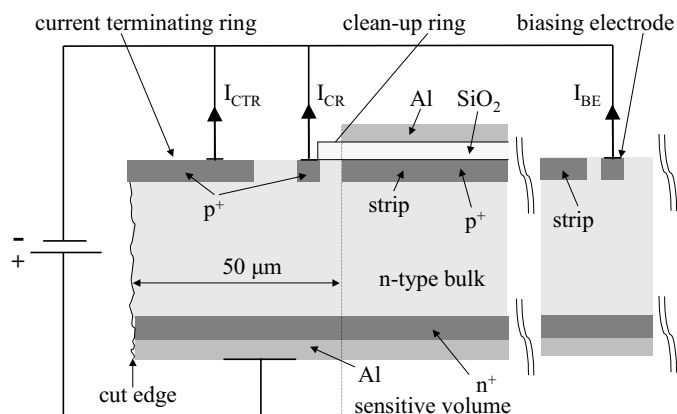
Figure 4.8: Cross-section of a silicon detector with CTS in the plane parallel to the strips and its biasing scheme.
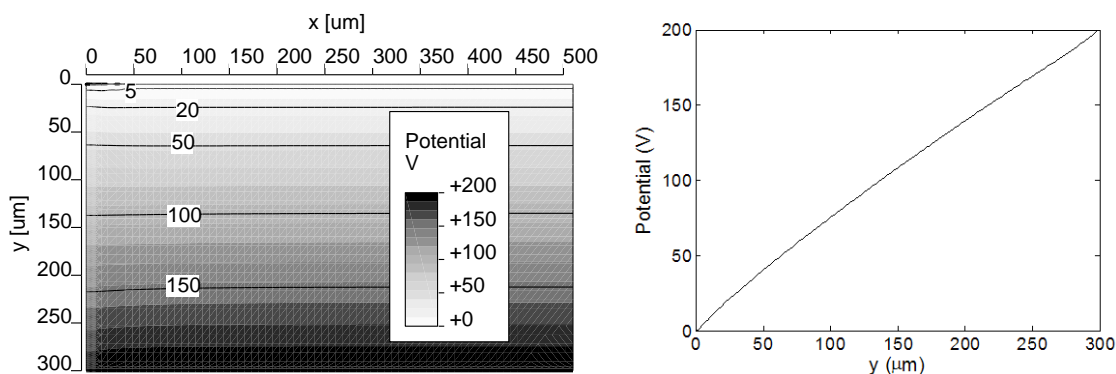
Figure 4.9: Left: potential distribution at the edge of a 300 μm thick silicon pad detector with CTS for a bias voltage of 200 V. The calculation extended up to 500 μm into the detector from the cut edge. Right: electric potential at the cut edge with an almost linear behaviour.

any further diffusion of this edge current into the sensitive volume, another implanted ring — the Clean-up Ring (CR) — can be placed between the CTR and the sensitive volume. The CTS and its biasing scheme are shown in figure 4.8.

For devices with this type of CTS, the leakage current in the sensitive volume (I_{BE}) which contributes to noise is not affected by the edge current ($I_{CTR} + I_{CR}$). The leakage current and the edge current have been shown to be completely decoupled. Moreover, for such devices, the charge collection efficiency has been shown to rise steeply from the edge of the sensitive volume reaching full efficiency within a few tens of micrometers (see section 4.6.1.1).

The electric potential distribution at the edge of a device with CTS has been modelled taking into account the highly damaged surface at the chip cut, where the irregularities within the first atomic layers could be assimilated to amorphous silicon. The results of this modelling have shown good consistency with the experimental results [14]. The potential distribution calculated with ISE TCAD [15] is shown in figure 4.9.
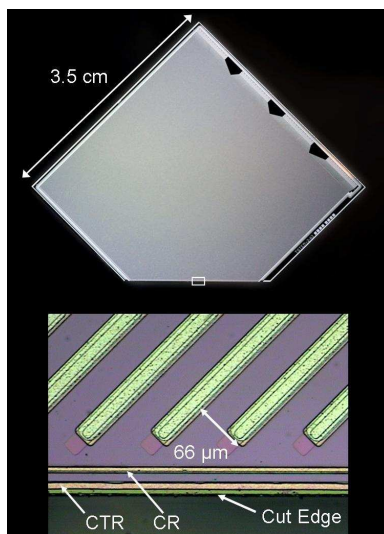
Figure 4.10: Picture of a Planar Edgeless Detector with CTS (top). The magnification of a portion of the chip cut region (bottom) shows the details of the CTS.

4.3.2 The silicon detector for the TOTEM Roman Pots

The advantages offered by the CTS have led TOTEM to choose this technology for the RP detectors. Geometry and granularity have been adapted to the specific requirements on surface coverage and spatial resolution.

The detectors have been developed and produced in a joint effort of the TOTEM group at CERN and Megaimpulse, a spin-off company from the Ioffe Physico-Technical Institute in St. Petersburg (Russia). These devices are single-sided AC p^+-n microstrip detectors with 512 strips and a pitch of 66 μm processed on very high resistivity n-type silicon wafers ($> 10 \text{k}\Omega \text{cm}$), 300 μm thick. All of them have the CTS as described in section 4.3 on one edge, i.e. the edge facing the beam. At one end of the strips an integrated pitch adapter reduces the inter-strip distance from 66 μm to 44 μm, producing four separated groups of 128 channels. This allows direct wire bonding to the readout chip VFAT. A picture of the planar edgeless Silicon detector for the TOTEM Roman Pots and a detail of the CTS are shown in figure 4.10. In these sensors the biasing is made via "punch-through" from a biasing electrode placed inside the CR. On all the sides where the sensitivity at the edge is not required, the CTS is integrated into a standard voltage terminating structure. The strips on the detector are at an angle of $45°$ with respect to the edge facing the beam.

4.3.3 Electrical characterisation

For the detector polarised according to the biasing scheme shown above, the typical values of currents measured at the CTR and the CR, $I_{CTR} + I_{CR}$, are compared to the current measured at the biasing electrode, I_{BE}, and shown in figures 4.11 and 4.12. There is a difference of four orders of magnitude between the current at the biasing electrode flowing through the sensitive volume of the detector and the one flowing through CR and CTR. This evidences that virtually all the leakage
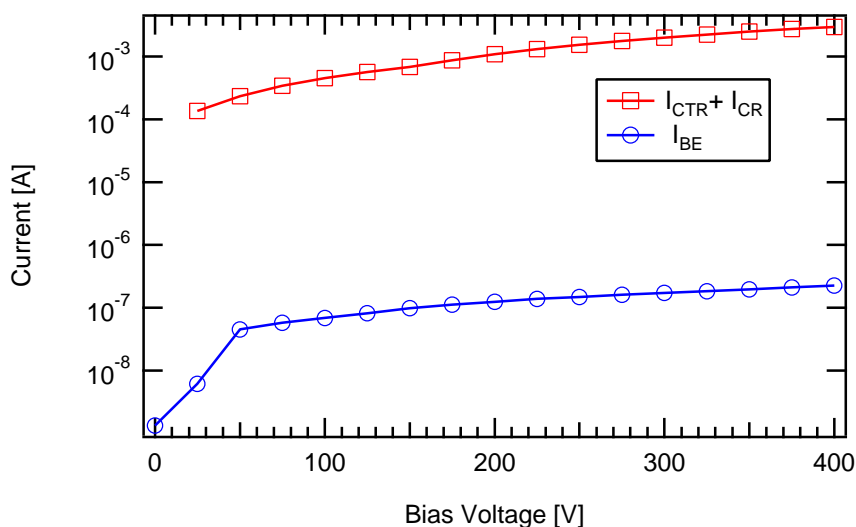
Figure 4.11: Current vs. voltage characteristics through the biasing electrode (I_{BE}) and across a detector edge ($I_{CTR} + I_{CR}$), measured at room temperature.
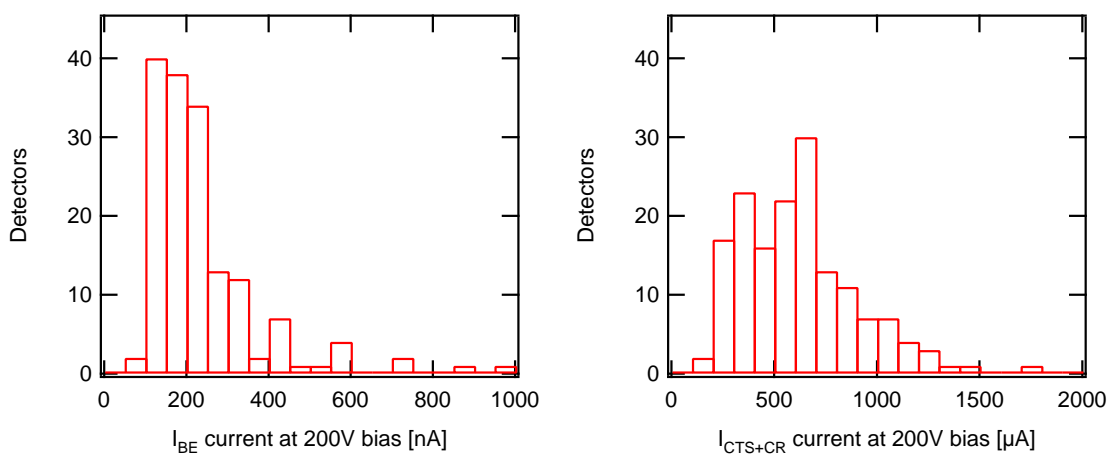
Figure 4.12: Distributions of the bulk current I_{BE} (left) and the edge current $I_{CTR} + I_{CR}$ (right) for a sample of 158 detectors at a bias voltage of 200 V.

current generated at the edge surface is collected by the CTR and the CR and does not flow through the sensitive volume where it would make detector operation impossible. The low current flowing into the biasing electrode confirms the validity of the current termination approach.
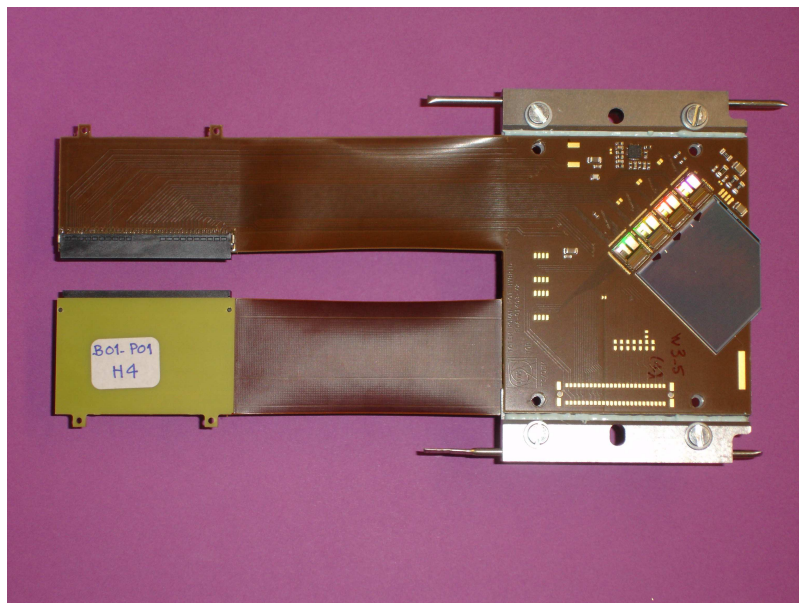
Figure 4.13: Two RP hybrids mounted back-to-back. Each hybrid carries the silicon detector and four VFAT readout chips.

4.4 On-detector electronics

The generalised electronics are described in more detail in chapter 7. Only the electronic boards that are relevant to the mechanical construction and the detector monitoring are discussed here. The silicon detector hybrid (figure 4.13) carries the detector with 512 strips wire-bonded to the input channels of 4 readout chips "VFAT" (section 7.1), and a Detector Control Unit (DCU) chip. Each VFAT provides tracking and trigger generation signals from 128 strips. The DCU chip is used to monitor detector leakage currents, power supply voltages and temperature. Via an 80 pin connector each VFAT will send the trigger outputs and the serialised tracking data from all strips to the motherboard, together with clock and trigger input signals, HV and LV power, and connections for a heater and a PT100 resistance thermometer for temperature control.

Due to the $\pm 45°$ orientation of the detector strips, flipping the detector hybrid and mounting it face to face with the next one results in mutually orthogonal strips giving the u and v coordinate information. To avoid losing space in between two hybrids, all electrical components are mounted on one side such that they do not overlap for the two cards mounted face to face and that they can be separated by only one component height.

In such way 10 detector hybrids closely arranged in 5 pairs, can be connected to one motherboard feeding all electrical connections through the flange between the pot's secondary vacuum and the outside world at atmospheric pressure.

The motherboard (figure 4.14) hosts clock and trigger distribution circuitry, Gigabit Optical Hybrids (GOH) — three for data and two for trigger bit transfer, two Coincidence Chip mezzanines, LVDS-to-CMOS converters, Trigger VFAT mezzanine, Control Unit mezzanine CCUM, Radiation Monitor circuitry and temperature sensors. The binary tracking data are stored in a digital memory
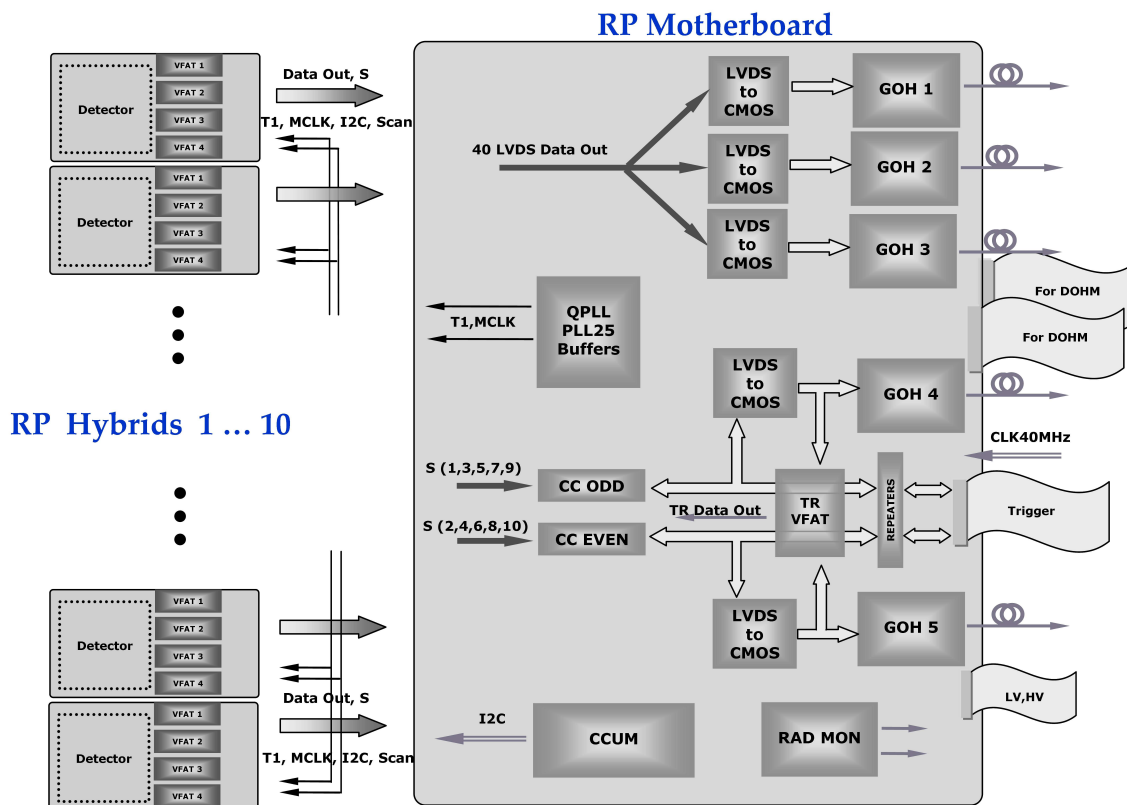
RP Motherboard

Figure 4.14: Block diagram of the RP motherboard with the connections to the hybrids.

and read out upon application of a readout trigger. A front panel with connectors for low and high voltage, control, data and trigger bit transfer to facilitates the connection to the central patch panel of the RP station.

To transmit the trigger bits to the counting room two options are implemented: the preferred choice — optical fibers — is used for the 150 m RP station and in TOTEM standalone runs also for the 220 m station. Common runs with CMS on the other hand are subject to CMS's limited trigger latency time, imposing trigger bit transmission with LVDS signals through fast electrical cables. The electrical transmission over such a long distance requires care to preserve signal integrity. This can only be achieved by restoring the LVDS signals to full levels at regular intervals over the transmission distance. A special integrated circuit was designed for this purpose: the LVDS repeater chip can treat 16 LVDS channels in parallel and was designed in special layout to guarantee radiation tolerance. This chip will be mounted on a small repeater board. At regular intervals of about 70 m a repeater station is introduced which consists of several repeater boards with cable connectors. Power for the repeaters is supplied along the cable as well, and filtered on board.
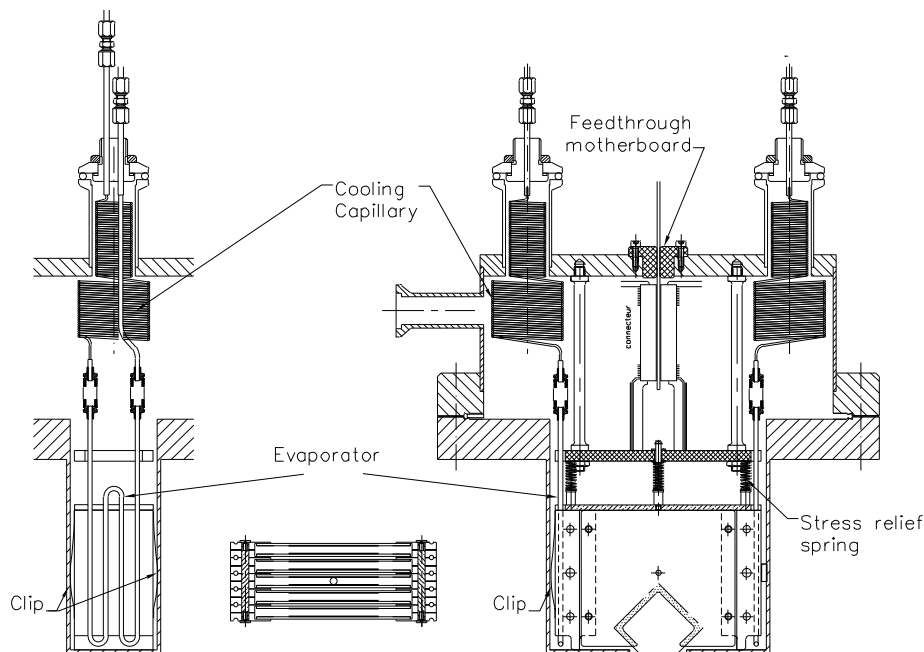
Figure 4.15: Conceptual design of the silicon detector package in the pot. In both views the clips for the alignment of the assembly are shown. The capillaries and evaporators are parts of the cooling system.

4.5 Detector integration and cooling in the Roman Pot

4.5.1 Integration of detector stacks in the pot

Each pot houses a compact stack of 10 detector planes with their hybrid boards and cooling pipes (figures 4.15, 4.16).

To keep the total width of the inefficient zone between the outer RP window surface and the active detector area below 0.5 mm, the distance between the thin window and the physical detector edge must not exceed 200 μm. The targeted alignment precision of 30 μm has to hold both at the mounting time and at the operation time. Since the detector modules will be mounted and operated at different temperatures, thermal contractions and expansions have to be taken into account.

The hybrid board is made of a processed Kapton film laminated on a high thermal conductivity substrate with a thickness of 0.5 mm. The material of the substrate is an Al-Si 70%–30% alloy (CE07), which has the advantage of a high thermal conductivity and a thermal expansion closely matching the one of the silicon sensor. The connectivity between the hybrid and the vacuum feed-through card (motherboard) is based on a kapton 'pigtail' with end connector. Both the silicon sensor and the four VFAT chips are glued with thermally conductive thermoplastic film to the hybrid. The chips are aligned on the hybrid using precision markers. After bonding the outputs of the chips to the hybrid the proper functioning of the complete hybrid is tested. In a second step, the sensor is aligned such that the bond pads of chips and sensor are best matched, and the input side of the chips is then bonded to the sensor. No special tools, except a bonding jig are required up to this point. Ten completed hybrids are then assembled by means of precision dowels and micrometre
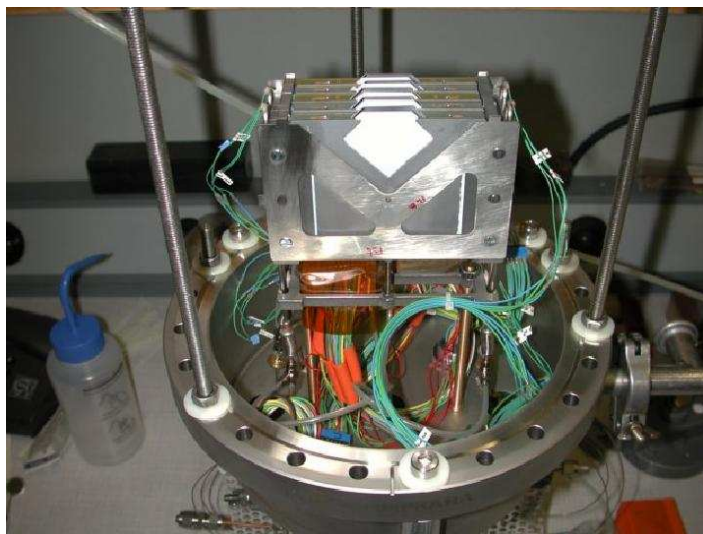
Figure 4.16: The detector package prototype mounted on the vacuum chamber.

stages to form the detector package. Survey with a 3D Coordinate Measuring Machine (CMM) is performed to determine the edge locations of all ten silicon sensors.

The assembly is fixed by means of a slightly flexible fixation on the support plate which is rigidly attached to the detector vacuum flange. The fixation is spring loaded. Once the detector is inserted in the Roman Pot, it exerts a small force on the bottom plate of the Pot ensuring the positioning of the assembly relative to the bottom plate. A flexible clip on the side of the assembly maintains the assembly with a slight force aligned to one side wall of the pot. A second similar clip will ensure the alignment of the assembly with respect to the front and back walls. The entire structure is conceived such that it can be dismantled and reassembled.

4.5.2 The cooling system

The cooling system integrated in the RP insertion will have to remove the thermal load from the sensors and the electronics. Moreover, to allow operation after high irradiation the RP silicon detectors will be operated at about -10°C to reduce the radiation induced thermally generated bulk current and to control the reverse annealing after high irradiation. Nevertheless given the geometry of the package it will be difficult to keep all modules at the same temperature. A spread of less than 10°C between the ten plates can be tolerated and does not represent a strong constraint. The major contribution to the thermal load of the whole system is given by the readout chips (VFATs). The total load per pot is about 20 W.

Because of the high radiation environment of the LHC tunnel, the main part of the refrigeration system is not installed near the RP but in the underground service area USC55 at IP5, a protected and always accessible place.

An evaporative fluorocarbon cooling strategy [16] has been adopted since it can transport fluid at ambient temperature over long distances (from USC55 near IP5 to the RP stations at 147 m and 220 m) without heat losses but only pressure drops which are still low and can be balanced by the compressors. The throttling of the fluid is done in the pot and is based on metal capillary
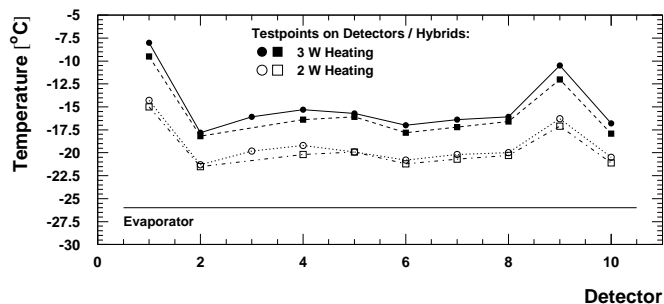
Figure 4.17: Temperature distribution measured on testpoints on the detectors (circular markers) and on the hybrids (square markers) for a heating power of 2 W and 3 W (open and solid markers respectively), compared with the evaporator temperature.

tubes. The C_3F_8 fluorocarbon dielectric fluid has been selected because it is non-flammable, non-conductive and radiation resistant. The heat transfer process is very effective because of the two phase flow regime.

The evaporative cooling system has been designed to guarantee a total cooling capacity of 1.2 kW and supply a global mass flow rate of 40 g/s to be uniformly shared between the 24 TOTEM Roman Pots. The fluid is supplied in liquid phase and at high pressure at the RP circuit inlet. The system is completely oil free and the process fluid adequately filtered to avoid any mechanical particle obstructing the lamination capillaries' inner section under irradiation.

Inside the Roman Pot the fluid medium flows through thin-walled copper-nickel pipes of 2.5 mm outer diameter. Two independent pipe evaporators supply fluid to the right and left side of the detector package. The evaporators are mechanically decoupled from the detector assembly at the inputs and outputs either by a bellow or by a spiral section. They are shaped in a double-S configuration and are squeezed in between the frame structure which foresees precisely machined grooves for this purpose. The evaporators are fed by capillary tubes that provide the throttling of the fluid. The coolant in gas phase is exhausted via larger diameter pipes. Both the capillaries and the exhausting pipes enter and leave the pot through two vacuum feed-throughs.

4.5.3   Tests on the thermo-mechanical prototype

A thermo-mechanical prototype has been assembled to characterise the conceptual design, the choice of the materials and the fluido-dynamic parameters of the cooling system. The VFAT chips on the hybrids were replaced with heaters with equivalent power density. The prototype was fixed to a vacuum chamber flange and inserted in an experimental vacuum chamber. All the connections of the pressure and temperatures sensors were read out through the vacuum feed-through. A capillary tube with an inner diameter of 0.55 mm was used.

The measurements showed that for the expected heating power of 2 W the temperature spread on a single hybrid card is within 3°C, and the maximum temperature difference between detectors is less than 10°C (figure 4.17).

The final length of the capillary, 1.5 m, is the result of an optimisation in view of obtaining a suitable pressure drop. The capillary will be coiled up in the pot to minimise the heat loss and the need of additional insulation.
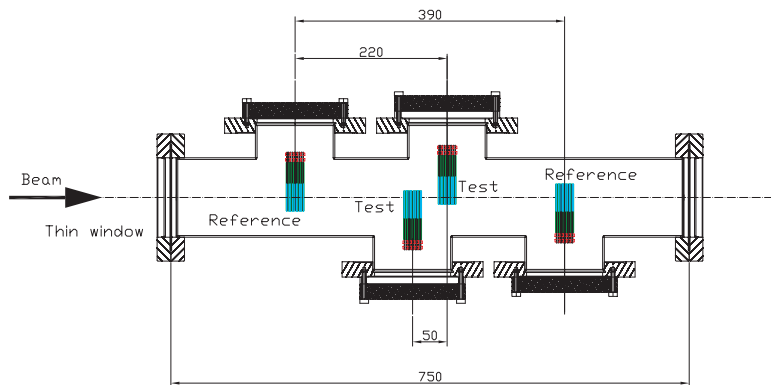
Figure 4.18: Arrangement of the test detectors and reference detectors with respect to the beam axis (dashed line) inside a test vacuum tube.

4.6 Detector performance

4.6.1 Detector tests with analog readout

4.6.1.1 Testbeam measurement of CTS detector performance

Edgeless silicon detectors have been tested in autumn 2004 with a muon beam in the SPS X5 area at CERN [13, 17]. The sensors had the final size and strip pitch of $66\,\mu$m. They were assembled into 4 packages each consisting of 8 detectors. The majority was read out with CMS's analogue APV25 chips [18] while a few were equipped with prototypes of TOTEM's own front-end chip, the VFAT, to test its trigger functionality. The packages formed a telescope placed inside a vacuum tube (see figure 4.18).

The outermost assemblies were used as reference to define tracks while the inner ones served as devices under test. The detector positions were measured with a precision of a few tens of microns. In the data analysis, the detector alignment was further refined with a global χ^2 minimisation algorithm to the precision of the order of $1\,\mu$m.

The detector setup was used to determine the resolution and the behaviour of the efficiency at the active edge of the test detectors. For these studies the detectors were operated at a temperature of around -10°C.

The CTS detectors in the test setup were biased at of 50 V, enough to overdeplete them and allow the full charge collection within the integration time of the readout electronics. Since more than 80% of hit clusters in these detectors consisted of one strip, the resolution of the detectors was close to the theoretical result when charge sharing is negligible, which is given by $d/\sqrt{12} = 19\,\mu$m, where $d = 66\,\mu$m is the strip pitch. A typical residual distribution is shown in figure 4.19 (left).

The efficiencies of the test detectors with respect to their geometrical coordinates were computed as fractions of accepted tracks. A track was considered as accepted when the test detector registered a hit within $\pm100\,\mu$m from the track. The combined reconstruction and alignment information was used to determine the position of the cut detector edges. The observed 10%–90% efficiency rise interval at the active edge was for all detectors smaller than $50\,\mu$m, and the re-
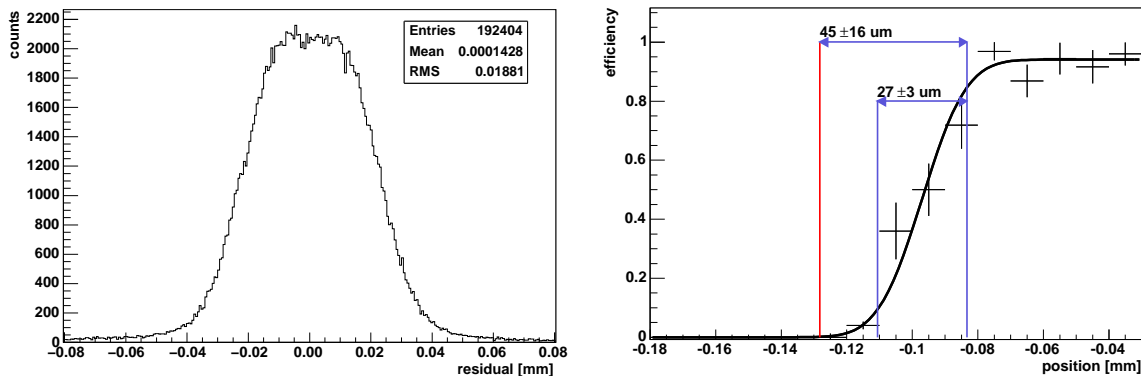
Figure 4.19: Left: residual distribution of a CTS test detector. The observed resolution was about 19 μm for all the test detectors, as expected from theory. Right: the efficiency of a CTS detector at the sensitive edge. The left-most vertical line indicates the reconstructed position of the physical edge, the other two vertical lines indicate the 10%–90% efficiency rise interval. The fit was performed with a Gaussian error function.
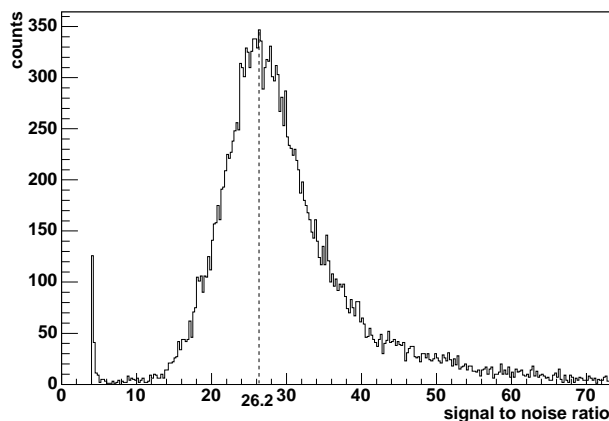
Figure 4.20: Signal-to-noise ratio distributions of a CTS test detector operated at a bias voltage of 100 V and at −11°C. The value of the most probable signal-to-noise ratio equals 26.2.

constructed distance between the cut edge and the position where 90% efficiency is reached was smaller than 60 μm. Figure 4.19 (right) shows the behaviour of the efficiency of one of the test detectors along the direction perpendicular to the cut edge.

Depending on the bias voltage and the detector thickness, the most probable value of signal-to-noise ratio was between 20 and 30. Figure 4.20 presents an example signal-to-noise distribution of the over-depleted test detector, operated at the bias voltage of 100 V.
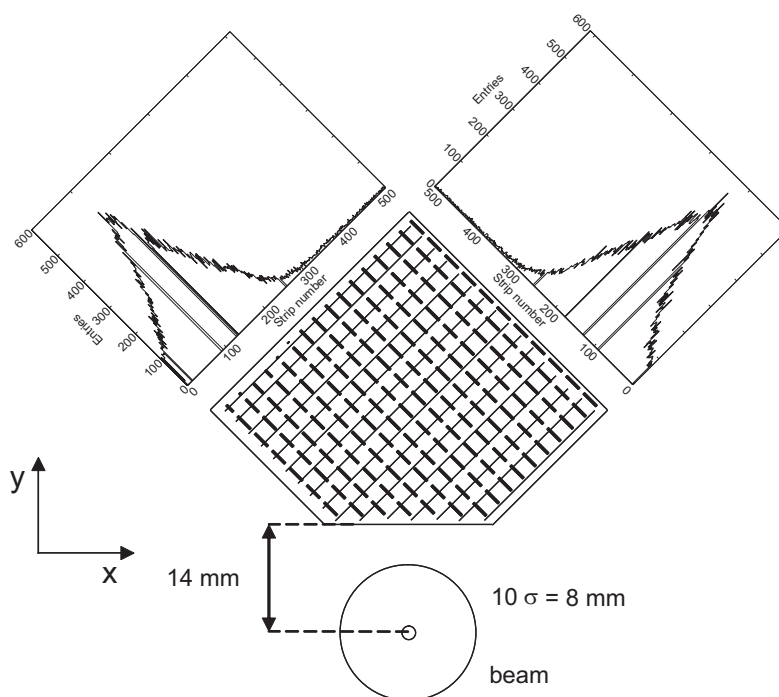
Figure 4.21: Profile of the SPS beam halo as seen by two orthogonal CTS detector planes at a distance of 14 mm from the beam centre. The data were taken with the bottom pot and the picture has been rotated by 180° around the beam axis for more convenience.

4.6.1.2 Full RP operation test in the SPS accelerator

The full operation of a Roman Pot unit prototype, consisting of a vacuum chamber equipped with two vertical insertions, was tested in a coasting beam experiment in the beamline of the SPS accelerator at CERN [11]. Each of the two insertions hosted four pairs of edgeless silicon detectors mounted back to back. In this early test, three pairs in each pot were used for tracking and were read out with the analogue APV25 chips. One pair was read out with a first prototype version of the digital VFAT chips delivering the fast-OR signal of all 512 strips used for triggering the data acquisition system in coincidence with the sum signal of the four pick-up electrodes of a beam position monitor located close to the detectors. Three different bunch structures were tested in the SPS accelerator: 1 single bunch in the accelerator ring, 4 bunches equally spaced, and 4 equally spaced trains of 4 bunches of 8×10^{10} 270 GeV protons with a revolution period of 23 μs. Detector data were taken with the two pots moving independently between 6 mm and 14 mm ($\sigma_{\text{beam}} = 0.8$ mm) from the beam pipe centre. Beam halo protons were detected at typical rates of 3 kHz. Figure 4.21 shows the halo profiles measured by two orthogonal detector planes of this pot. There were a few noisy channels on both detectors which have been removed from the profiles.
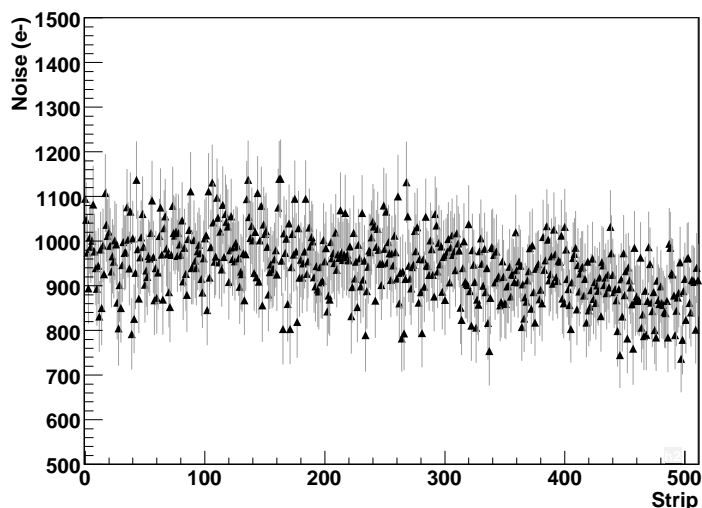
Figure 4.22: Noise at the different VFAT channels bonded to the edgeless detector biased with 150 V.
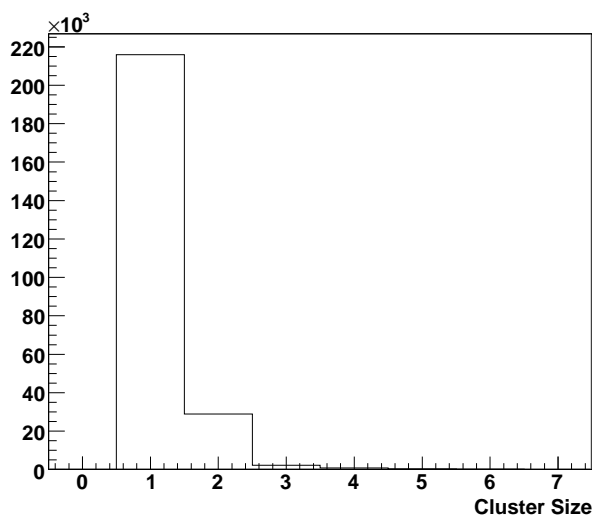
Figure 4.23: Cluster size in number of strips for particles perpendicular to the detector plane (detector bias: 150 V).

4.6.2 Operation of CTS detectors with VFAT chip

During 2007, the silicon detectors with CTS were tested in the H8 beam with the final electronics. Each detector was mounted on a final hybrid as described in section 4.4. Figure 4.22 shows the noise per strip, expressed in electrons, for all strips of one detector. The average noise and the rms are about 1000 and 100 electrons respectively. No outstandingly noisy channels were observed.

Tracks were defined in the H8 beam with a small size scintillator hodoscope, adjusted to the beam size. The cluster size for tracks, perpendicular to the test detector plane, is plotted in figure 4.23. In 90% of the cases, the cluster contains only 1 strip. This is a typical scenario for the forward protons in the TOTEM experiment since they are parallel to the beams and hence perpendicular to the detector planes within better than 1 mrad.
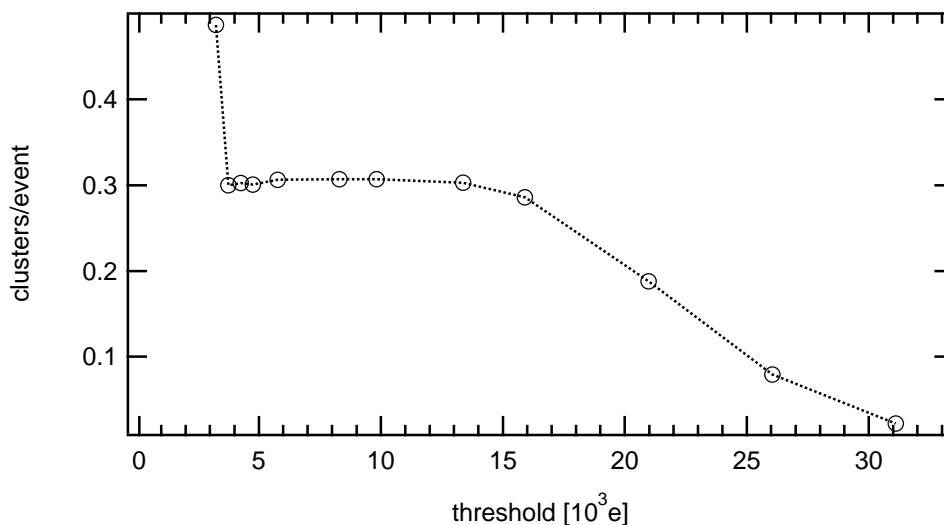
Figure 4.24: Threshold scan for one of the four VFAT chips of the Roman Pot Hybrid performed with a pion beam from the SPS. The number of clusters per triggered event is plotted versus the discriminator threshold expressed in electrons (detector bias: 150 V). The trigger was given by two scintillators in coincidence whose overlap covered slightly less than the whole CTS detector, about 3 times the area read out by the VFAT considered here, which explains the plateau level of $\sim 30\%$.

In order to demonstrate the detector response, several threshold scans were performed with a pion beam. In figure 4.24 the number of clusters per triggered event is plotted versus the discriminator threshold expressed in electrons. The noise starts to become visible at a threshold of 3000 electrons (three times above the average noise, see figure 4.22), at an occupancy level of 0.2% per strip. The wide plateau extends over a range of 10000 electrons. The maximum of the pulse height distribution can be estimated from the falling edge of the threshold curve. It corresponds to an efficiency loss of about 1/3 at a threshold of 21000 electrons, resulting in a signal-to-noise ratio in the range of 20 to 25.

4.6.3 Irradiation studies for CTS detectors

It is important to evaluate the radiation hardness of the edgeless Silicon detectors. However, there are no indications to believe that the performance of the edgeless devices with CTS after high radiation would degrade faster than the ones with standard voltage terminating structures provided that the edge current ($I_{\mathrm{CTR}} + I_{\mathrm{CR}}$) and the sensitive volume current (I_{BE}) whose dominant component is the bulk current, remain decoupled also after high radiation. To prove this assumption, edgeless silicon detectors have been irradiated at the neutron reactor TRIGA in Ljubljana at different fluxes up to 10^{14} 1 MeV n/cm^2. The edge current stays constant, independent of the radiation dose (figure 4.25, left). The bulk current I_{BE} increases proportional to the fluence Φ (figure 4.25, right). The damage factor α, defined as

$$\alpha = \frac{I_{\mathrm{BE}}}{\mathscr{V}\Phi},\tag{4.1}$$

where $\mathscr{V}$ is the detector volume, amounts to about 5×10^{-17} A/cm [19], which is in agreement with earlier measurements on devices using standard voltage terminating structures [20].
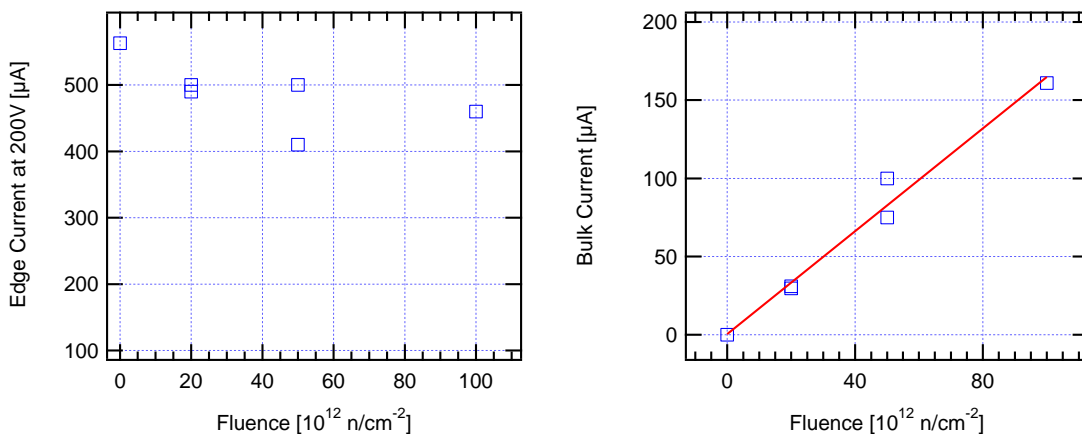
Figure 4.25: Left: edge current of CTS detectors biased at 200 V after different neutron fluences. Right: bulk current at full depletion voltage as a function of the fluence fitted with a linear function.
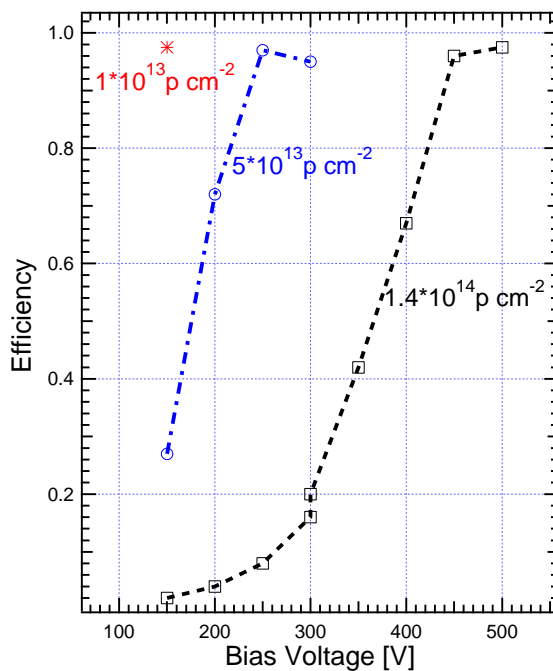
Figure 4.26: Efficiency of irradiated Edgeless Detectors with CTS at the working temperature of -18°C. The efficiency has been calculated by comparing the hits in the irradiated detector with the hits in a non-irradiated detector placed in front, along the beam axis.

More detectors have been irradiated with 24 GeV protons at CERN. The efficiency of these detectors as measured in the H8 test beam is given in figure 4.26 as a function of the bias voltage. Whilst a radiation up to 10^{13} p/cm^2 does not change the detector behaviour, stronger irradiated detectors (1.4×10^{14} p/cm^2) need a much higher bias voltage up to 450 V to be fully efficient. Presently, a radiation of 10^{14} p/cm^2 is considered as an upper limit for a functioning detector.
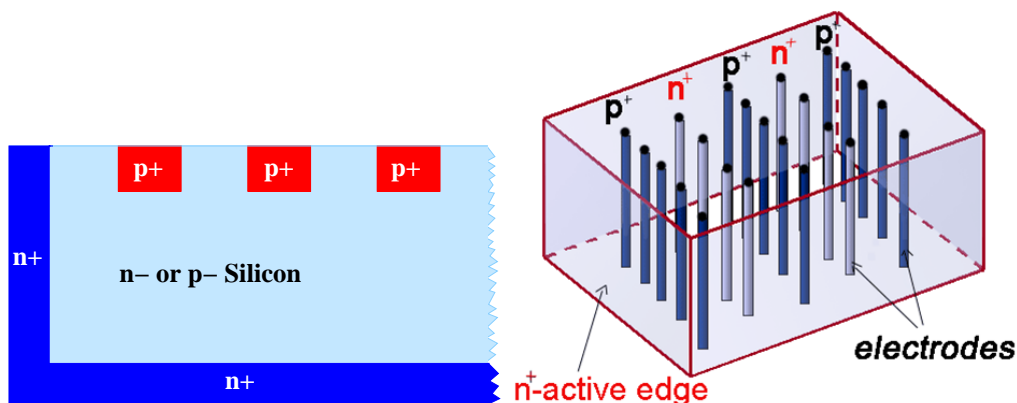
Figure 4.27: Left: sketch of a planar-3D detector. The edge (dark region) on the left hand side of the sketch, is an extension of the backside n^+ electrode and allows full control of the electric field lines at the edge. Right: sketch of a full 3D detector where the p^+ and n^+ electrodes are processed inside the silicon bulk. The edges constitute another n^+ electrode surrounding the 3D volume.

The above detectors were homogenously irradiated whereas in the experiment, due to diffractive protons, only a tiny area of a few mm^2 close to the sensitive edge is exposed to high proton fluence. Therefore, a non-irradiated detector was tested with bias voltages up to 500 V. Performance problems at this large bias voltage were not observed. However, a few strips showed a higher noise occupancy than at lower voltages.

Calculations of the diffractive proton flux hitting the detectors indicate that the present detectors will probably be alive up to an integrated luminosity of about 1 fb^{-1}. To cope with higher luminosities, TOTEM has initiated an INTAS project [21] to develop radiation harder edgeless detectors.

4.7 Alternative detector technologies: planar-3D and full 3D silicon

In addition to the planar silicon detectors with CTS, TOTEM is considering to equip some RPs partly with another novel type of "edgeless" silicon detectors: the planar-3D detectors [22], i.e. devices with a conventional planar microstrip interior and active edges as introduced with the full 3D detector technology [23]. In this configuration, the free edges of a planar detector are deep etched and n^+ dopant diffused in. Then the sensor is removed from the wafer again by etching, avoiding in this way the typical surface defects produced by saw cuts. In this way the edges of the sensor become an extension of the back-side n^+ electrode to the front side, as shown schematically in figure 4.27 (left). This enclosing n^+ electrode — the "active edge" — completely defines the electric field lines when a reverse bias voltage is applied. Also with this technology, the dead area which would be needed for guard rings in conventional planar detectors is reduced to no more than a few tens of microns.

Prototypes of planar-3D detectors have been tested in the 2004 testbeam together with the CTS detectors. Both the efficiency rise at the edge and the spatial resolution of the planar-3D detectors were measured to be very similar to those of the CTS detectors. However, these early

sensor prototypes had only a thickness of 235 μm and — due to a production problem — could only be biassed with voltages up to 30 V where they are not yet fully depleted. Both facts led to a most probable signal-to-noise ratio of only 11.5. Studies on more advanced samples of this detector technology are being continued.

On the quest for edgeless radiation-hard detector technologies, TOTEM has also conducted the first beamtest with small prototypes of full 3D active-edge detectors, as sketched in figure 4.27 (right) and described in [23]. The test results were very encouraging [24]. In particular, the 10-to-90% efficiency rise at the edge happens over a distance of only 18 μm, and the measured sensitive width of the detector is equal to the physical width within 10 μm. While the production of large-area sensors is still difficult at present, this intrinsically radiation-hard technology [25] is a promising upgrade option for future operation at highest luminosities.

Chapter 5

The forward telescopes

5.1 System strategy

The measurement of the inelastic rate, which is necessary for the total cross-section determination, is performed by identifying all beam-beam events with detectors capable to trigger and to reconstruct the interaction vertex. Monte Carlo studies have shown that a good detector coverage in the forward region is necessary for a complete measurement of the inelastic rate. The main requirements of these detectors are:

- to provide a fully inclusive trigger for minimum bias and diffractive events, with minimal losses at a level of a few percent of the inelastic rate;

- to enable the reconstruction of the primary vertex of an event, in order to disentangle beam-beam events from the background via a partial event reconstruction (mainly the tracks coming from the primary vertex);

- a detector arrangement which is left-right symmetric with respect to the IP, in order to have a better control of the systematic uncertainties.

The requirements for such detectors are somewhat different from those for detectors that must guarantee detection and reconstruction of each particle in the event, which has influenced the choice of the technology for T1 and T2.

The TOTEM forward telescopes cover a rapidity range of about 4 units and are installed symmetrically in the forward regions of CMS (figure 1.1) on both sides ("arms") of the IP:

- T1 ($3.1 \leq |\eta| \leq 4.7$) is made of 5 planes per arm, each consisting of 6 trapezoidal Cathode Strip Chambers (CSC), and will be installed in the CMS End Caps between the vacuum chamber and the iron of the magnet, at a distance of 7.5 to 10.5 m from the IP.

- T2 ($5.3 \leq |\eta| \leq 6.5$) is made of 20 half circular sectors of GEM (Gas Electron Multiplier) detectors per arm and will be installed between the vacuum chamber and the inner shielding of the HF calorimeter at an average distance of 13.5 m from the IP.

In addition to the measurement of the total inelastic rate, T1 and T2 will be key detectors for the study of inelastic processes either by TOTEM or by the joint CMS/TOTEM experiments [2]. At low luminosities ($\mathscr{L} < 10^{31}\,\mathrm{cm^{-2}s^{-1}}$):

- The integrated inclusive Single Diffractive (SD) and Double Pomeron Exchange (DPE) cross-sections can be measured, as well as their t and M_X dependence (where M_X is the mass of the diffractive system). SD and DPE events have a clean signature in TOTEM and can be triggered requiring at least one track in T1 or T2 in coincidence with the proton(s) detected in the Roman Pots.

- T1 and T2 contribute to the detection and measurement of the rapidity gaps in diffractive events, which may provide a complementary measurement of the fractional momentum loss of the surviving proton(s), as well as shed new light on the problem of the rapidity gap survival probability.

- The telescopes' coverage and granularity allow the measurement of the charged multiplicity in the forward region, providing important information for the cosmic ray physics community (mainly to tune their event generators). More details can be found in [26].

At higher luminosity, in the range $10^{31} < \mathcal{L} < 10^{33}\,\mathrm{cm}^{-2}\mathrm{s}^{-1}$, T2 can be used in the joint CMS/ TOTEM experiment for hard diffraction and forward physics studies. It can be used as a rapidity gap trigger in order to reduce QCD background in exclusive particle production in DPE events, as well as to help in very forward lepton identification in Drell-Yan pair production. The possibility of exploiting T2 track information in the study of rare processes such as single-diffractive proton dissociation into three very forward jets is still under investigation.

5.2 T1 telescope

5.2.1 Requirements and choice of detector technology

The T1 telescope, installed in two cone-shaped regions in the endcaps of CMS, detects charged particles in the pseudo-rapidity range $3.1 \leq |\eta| \leq 4.7$.

At $\mathcal{L} = 10^{28}\mathrm{cm}^{-2}\mathrm{s}^{-1}$ with a reduced number of bunches, the expected number of interactions per bunch crossing is expected to be 2.5×10^{-3} which translates to an inelastic interaction rate of about 1 kHz. The average number of charged particles per event in T1 is expected to be ~ 40.

The inelastic trigger plays an important role in the measurement of the total cross-section: one needs a minimum bias trigger with a very high and measured efficiency. Systematics in the measurement of the trigger efficiency will be studied using different trigger combinations and cross-checks of their stability during the measurement. The basic trigger elements (primitives) are arranged in a roughly pointing arrangement to perform, if necessary, a first level background suppression, and will be useful also to define the different sub triggers. To discriminate good beam-beam events from the background, which includes beam-gas interactions (pointing to different regions in z inside the beam pipe) and other machine backgrounds such as the muon halo (approximately parallel to the beam), TOTEM needs to reconstruct only a number of tracks sufficient to reconstruct the position of the interaction vertex and check that it is compatible with the interaction point.

A detector with a well-known technology to meet these general requirements is the multi-wire proportional chamber with segmented cathode read-out: the Cathode Strip Chamber (CSC).
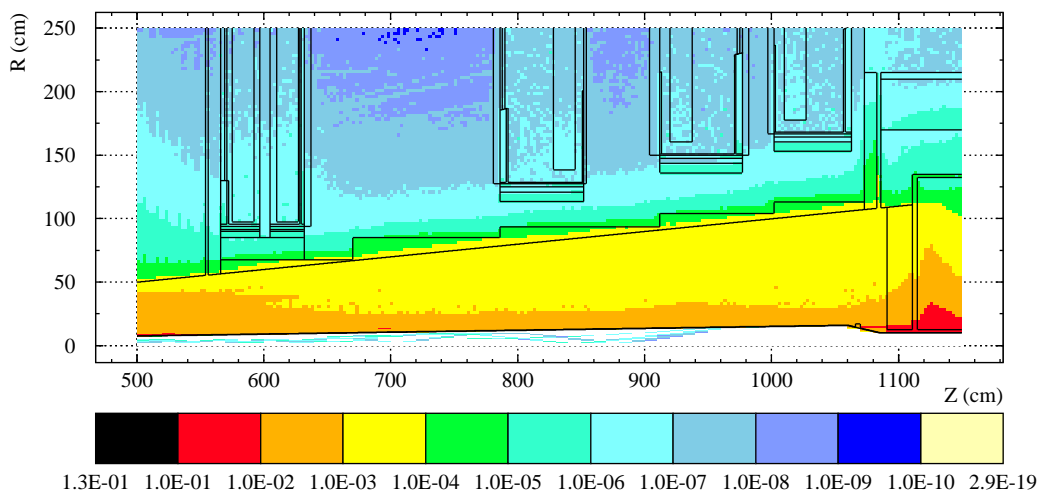
Figure 5.1: Expected accumulated dose, in Gy, from a simulation for 1 s at $10^{34}\,\mathrm{cm}^{-2}\mathrm{s}^{-1}$ luminosity, in the region occupied by T1.

These detectors, in which a single gas gap with segmented cathode planes allows a two-dimensional measurement of the particle position, are well understood (see for example [27]). Gas detectors of this kind are slow, but the response time for a CSC with a 10.0 mm gas gap is still compatible with the expected hit rates for TOTEM. Moreover, TOTEM's CSCs can be built in shapes suitable to cover the required area of the T1 telescope. They have small material densities which is important because they are positioned in front of forward calorimeters.

Another delicate parameter to consider is the behaviour in a high-radiation environment. Detailed simulations [28] estimate the flux of charged and neutral particles and the accumulated dose in the T1 region (figure 5.1).

The ageing properties of the TOTEM CSCs have been tested at the Gamma Irradiation Facility at CERN: two chambers have been irradiated, integrating a total charge on the anode wires of 0.065 C/cm, without showing any loss of performance, in agreement with tests performed by CMS [29]. This accumulated dose is equivalent to about 5 years of running at luminosities of $10^{30}\mathrm{cm}^{-2}\mathrm{s}^{-1}$. In the outer region of T1, where the cathode read-out electronics will be installed, the expected dose is lower by about two orders of magnitude.

5.2.2 Detector and telescope design

5.2.2.1 Detector geometry

The two *arms* of the T1 telescope, one on either side of the IP5, fit in the space between two conical surfaces, the beam pipe and the inner envelope of the flux return yoke of the CMS end-cap, at a distance between 7.5 m and 10.5 m from the interaction point. The telescopes will be the last to be inserted when closing and the first to be removed when opening the CMS detector.

Each telescope consists of five planes of CSCs, equally spaced in *z*, numbered as 1 to 5 from the closest (smallest) to the farthest (largest) from the interaction point. The vacuum chamber is
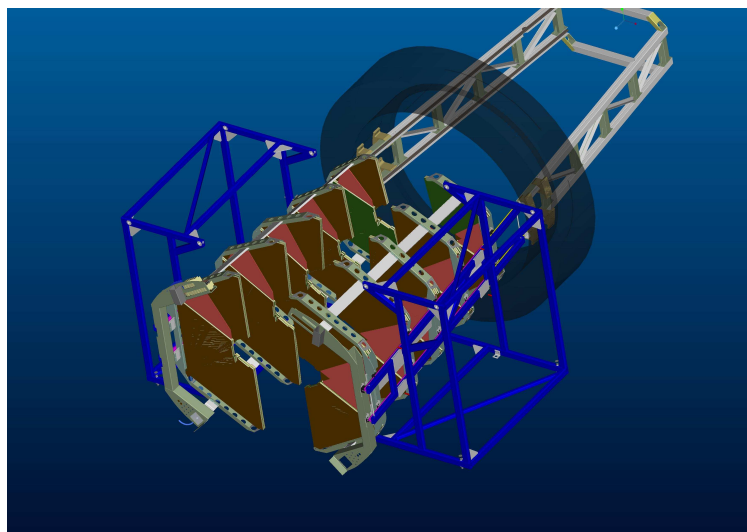
Figure 5.2: The two halves of one T1 telescope arm before insertion in CMS.

in place and aligned when the installation of T1 takes place: for this reason each telescope arm is built in two vertically divided halves (*half arms*) as depicted in figure 5.2.

A detector plane is composed of six CSC wire chambers covering roughly a region of 60° in ϕ and, as mentioned above, is split in two halves and mounted on different supports. Overlap is provided between adjacent detectors (also for the ones on different supports) to cover with continuous efficiency the approximately circular region of each telescope plane. In addition, the detector sextants in each plane are slightly rotated with respect to each other by angles varying from −6° to +6° in steps of 3°, the "reference" orientation being that of layer 5. This arrangement is useful for pattern recognition and helps to reduce the localised concentration of material in front of the CMS HF (Hadronic Forward) Calorimeter.

The conical volume reserved for the telescope contains also the mechanical support structure for installation inside the CMS end cap, which implies the construction of CSC detectors of 10 different dimensions (2 different types in each plane identified by the codes nG, nP). Figure 5.3 shows the layout of the 30 detectors of one arm.

5.2.2.2 Description of the T1 detectors

CSCs have been studied in detail in RD5 [27], and CSCs of very large dimensions have been built for ATLAS [30], CMS [31] and LHCb [32]. The TOTEM CSCs use basically the same technology developed for the other larger experiments, which we want to acknowledge here, tailoring specific parameters to the TOTEM requirements.

An exploded view of the different components making up a chamber assembly is shown in figure 5.4.

Two stiff panels of trapezoidal shape determine the flat surfaces of the cathode planes. A thin continuous frame is inserted between the two panels to keep with a good precision the two cathode planes parallel with a gap of 10.0 mm. The frame also has the function of defining a tight volume in which high purity gas will be flushed with a slight overpressure of a few g/cm^2.
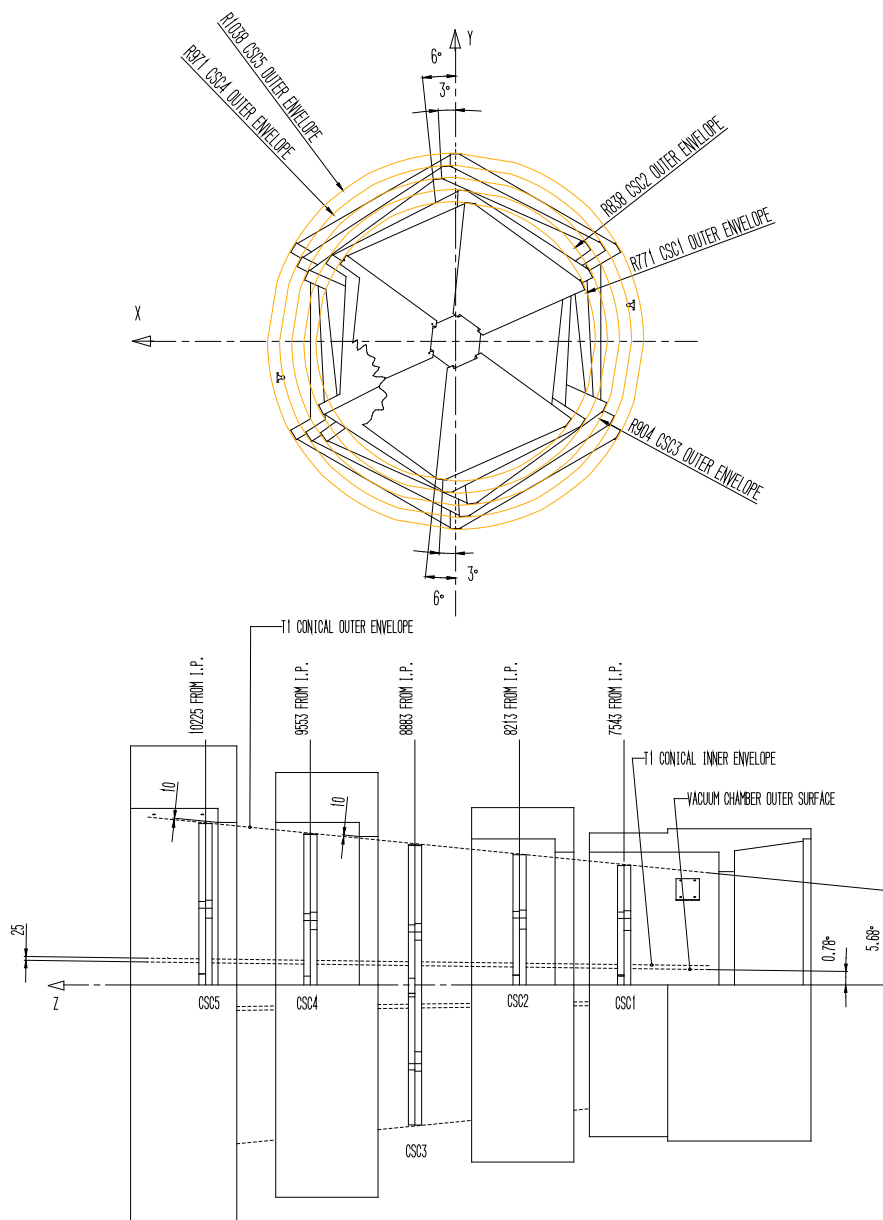
Figure 5.3: Layout of one T1 detector arm. The front view (left) shows the small rotations of the different planes.

The cathode panels are composite structures, sandwich panels of standard glass-epoxy laminates with a core of honeycomb, and provide the necessary stiffness. A study and tests were performed to optimise the thickness of both skins and of the core in the sandwich panel, in order to meet the stability requirements under load and minimise the material of the detector. The two panels are made with a 15 mm thick Nomex hexagonal honeycomb, enclosed between two 0.8 mm thick "skins" of fiberglass/epoxy laminate. Both skins are covered by a 35 μm thick copper layer. Cathode strips are etched and gold-plated with standard PCB technology on one of the two skins of a panel before its manufacture. The correct width of the gas gap is ensured by a G-10 frame glued
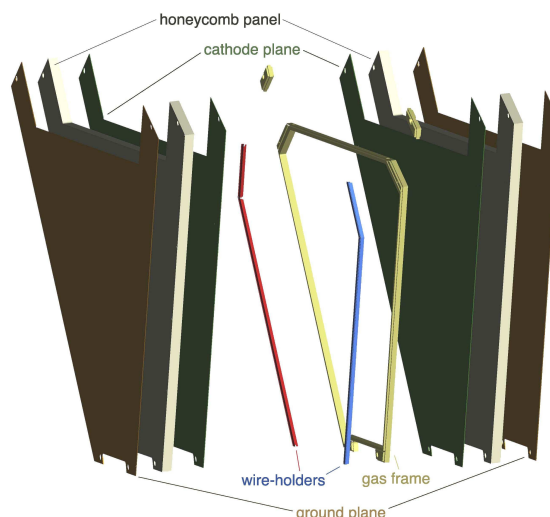
Figure 5.4: Exploded view of a TOTEM CSC detector.

to one of the two panels ("gas frame"). Besides acting as spacer, the frame guarantees gas tightness to the detector and gas distribution. The gas input and output lines enter the detector in the large side of the trapezoid and continue through a narrow duct machined through the full length of the sides: uniform gas distribution to the sensitive volume of the detector is achieved on each side via six equally spaced holes of 1.0 mm diameter.

The anode of the detector is composed of gold-plated (gold content of 6–8%) tungsten wires with 30 μm diameter, produced by Luma Metall;[1] the wires are strung parallel to the base of the trapezoid with a tension of 0.7 N at a pitch of 3.0 mm. The support for the wires ("wire holder" in figure 5.5) is provided by two printed circuit bars precisely machined to a thickness of 5.0 mm glued on the wire panel along the oblique sides of the detector and inside the gas volume. The wires are soldered and glued to pads on top of the bars; the pads are in turn electrically connected to tracks on the external region of the cathode plane. The first and the last anode wire, close to the inner and the outer edge of the detector, are field-shaping electrodes and have a larger diameter (100 μm). High voltage is applied on one side; on the opposite side the front-end card is directly soldered to pads connected to each single anode wire.

The cathode electrodes are parallel strips obtained as gold-plated tracks oriented at ±60° with respect to the direction of the wires and have 5.0 mm pitch (4.5 mm width and 0.5 mm separation). Each strip is connected to high-density connectors mounted outside the gas volume as shown in figure 5.5.

The orientations of the cathode strips and of the anode wires allow for three measurements in the plane of the position of the avalanche thus providing three measured coordinates for each particle track, which significantly helps to reduce the number of fake hits from random combinations ("ghosts").

The geometrical parameters of all 10 types of chambers are summarised in table 5.1; the numbers of anode and cathode read-out channels are listed in table 5.2.

---

[1]LUMA METALL AB, S-39127 Kalmar Sweden.
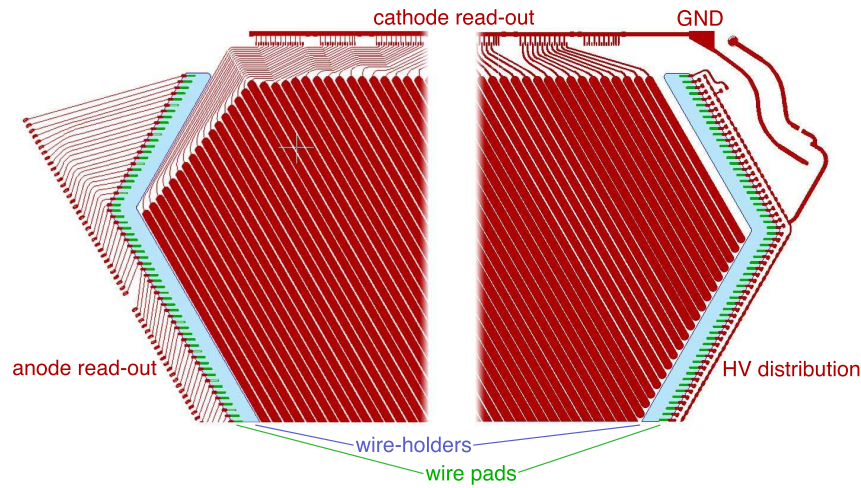
Figure 5.5: Cathode strips and wire-holder printed circuit boards.

Table 5.1: CSC geometrical parameters.

detector type	1G	1P	2G	2P	3G	3P	4G	4P	5G	5P
major base width [mm]	766	641	833	717	894	751	967	840	1016	957
minor base width [mm]	233	233	244	244	255	255	267	267	260	290
height [mm]	498	385	546	453	591	477	642	543	681	615
gas gap	10 mm									
anode wire spacing	3 mm									
anode wire diameter	30 μm									
cathode strip pitch	5 mm									
cathode strip width	4.5 mm									

Table 5.2: T1 read-out channels.

chamber type	1G	1P	2G	2P	3G	3P	4G	4P	5G	5P
wires per anode plane	165	127	181	150	196	158	213	180	226	204
strips per cathode plane	118	97	129	108	137	114	150	127	164	150
total anode channels	11124									
total cathode channels	15936									

5.2.2.3 T1 detector production

Immediately after assembly, the T1 CSC are submitted to a set of acceptance tests. The gas gain uniformity is measured by displacing a point-like ^{90}Sr radioactive source on the surface of a CSC operated at a high voltage of 3.6 kV, flushed with an Ar/CO_2 (50/50) mixture and measuring the current drawn by the power supply (figure 5.6).
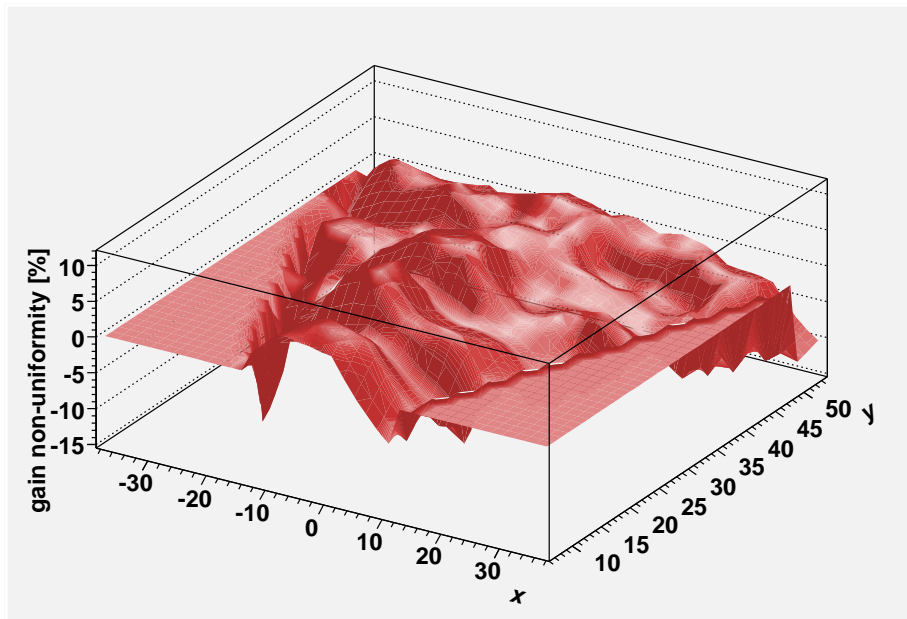
Figure 5.6: Gas gain uniformity deviations over a TOTEM CSC.

Figure 5.7: Completed CSC chambers for T1 in a test area at CERN.

After arriving at CERN, the detectors are submitted to further tests; figure 5.7 shows completed CSC chambers in the assembly laboratory.

The detectors that compose a half-plane are then secured to an aluminium frame with an overlap of the sensitive areas between them of few centimeters. Each of the five detector planes of one half telescope, plus a sixth frame that supports patch panels for the connections of the "services" (readout lines, trigger lines, high voltage, low voltage and gas and cooling lines), is fixed
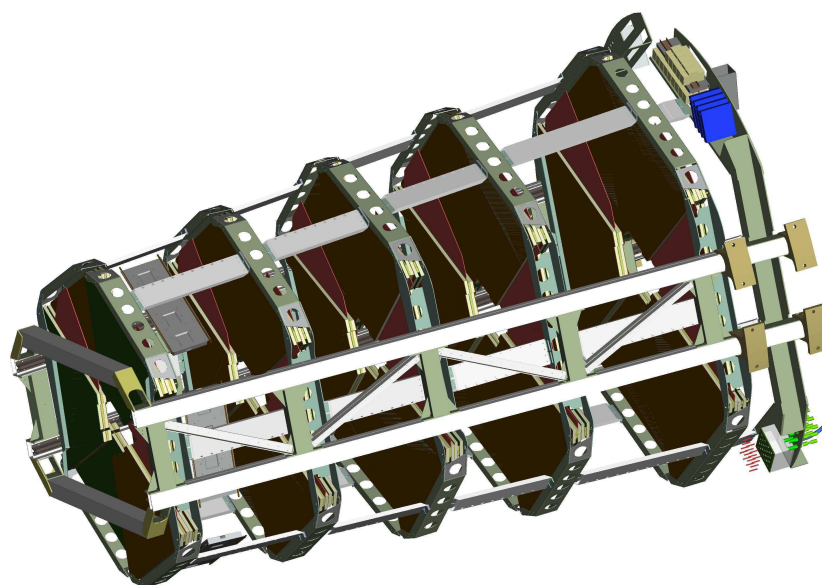
Figure 5.8: T1 assembly (one arm) with support structure. Some of the spacers between the detector planes and one support bar for the cathode read-out electronics are visible. On the right-hand side, the service support frame and the fixation plates securing the whole assembly to the internal surface of the CMS flux return yoke can be seen.

separately to the rails. The relative positions of the planes are defined by a series of appropriately positioned aluminium spacers. One telescope arm (two halves) in its final position on the truss is shown in figure 5.8.

5.2.2.4 Support structure and installation in CMS

The installation of the T1 telescope inside the CMS end-cap is delicate due to the tight geometrical constraints. Firstly, the zone is only accessible through the front circular opening and the installation can only be made when the end-caps are in place. Secondly, the beam pipe is also in place and the detector must be "closed" very carefully around it, avoiding contact with the two vertical rods supporting the pipe. Thirdly, the path of several CMS alignment laser beams traverse the volume of T1 and must be kept free.

Each of the two telescopes is therefore vertically divided in two halves, with independent support structures and services.

Two steel trusses are bolted to the third sector (YE3) of the CMS end cap, the same that supports the vacuum pipe, thus minimising any possible movement of T1 relative to the vacuum pipe as a result of the end cap deformation when the magnet is switched on. To guarantee the minimum acceptable deformation under load and at the same time minimise the cross-section of the structure, the trusses are joined together at the other end by two transverse bars. At installation T1 slides in position on rails mounted on each truss.
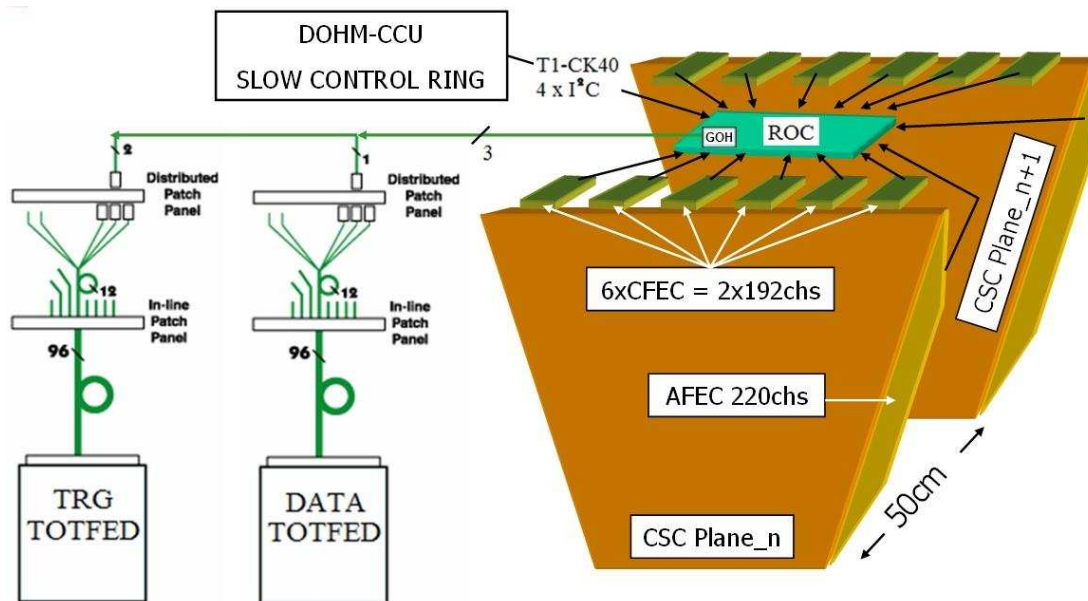
Figure 5.9: Overview of the T1 electronics system.

The half telescope is assembled and prepared for installation inside a specific structure with two rails similar to the truss ones. The half planes of T1 are mounted on this temporary structure, equipped with read out electronics, connected and tested. The structure also serves as support for the service racks of T1. For installation the structure is positioned on top of the HF calorimeter, the rails on the end cap and on the structure are aligned and the two telescope halves are slid into position inside the CMS end-cap. After this operation the CMS HF calorimeter can be raised to its final position, with the T1 external support structure still on its top.

5.2.3 T1 electronics system

The CSC anode and cathode signals are collected by custom-designed Anode Front-End Cards (AFEC) and Cathode Front-End Cards (CFEC), and conditioned by dedicated VLSI devices [33]. The serial digital data stream and the trigger signals coming out from the AFEC and CFEC are collected by the custom-designed Read-Out Card (ROC [33]) where they are serialised and optically transmitted to the DAQ system through a dedicated CMS Gigabit Optical Hybrid (GOH) [34]. The configuration and monitoring of the system is performed by the I^2C standard protocol distributed through the optical CMS Slow Control Ring SCR (DOHM [35] + CCUM [36]).

The T1 electronic front-end system globally involves 60 AFEC, 252 CFEC, 36 ROC, 96 GOH, 4 DOHM, 36 CCUM, while the T1 DAQ structure is based on a TOTEM custom board that can perform data (data FED) and trigger (trigger FED) signal analysis (section 7.2.2). An overview of the system is shown in figure 5.9.

5.2.3.1 AFEC

The AFEC is the board that collects and groups the anode wires of the CSC detector. Due to the conic structure of the telescope, ten different types of AFECs have been adapted to the chambers, for a total of 60 boards installed. The AFECs are soldered directly on the edges of the chambers, and the dimensions vary between 60 cm and 100 cm. The AFEC contains for every channel a double-stage high-pass filter isolating the high voltage on the wire from the readout, and adapting impedance and signal shape. The readout of up to 256 wires per chamber is carried out by two VFAT chips (section 7.1), each mounted on a VFAT hybrid (section 5.3.4) connected to the AFEC through a compact 130 pin connector.

Trigger information, permitting both individual TOTEM and CMS-integrated runs, is generated on the VFAT by grouping anode wire signals into 16 groups to form primitive hits for road reconstruction.

The connection of the AFEC to the ROC board, that represents the superior level of the DAQ chain, is realised by two high-density halogen free 50-wire cables.

5.2.3.2 CFEC

The CFEC is the board that collects and groups the cathode strip signals of the CSC detector. Each board processes 128 input signals with a passive network and delivers the outputs to a VFAT chip on a VFAT hybrid connected to the CFEC through a compact 130 pin connector. Due to the different sizes of the detectors, for each layer of the telescope a different number of CFEC boards are needed.

In order to improve the position resolution, a second version of the board has been designed and tested. In the new board the analog signal processing is performed by the BUCKEYE and LCT-COMP devices [37], developed for the CMS Muon project. The BUCKEYE chip includes a 5th order preamplifier, shaper and tail cancellation stages, while the LCT-COMP performs the discrimination of the BUCKEYE analog outputs. Each comparator output is serially coded on three bits (TRIADE) that contain the information about the side (right or left) of the strip where the charge is distributed.

The serial decoding of the discriminator outputs and the management of the slow-control features of the CFEC, like threshold settings, channel masking and calibration, are accomplished by an ACTEL Antifuse FPGA (A54SX32A)[2] device.

5.2.3.3 ROC

The ROC board represents the data, trigger and low voltage junction point of the T1 detector front-end boards and performs a similar function for the CSCs as the motherboard for the RPs. Each card is able to acquire data and trigger bits from two CSC detectors.

The board receives data from 16 VFAT hybrids hosted on the AFEC and CFEC cards, for a total of 2048 CSC signals.

The serial data stream received from the front-end is converted from LVDS to CMOS level, connected to the GOH mezzanine and optically transmitted to the DAQ system through the custom data FED board in the counting-room (section 7.2.2 and Ref. [38]).

---

[2]SX-A Family FPGAs, Actel Corp., February 2007.

Each detector has allocated up to 8 front-end connections, divided in two for the anodes and six for the cathodes. Only the AFECs produce trigger information. For each detector a total of 16 trigger bits are generated and transmitted to the TOTEM trigger system (trigger FED board) via a dedicated GOH optical link. The trigger information can also be merged with the data using a spare Gigabit Optical Link data channel and a special VFAT trigger hybrid.

For slow control, the CMS tracker and ECAL token ring system was adopted: similar to the RP system, a CCUM mezzanine mounted on the ROC forms a node in the slow control token ring. This system contains a skip fault architecture for additional redundancy based on doubling signal paths and bypassing of interconnection lines between CCUMs. Each CCUM controls the reset signal, three 8-bit general-purpose I/O ports and up to 16 I^{2}C serial line connections.

The 40 MHz master clock and the LHC fast commands are extracted in the ROC also from the token ring, and regenerated by CMS PLL devices (PLL25 [39] and QPLL). The distribution of the clock and the LHC fast commands to the front-end boards is implemented adopting a tree structure in order to minimise the skew and the delay time between different front-end receiver circuits.

In order to avoid missing data in case of failure of the master VFAT that enables the GOH serial data transmission, redundancy logic has been foreseen in the design of the ROC. The swapping of the master VFAT can be done via the general purpose I/O bits available through the SCR. As for the data, also the trigger bit transmission is modifiable changing the functionality of the logic with the SCR I/O connections.

A spy test port is foreseen on the ROC board, all the front-end connections are routed to dedicated connectors in order to plug a piggy-back mezzanine where a dedicated Xilinx FPGA (XC3S1500FG456)[3] and USB 2.0 logic can emulate the DAQ system chain.

5.2.3.4 High and low voltage supplies

The high and low voltage distribution for the CSC detectors is organised per half telescope arm (15 detectors). The high voltage system is based on the 24 channel A1550P board [40] (5 kV, 1 mA) and the CAEN SY1527 controller [41] placed in the counting-room.

The low voltage has to be applied locally, and thus the Wiener Marathon system [42] was chosen for its robustness against radiation and magnetic fields. One crate with 12 channels (2-8 V, 55 A) provides digital and analog power separately for half a telescope arm.

5.3 T2 telescope

5.3.1 Requirements and Choice of Detector Technology

The T2 telescopes, located at ± 13.5 m on both sides of IP5 (figure 1.1), detect charged particles in the pseudorapidity range of $5.3 \leq |\eta| \leq 6.5$. Generic requirements for the T2 (like for T1) include a fully inclusive trigger for diffractive events, hit pattern reconstruction for vertex finding to be used in discriminating against possible beam-gas background and for left-right symmetric alignment of telescopes for better control of the systematic effects.

The T2 telescope has been designed for good coverage of forward physics processes with varying beam conditions both at low luminosities (total cross-section and soft diffractive scattering)

---

[3]Xilinx Inc., *Spartan-3 FPGA family — v. DS099*, 25 May 2007.
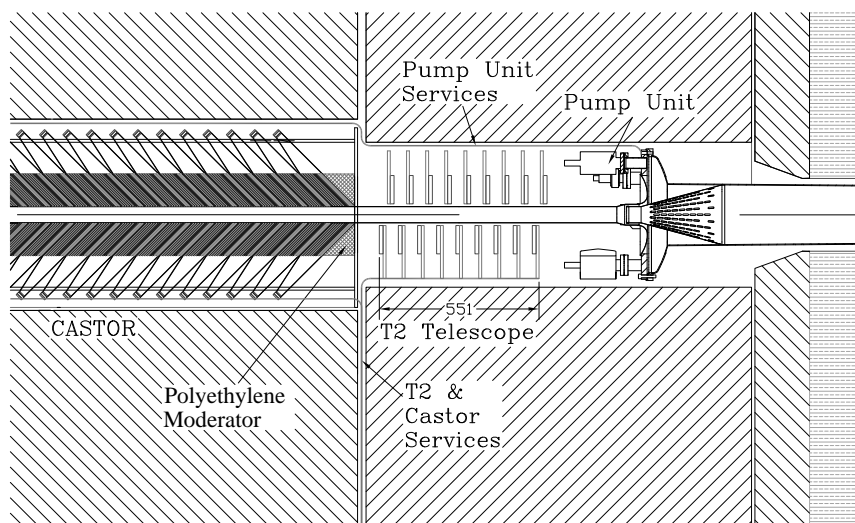
Figure 5.10: The location of the TOTEM T2 telescope within the shielding of CMS.

and at moderate luminosities (semi-hard diffractive scattering, low-x physics). Moreover, the T2 telescope is expected to operate up to luminosities of the order of 10^{33} cm^{-2}s^{-1} [1] where hard diffraction, heavy particle searches and physics beyond the standard model could be probed.

Due to the shape of the LHC vacuum chamber at the T2 location, an increased rate of particle-wall interactions is expected and had to be carefully considered. As a result, a compact detector array with a resolution in polar angle, $\Delta\theta/\theta$, matching the corresponding T1 resolution was adopted as a design criterium.

The gaseous electron multipliers (GEM) were selected for detectors of the T2 telescope thanks to their high rate capability, good spatial resolution, robust mechanical structure and excellent ageing characteristics. Invented a decade ago by Fabio Sauli [43] and studied by numerous research groups in experimental high energy physics, the GEM technology may be considered as a mature technology for the LHC environment. Excellent results of the COMPASS experiment [44], obtained during running periods extending over several years in high-rate environment, support also the choice of the GEM technology. Consequently, the COMPASS GEM design was adopted as a guideline for the GEMs of the TOTEM T2 telescope.

5.3.2 Detector Layout

5.3.2.1 The Telescope

The T2 telescopes are installed in the forward shielding of CMS between the vacuum chamber and the inner shielding of the HF calorimeter. There is a vacuum pump unit in front of T2 and the CMS CASTOR calorimeters behind it (figure 5.10). To reduce the neutron flux at T2 and HF, an additional polyethylene moderator will be installed between T2 and CASTOR. According the CMS simulations performed with the FLUKA Monte-Carlo package, the expected fluence of charged particles is around 10^6 cm^{-2}s^{-1} with the moderator installed [1].
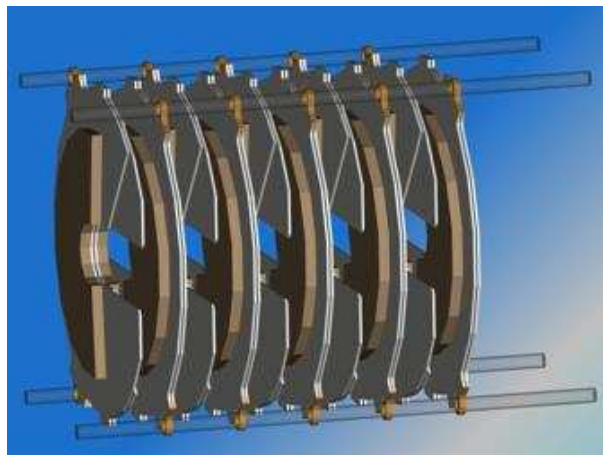
Figure 5.11: A CAD drawing depicting the arrangement of the 20 consecutive half-planes of Gaseous Electron Multiplier (GEM) detectors into one of the two T2 telescopes. In each detector layer, two GEM half-planes are slid together for maximal azimuthal angle coverage. With the ten double detector layers both high efficiency for detecting the primary tracks from the interaction point and efficient rejection of interactions with the LHC vacuum chamber is achieved.

In each T2 arm, 20 semi-circular GEM planes – with overlapping regions – are interleaved on both sides of the beam vacuum chamber to form ten detector planes of full azimuthal coverage (figure 5.11). The GEMs are installed as pairs with a back-to-back configuration. This arrangement of active detector planes allows both track coordinates and local trigger – based on hit multiplicities and track routes pointing to the interaction region – to be obtained. The material budget of T2 telescopes is minimised by using low-Z construction materials and honeycomb structures in manufacturing the GEM support mechanics.

5.3.2.2 T2 GEM Detectors

The shape of the GEM detector used in T2 telescope is semi-circular with an active area covering an azimuthal angle of $192°$ and extending from 43 mm up to 144 mm in radius from the beam axis (figure 5.12).

The design of the T2 GEM detector is based on utilisation of the standard GEM foils manufactured by the CERN-TS-DEM workshop. The foil consists of $50\,\mu$m polyimide foil (Apical) with $5\,\mu$m copper cladding on both sides. Due to the bidirectional wet etching process used by the workshop the shapes of the holes are double conical. The diameters of the holes in the middle of the foil and on the surface are 65 and $80\,\mu$m, respectively.

Three GEM foils are used as a cascade in one detector (figure 5.13) to reduce the discharge probability below 10^{-12} [45]. For the same reason the voltage divider supplying the voltages for the foils is designed such that the potential difference is gradually decreasing from the uppermost foil to the lowest one (nearest to the readout board). Moreover, the high voltage side of each foil is divided into four concentric segments for limiting the energy available for sparks (figure 5.14).
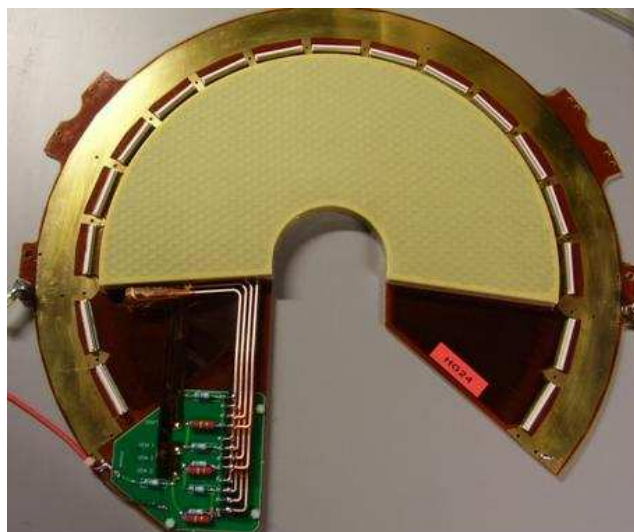
Figure 5.12: The TOTEM T2 GEM detector without front-end electronics and cooling pipes.
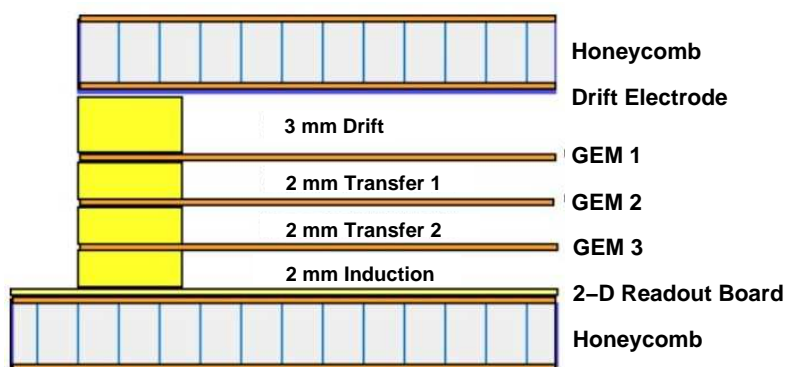
Figure 5.13: A side view of the T2 GEM detector structure: Three Gaseous Electron Multiplier (GEM) amplification stages are realised by three perforated and Cu-clad polyimide foils supported by honeycomb plates. A 3 mm drift space is followed by two 2 mm deep charge transfer regions (Transfer 1 and Transfer 2) and a 2 mm charge induction space. The large signal charges are collected, in two dimensions, by a read-out board underneath of the induction layer. The lightweight construction and support materials are chosen for low-Z material budget and mechanical robustness.

The segments are biased separately through high voltage resistors, enabling switching off the innermost segment if required. The ground sides of the foils are continuous.

At the design value of the operating voltage, the gas amplification over all the three foils will be roughly 8000, a value selected by the COMPASS experiment too. Consequently, the average amplification over a single foil is typically 20. The thickness of the drift space is 3 mm, whereas the transfer 1 and 2 and the induction gaps are all 2 mm (see figure 5.13). The corresponding electric fields over the gaps are approximately 2.4 kV/cm and 3.6 kV/cm, respectively.
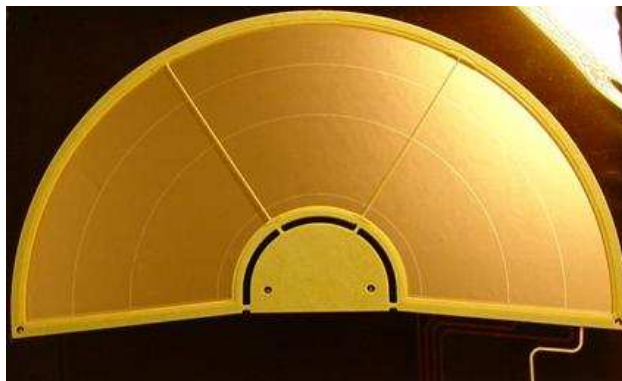
Figure 5.14: The T2 GEM foil glued to the support frame. The division of the electrode into four ring segments to minimise the energy available for discharges is visible.

The GEM foils are stretched and glued over supporting frames, which are manufactured by Computer Numerical Control (CNC) machining from fiberglass reinforced epoxy plates (Permaglas) with thicknesses of 2 mm. Two additional supporting spacers of thickness 0.5 mm are designed in the middle of the frames (see figure 5.14). Their position is slightly asymmetric to minimise dead areas. The drift frame is similar, except that the thickness is 3 mm and that no thin spacers in the middle of the frame are used.

An outgassing analysis of the frame material revealed emission of several organic compounds. Most of them were solvent-like remnants from the manufacturing process. One of these was toluene, which is known to cause ageing in ordinary wire chambers [46]. To remove the solvents from the material, all the frames were baked in a vacuum oven for several hours at a temperature of 80°C.

A polyimide foil with a copper cladding (5 μm) on a single side with thickness of 50 μm is used as a drift electrode which is glued to the front plate. The front and back plates are honeycomb structures, in which a honeycomb sheet of thickness 3 mm (Nomex) is sandwiched between two thin FR4 sheets of thickness 125 μm and enclosed inside a supporting frame made of the same material as the frames of the foils. The readout board is glued to the back plate.

A printed circuit board covered by polyimide foil with a pattern of strips and pads is used as a two-dimensional readout board. The rather complicated structure is manufactured partly by a commercial company and partly by a CERN workshop (TS-DEM group). The readout board contains 2×256 concentric strips for the radial coordinates and a matrix of 1560 pads for azimuthal coordinates and for the T2 local trigger (figure 5.15).

The strips lie on top of the pads and are isolated from the pads by a thin layer of polyimide, which is removed between the strips by wet etching (figure 5.16). The width and spacing of the strips are 80 and 400 μm respectively. To reduce the occupancy, the strips are divided into two parts, each covering 96° in azimuthal angle. The readout of the strips is located on both ends of the chamber.

The pads are divided into 65 radial sectors each containing 24 pads with sizes ranging from $2 \times 2 \, \text{mm}^2$ close to the vacuum chamber wall to $7 \times 7 \, \text{mm}^2$ at the outer edge of the semi-circular planes. The charge collected by the pads is read, with help of vias and strips on the backside of the board, at the outer edge of the readout board.
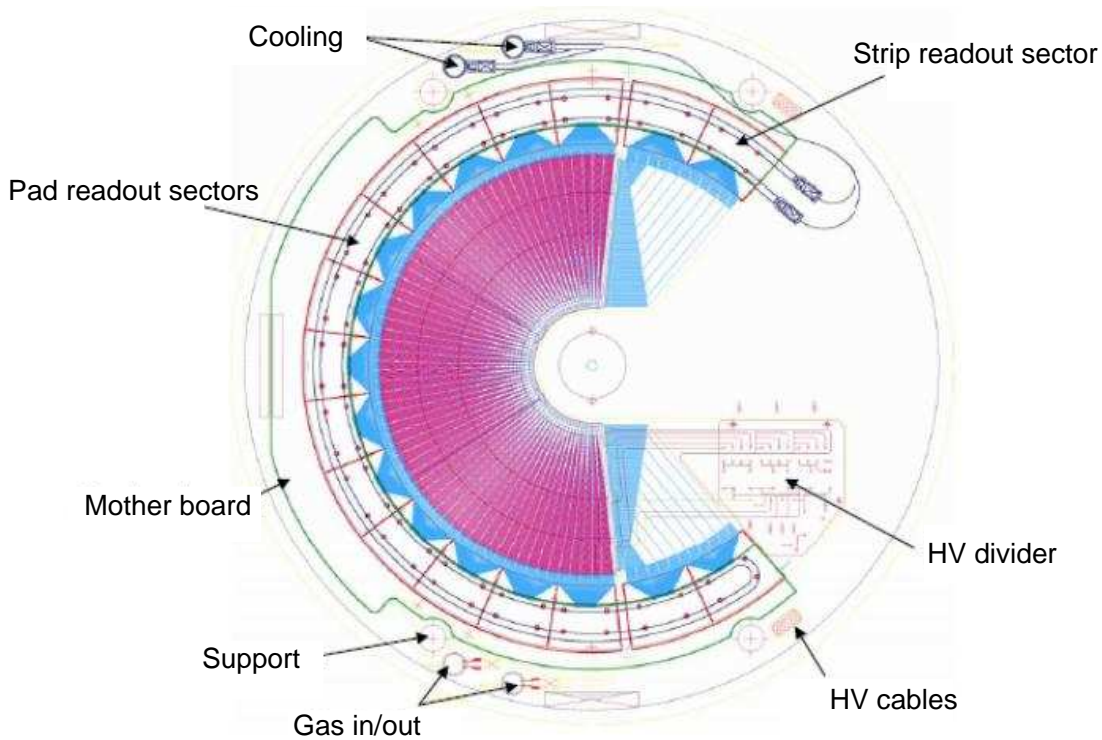
Figure 5.15: The design drawing of the TOTEM T2 GEM detector.
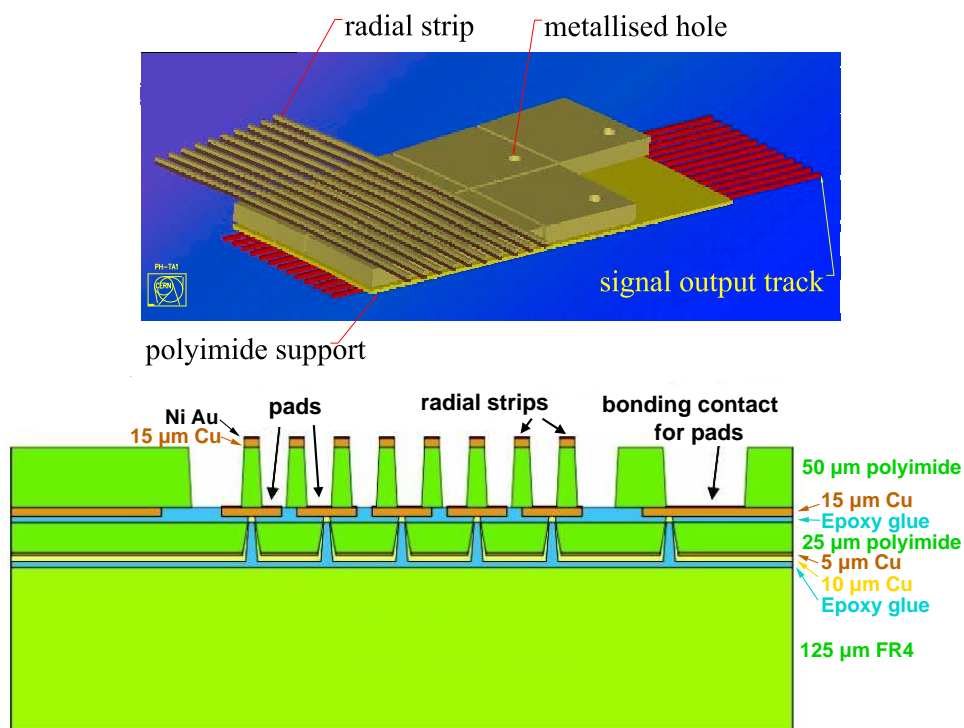
Figure 5.16: Detailed views of the strip/pad structure of the T2 GEM readout. Top: 3-dimensional view, bottom: cross-section.

Unlike in the COMPASS experiment, the readout electronics are connected to the readout board by connectors. No wire bonding on the readout board is required. SMD-connectors of 130 pins with 0.5 mm pitch are soldered directly on the board. Four connectors are required for the strip readout (128 strips per connector) and 13 for the pad readout. The pad connectors are hence used to read five sectors of 24 pads (120 pads), the other pins in the connectors are grounded.

The gas connectors are also installed on the readout board. The fill gas of the GEM (Ar/CO_2 70/30 mixture) is supplied through channels engraved in the fiberglass frame beneath the polyimide foil. The frames of the GEM foils contain also holes in two corners for a uniform distribution of the gas to the drift, transfer and induction gaps.

5.3.3 Detector Manufacture

The production of the required 50 individual GEM detectors (2×20 detector planes for the left and right T2 telescopes, 10 in reserve) was initiated in summer 2006 in Helsinki. Due to the harsh operating environment in the forward region, special care has been taken in devising efficient quality control processes both for the GEM components and their overall performance criteria.

The GEMs are almost exclusively manufactured in clean rooms of the Detector Laboratory where a dedicated assembly line for the large GEM detectors was set up. Although the production process is mostly based on manual assembly phases, some of the quality-control related tasks are made automatic. These include leakage current measurements of the GEM foils, optical inspection of the foils and search for broken or short-circuited strips/pads on the readout board.

An automatic leakage current measurement system for the GEM foils was devised and consists of a programmable electrometer, a special arrangement for electric contacts and a LabView based software package. The GEM foils are considered acceptable when the leakage current stays over half an hour below 0.5 nA at a test voltage of 500 V over the foil in dry atmosphere.

In addition to the leakage current measurement, the quality control of the GEM foils contains visual inspection of the foils and optical scanning of the whole foil surfaces. The aim of the scanning is to record the known defects of the foils for later use. A commercial flatbed scanner and an external background lighting setup are combined for automatic GEM foil scanning. The foils are scanned from each side with a resolution of 2400 dpi. Background light is utilised for spotting the holes in which the polyimide layer was incompletely etched or when the hole was entirely absent on the other side of the foil. In addition to finding defects on the surface of the foil, the system is also used for measuring the variation of hole sizes across the foil area.

Broken strips and short circuits between strips and pads may cause data corruption and additional noise in GEMs. These defects are easily seen in capacitance values of the strips and the pads. Due to the large number of channels (1560 pads and 512 strips), a special automated capacitance measurement system for the strips and pads of the GEM readout boards was developed. The system consists of a computer controlled x-y table, a programmable LCR-meter and a custom-made test board. The pad geometry, with pads growing larger when moving from inside out in radial direction from the beam vacuum chamber wall, is clearly seen in the resulting graphs. The measured variation of strip capacitances is relatively small.

In the finishing stage of the manufacturing process the basic characteristics of the GEMs filled with a gas mixture of Ar/CO_2 (70/30) are measured in the laboratory with the help of standard ^{55}Fe
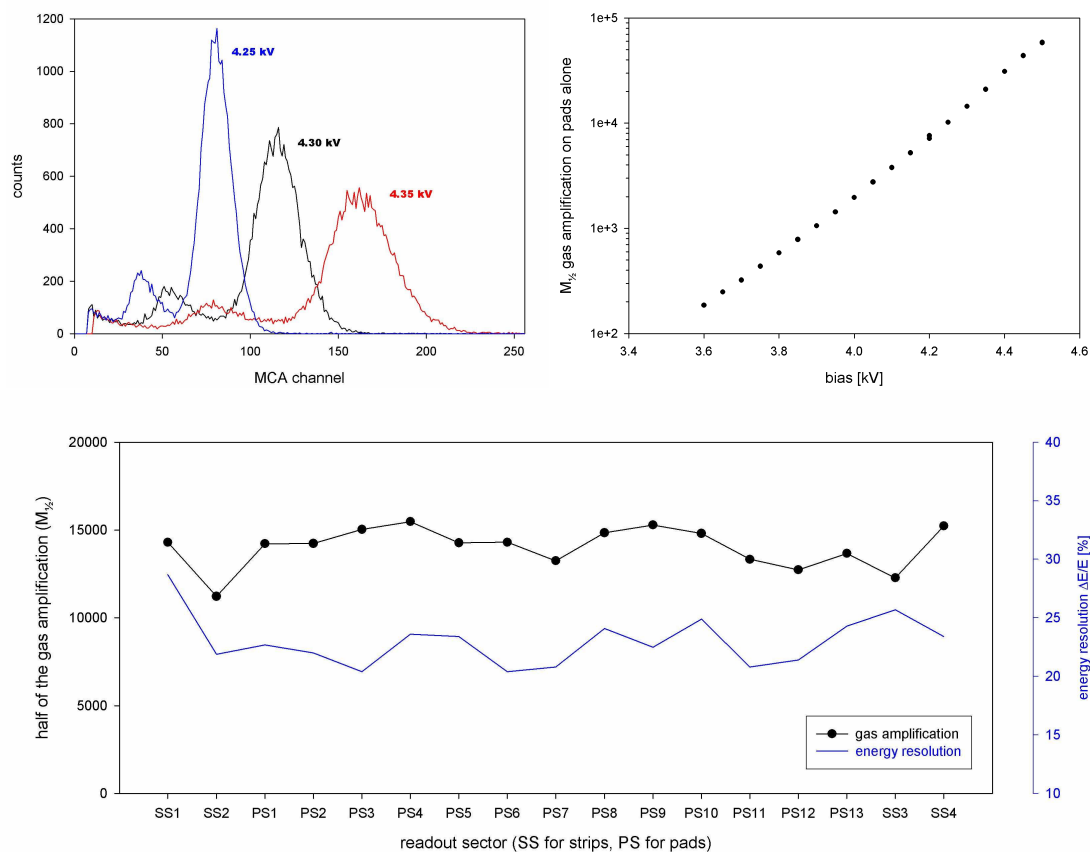
Figure 5.17: Examples of operational tests of the T2 GEMs with gas mixture Ar/CO$_2$ (70/30) done after the detector assembly: a) ^{55}Fe X-ray spectra at different bias voltages, b) a gas amplification vs. bias voltage, c) variation of the gas gain and the energy resolution over the readout sectors.

X-ray sources (5.9 keV). These consist of gas amplification and energy resolution measurement at different bias voltages and in different readout sectors (figure 5.17). All the GEMs are tested with a gas amplification up to 10^5, which corresponds to a gain one order of magnitude higher than the design value. Moreover, the characteristics of the GEMS and their readout electronics are tested in several beam tests during the years 2006-2007.

5.3.4 On-detector electronics

The T2 detector consists of 40 GEM detectors arranged in 4 quarters of 10 detectors. Each detector is read out by 17 VFATs 13 for the pads (120 pads per VFAT) and 4 for the strips (128 strips per VFAT). Each VFAT is mounted on its own VFAT hybrid (figure 5.18). All 17 VFAT hybrids of one GEM detector are mounted on a "horseshoe card" named after its physical shape (figure 5.19) The horseshoe cards of the 10 detectors of one T2 telescope half arm are connected to the so-called "11th card" which provides the interface to the outside world. A schematic view of the entire system is shown in Figure 5.20.

**Figure 5.18**: The TOTEM gas detector hybrid carrying one VFAT readout chip (under the cover).
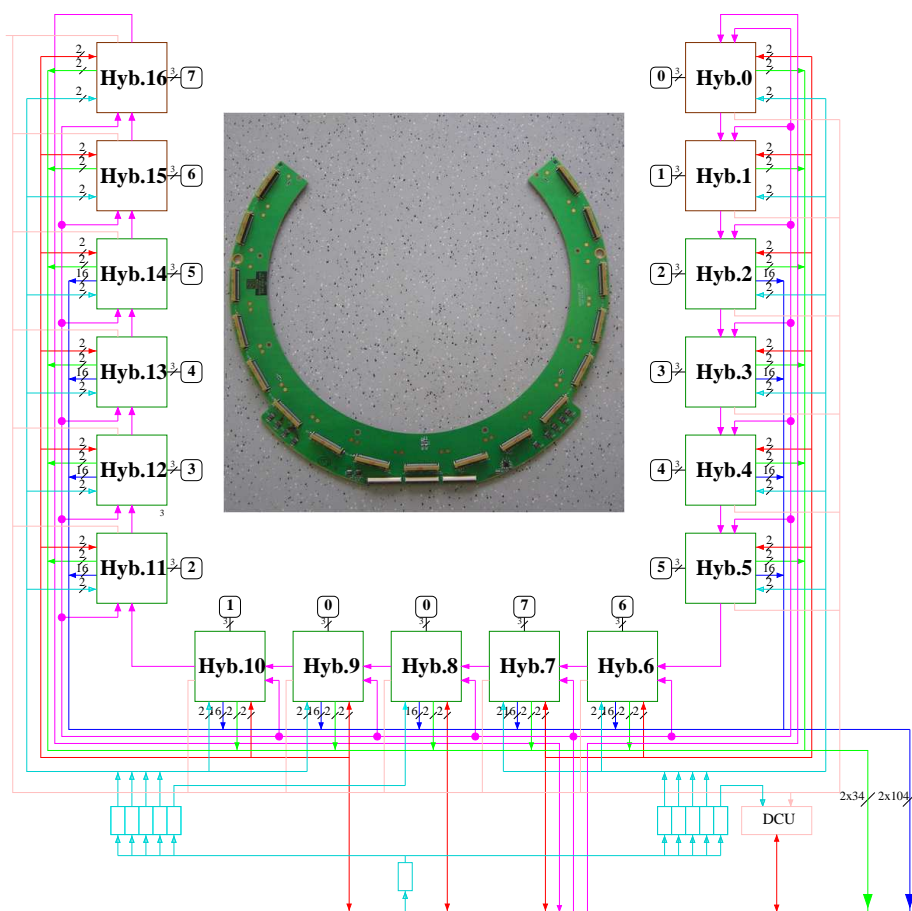
Figure 5.19: Architecture of the Horse-Shoe card (red for I²C lines, cyan for clock and trigger lines and LVDS buffers, pink for DCU and monitoring lines, blue for trigger hybrid outputs, green for data and data valid hybrid outputs, magenta for scan test lines, dark green for pad VFAT hybrids, dark brown for strip VFAT hybrids).
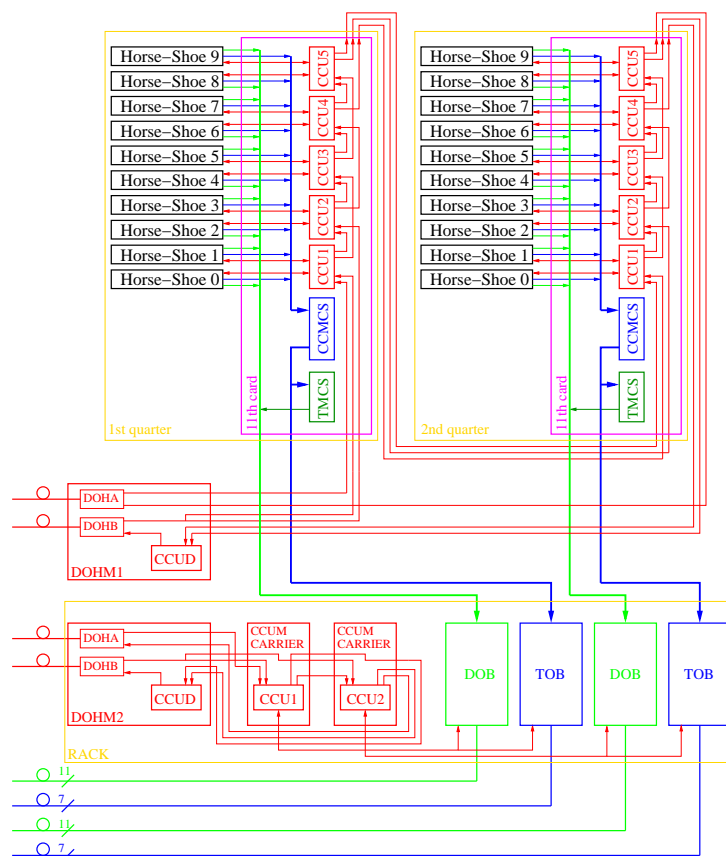
Figure 5.20: Architecture of the readout electronics of half of the detector (black for Horse-Shoe cards, magenta for 11th cards, red for CCUMs, DOHMs and control, clock and trigger lines, blue for trigger hybrid outputs, CCMCs and Trigger Opto-Boards, green for data outputs and Data Opto-Boards, dark green for TMCs and TMC outputs to Data Opto-Boards.)

The VFAT hybrids are linked to their horseshoe card by a 50-pin connector transmitting:

- precision data and trigger data from the VFATs to the horseshoe card, and

- clock, trigger and control signals, HV and LV power from the horseshoe card to the VFAT hybrids.

5.3.4.1 Data Path

The precision data (green lines in figure 5.20) and the tracking data (blue lines) originating from all hybrids of a T2 half arm (or quarter of the full telescope) are transmitted via the 10 horseshoe cards to the 11th card (magenta boxes in the figure) which performs coincidence analysis on the grouped trigger data coming from the VFAT fast-or logic. For the latter purpose, the 11th card houses 13 mezzanine cards equipped with a coincidence chip (CCMCs, blue boxes).

Both full-precision data as well as results of the trigger coincidence logic are sent from the 11th card to Opto-Boards equipped with GOHs (Gigabit Optical Hybrids) for optical transmission

to the counting-room. The extreme radiation levels in the T2 station preclude the use of optohybrids on the 11th card, which therefore had to be placed in a rack on the GEM platform just outside the shielding of the detector. Data transmission to the optohybrids is carried out electrically using LVDS signals over about 6 metres.

Since one GOH can handle up to 16 data lines, the $10 \times 17 = 170$ precision data lines from a T2 half arm are regrouped in the 11th card and sent to 11 GOHs mounted on one Opto-Board ("Data Opto-Board", green boxes "DOB" in the figure).

The $13 \times 8 = 104$ trigger outputs of the CCMCs are also regrouped and sent to 7 GOHs mounted on a second Opto-Board ("Trigger Opto-Board", blue boxes "TOB" in the figure).

In order to include trigger information into the data stream, a second branch of the 104 trigger signal lines is regrouped into two sets of 64 and 40 signals respectively and sent to 2 Trigger Mezzanine Cards (TMCs, dark green boxes in the figure) equipped with a VFAT chip. Each TMC generates a data stream containing trigger information that is sent to the Data Opto-Board together with the output data from the VFAT hybrids.

For the whole T2 system 8 optoboards are foreseen, 4 on either side, 2 for each half arm, one for tracking data and one for trigger data.

5.3.4.2 Controls

A Detector Control Unit (DCU) on the horseshoe card monitors temperature, analog and digital power supply voltages, and the output voltages and currents generated in the DAC integrated in the VFAT chips. The DCUs are controlled via I^{2}C links by Communication and Control Units (CCUs), each of them mounted on a CCU mezzanine card (CCUMs) on the 11th card. With 1 CCU per 2 horseshoe cards, each 11th card is equipped with 5 CCUs. The 2×5 CCUs on the two 11th cards of each T2 arm communicate with the control token ring via 1 Digital Opto Hybrid Module (DOHM). See also section 7.2.1.

The controls for the Opto-Boards are generated by two additional CCUMs mounted on CCUM carriers in the rack on the GEM platform outside the detector shielding. These CCUMs are connected to a second DOHM for communication with the control token ring.

The clock signals and trigger commands for the Horseshoe cards, the TMCs, the CCMCs and the Opto-Boards are distributed by the CCUMs after extraction from the control token ring.

5.3.4.3 Power Supplies

Two 11th cards and the 20 connected horseshoe cards are powered by a 12-channel Wiener Power Supply. Eight channels are used for analogue and digital power supply voltages of odd and even Horse-Shoe cards connected to the two 11th cards. Two other channels are used to power the first DOHM and the CCUMs in the 11th cards and the second DOHM, the CCUM in the CCUM carriers in the rack and the Opto-Boards respectively. Two channels are used as spares.

5.3.5 Detector Performance

Some of the TOTEM GEM detectors underwent several tests in a laboratory setup as well as in an SPS testbeam. The aim of these tests was to verify the performance and quality of the GEM detectors, the optimisation of the noise level measured with the TOTEM VFAT readout chip.
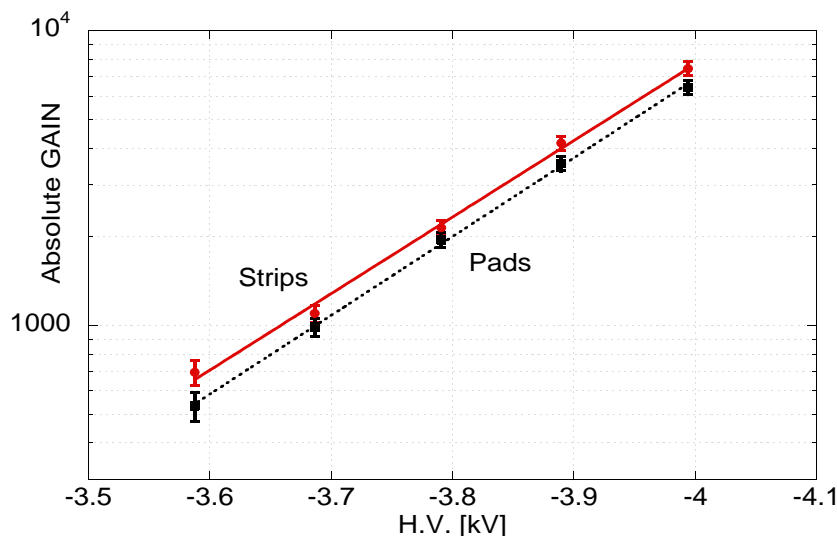
Figure 5.21: Absolute Gain calibration as a function of the applied High Voltage for strips (solid) and pads (dashed). This calibration curve was obtained with a Cu X-ray tube source, by measuring the X-ray interaction rate in the gas and the current collected by strips and pads.
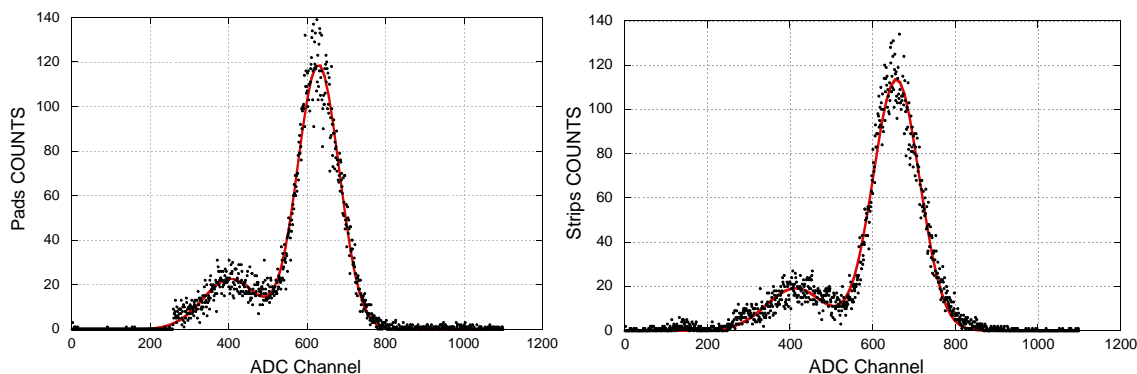
Figure 5.22: Cu X-ray spectrum as measured with a group of 48 pads (left) and with a group of 16 strips (right) on a GEM with a high voltage of -4 kV.

The absolute gain calibration curve for strips and pads irradiated by a Cu X-ray tube is shown in figure 5.21 as a function of the High Voltage applied. The comparison of the results of this test for different positions on the sensitive area of each detector and between different chambers, is in agreement with the expectations.

Figure 5.22 shows typical spectra obtained with a Cu X-ray tube, from which we can extract information about energy resolution (figure 5.23, left) and charge sharing between strips and pads (figure 5.23, right). These spectra were obtained with a 142IH ORTEC charge preamplifier and an ORTEC 450 research amplifier while the detector was powered with a HV of -4 kV.

Tests of GEMs equipped with the final TOTEM readout chip VFAT have been done to study the combined performance. Figure 5.24 shows the noise level for some strips (left-hand and mid-
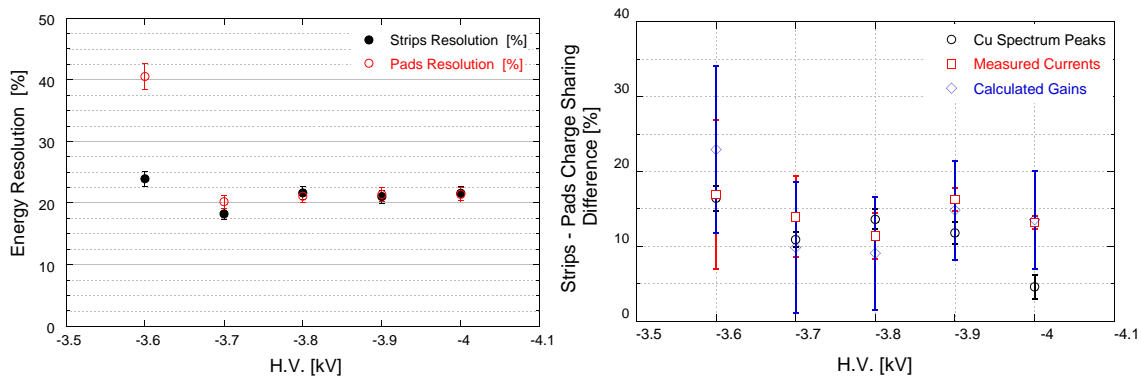
Figure 5.23: Left: energy resolution for strips and pads measured on the Cu $K\alpha$ (and $K\beta$) emission peaks as a function of the applied HV. Right: charge sharing between strips and pads (open circles), as obtained by the relative difference between the positions of the Cu $K\alpha$ peak of strips and pads obtained from spectra analogous to the ones in figure 5.22. Also shown are the relative differences between the currents collected from strips and pads (open squares), and between the gains (open diamonds).
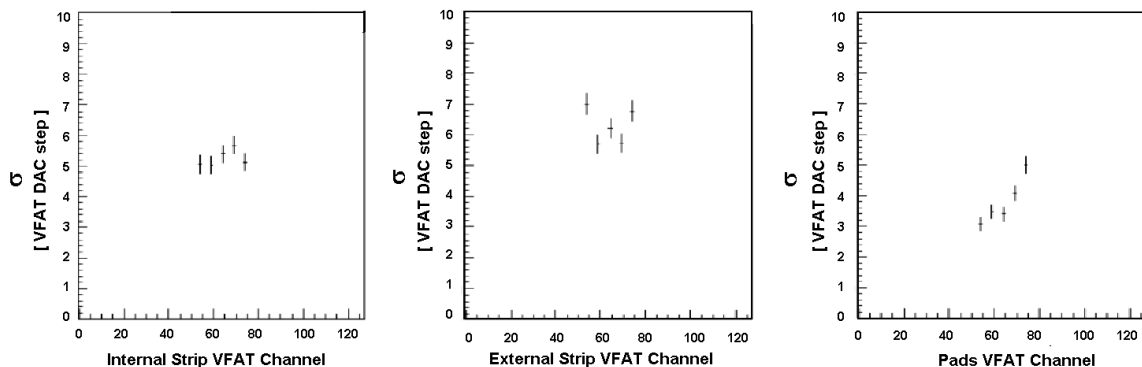
Figure 5.24: GEM read out by VFAT: noise σ of a group of internal strips with radii in the range $42.5\,\mathrm{mm} \lesssim r \lesssim 93.3\,\mathrm{mm}$ (left), external strips with $93.7\,\mathrm{mm} \lesssim r \lesssim 144.5\,\mathrm{mm}$ (middle), and a sector of pads (right), obtained with the calibration pulse scan available for the VFAT testing procedure. One VFAT DAC step corresponds to about 600 electrons.

dle plot) and pads (right-hand plot) obtained by varying the VFAT calibration pulse amplitude controlled by a Digital-to-Analog Converter (DAC), while keeping the threshold constant (see section 7.1, figure 7.6). An rms noise of $\sigma_{\mathrm{noise}} \approx 5\,\mathrm{DAC}$ units corresponds to about 3000 electrons. The pad noise clearly increases with the pad capacitance given in figure 5.25.

The CERN SPS beam test was important for understanding the response of the electronic readout chain to the typical signals of the GEM.

Events were triggered with two aligned scintillation counters of $5 \times 5\,\mathrm{cm}^2$ size, positioned up- and downstream of the GEM chambers under test.
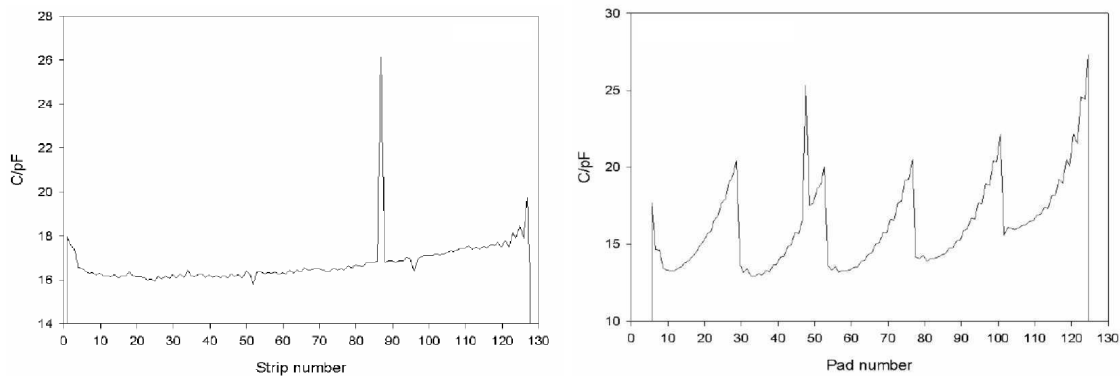
Figure 5.25: Capacitance measurement for strips (left) and pads (right). The spikes are caused by shorts between strips and pads.
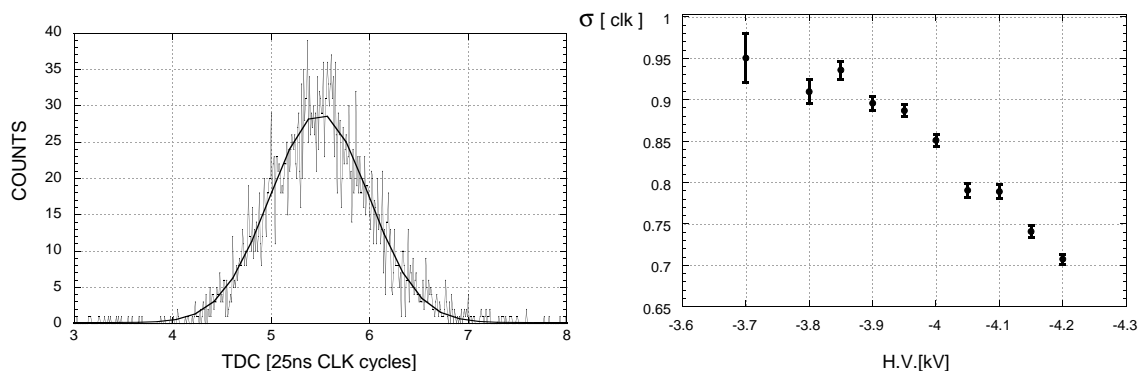
Figure 5.26: Left: distribution of the GEM VFAT trigger time with respect to the scintillator trigger time, measured with a TDC. Right: width σ, expressed in clock cycles, of the previous time distribution as a function of the high voltage.

Figure 5.26 (left) shows a measurement of the time difference between the GEM trigger signal and the scintillator trigger (asynchronous to the 25 ns clock), obtained with a TDC unit. The spread of this distribution, defining the time resolution of the GEMs, is shown in the right-hand plot as a function of the high voltage. As expected, increasing the voltage leads to a higher electric field and hence a shorter signal rise time with less time walk and a better time resolution.

The trigger time distribution extends over several clock cycles of 25 ns. Therefore, upon receiving a trigger, the readout has to accept signals within a time window covering several clock cycles, in order to avoid missing hits. The VFAT can accomplish this task by storing each hit in a programmable number of subsequent 25 ns bins of its memory (cf. section 7.1). An alternative approach for ensuring full efficiency is the reduction of the signal rise time by either increasing the electric field in the GEM or by adding CF_4 to the gas mixture.

Figure 5.27 shows the cluster size distribution for strips and pads at the typical HV of -4 kV. In figure 5.28 the mean cluster size is shown as a function of the high voltage and the VFAT threshold. The cluster sizes found are compatible with the results obtained by simulation.
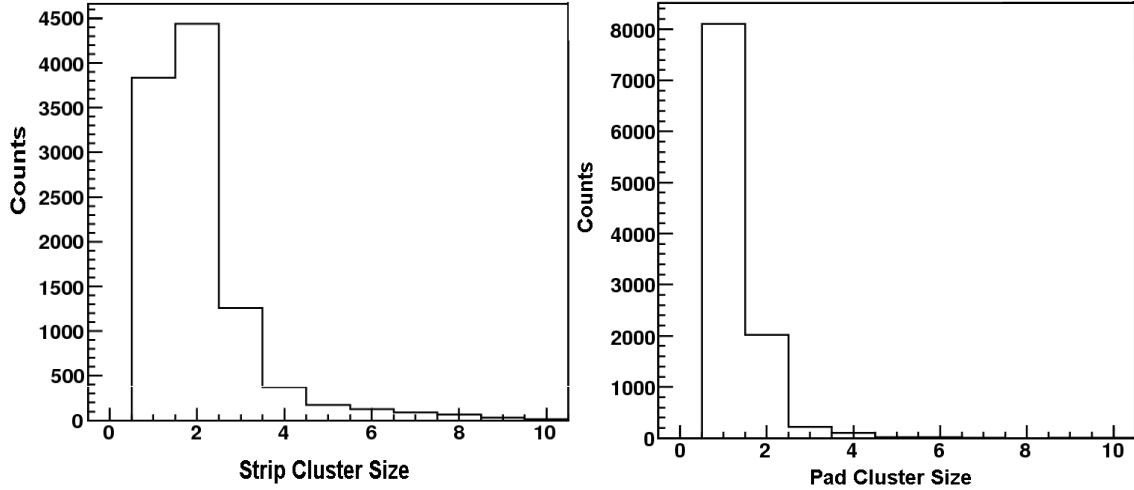
Figure 5.27: Strip and pad cluster size at HV $\approx -4.0\,$kV, with a threshold of 40 DAC steps (or 24000 electrons) and a signal sampling time window of 2 clock cycles in the VFAT.

The cluster size distribution has an impact on the spatial resolution of the detector. For the operating parameters chosen for the tests underlying figure 5.27, pad clusters consist predominantly of only one pad, which leads to a resolution of $p/\sqrt{12}$ (where p is the pad width), ranging from $2\,\text{mm}/\sqrt{12} \approx 580\,\mu\text{m}$ to $7\,\text{mm}/\sqrt{12} \approx 2\,\text{mm}$. The strip clusters on the other hand contain mainly one or two strips, with approximately equal probability. Since tracks passing near the centre of a strip produce preferrably 1-strip clusters whereas tracks passing between two strips will rather give 2-strip clusters, the resolution will be better than for a pure 1-strip cluster population. While the precise value of the resolution depends on details of the charge sharing mechanism, one can expect it to lie in the range from $0.5\,d/\sqrt{12} \approx 58\,\mu\text{m}$ to $d/\sqrt{12} \approx 115\,\mu\text{m}$, where $d = 400\,\mu\text{m}$ is the strip pitch. In the testbeam setup at hand, no external reference detector was available, which excludes a direct measurement of the resolution. However, with the hit measurements in two GEM planes and an approximate knowledge of the beam parallelism, a very rough consistency check is possible. Figure 5.29 shows the distribution of the radial distance between the strip cluster centres belonging to projective track hits in the two GEM planes with a distance $\Delta Z_{\text{GEM}} = 395\,\text{mm}$ along the beam. The observed standard deviation, $\sigma_{\text{obs}} \approx 235\,\mu\text{m}$, of this distribution can be decomposed according to the relationship

$$\sigma_{\text{obs}}^2 = 2\sigma_{\text{GEM}}^2 + \Delta Z_{\text{GEM}}^2 \sigma^2(\theta_{\text{beam}}). \tag{5.1}$$

Solving (5.1) for the angular spread of the beam, $\sigma(\theta_{\text{beam}})$, yields a value between 0.43 and 0.56 mrad which is well consistent with expectations for this beam.
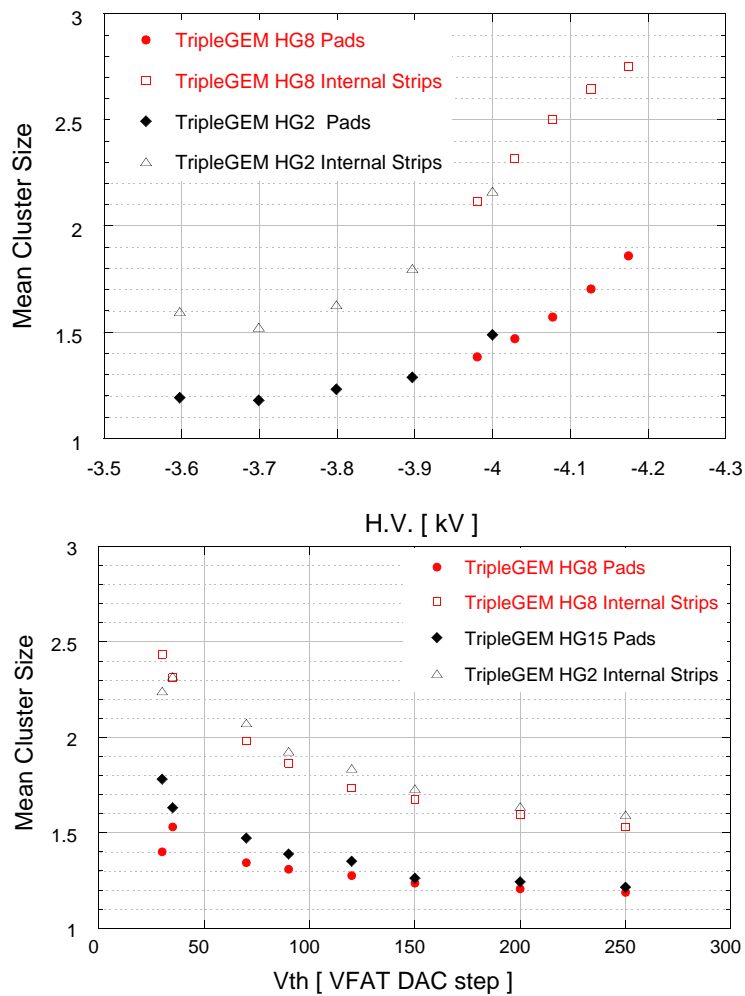
Figure 5.28: Cluster size for strips (open marker) and pads (filled marker) as a function of the high voltage for a threshold of 35 DAC steps (top), and as a function of the VFAT threshold for HV = −4.1 kV (bottom) for different GEM planes (HG8, HG2, HG15). 1 DAC step corresponds to about 600 electrons. In all cases, the signal sampling time window in the VFAT was 2 clock cycles wide.
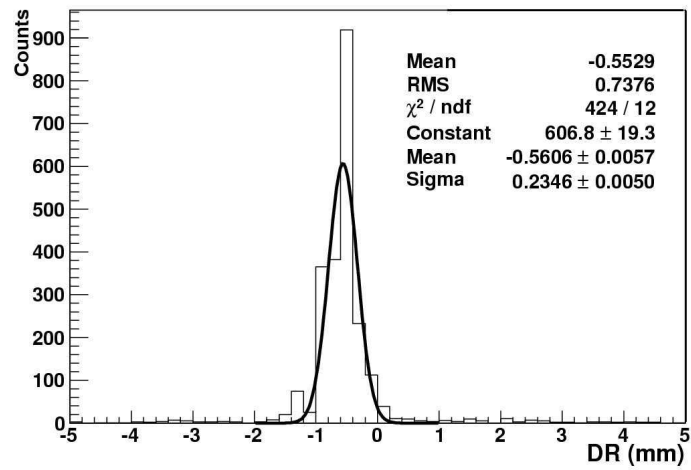
Figure 5.29: Radial distance of strip cluster centres belonging to aligned hits in two different T2 planes.

Chapter 6

Physics performance

6.1 Principle of proton reconstruction

Protons emerging from elastic and diffractive scattering at LHC are emitted at very small angles (10 to $150\,\mu$rad) and undergo no or small ($10^{-7} \div 0.1$) fractional momentum loss ($\xi = |\Delta p|/p$), respectively. Hence they are very close to the beam and can only be detected in the RP detectors downstream symmetrically on either side of the interaction point (IP) if their displacement at the detector location is large enough.

The transverse displacement $(x(s), y(s))$ of an elastically or diffractively scattered proton at a distance s from the IP is related to its origin $(x^*, y^*, 0)$, scattering angles $\Theta^*_{x,y}$ and ξ value at the IP via the optical functions L, v, D as described in chapter 3. The optical functions (L, v, D) determining the explicit path of the particle through the magnetic elements, depend mainly on the position along the beam line (i.e. on all the magnetic elements traversed before reaching that position and their settings which is optics dependent) but also on the particle parameters at the IP (3.2).

The proton tracking through the accelerator lattice is based on the parametrization of the optical functions (extracted for each configuration from the program MAD-X [47]); their slight dependency on the kinematic variables, $\Theta^*_{x,y}$ and ξ, is also taken into account [48].

The transverse vertex position and the scattering angle at the IP are smeared assuming Gaussian distributions with widths given by the transverse beam size and the beam divergence, both determined by β^* and by the (normalised) emittance ε_n. Table 6.1 summarises the beam parameters at the IP for the different optics settings. In addition an energy spread of 10^{-4} is always assumed. The minimum distance of a RP station to the beam on one hand and constraints imposed by the beam pipe or beam screen size [49] on the other hand will determine the proton acceptance of a RP station. The minimum distance of a RP to the beam is proportional to the beam size $((10-15) \times \sigma_{x(y)}(s))$.

6.1.1 Acceptance

The acceptance of the RP system for elastically or diffractively scattered protons depends on the optics configuration. The complementarity of the acceptance of different optics configurations is shown in figure 6.1. As discussed in chapter 3, the TOTEM-specific optics with $\beta^* = 1540$ m was

Table 6.1: Parameters of the different optics settings at nominal emittance ε_n=3.75 μm·rad ($\varepsilon_n = 1\,\mu$m·rad for β^*=1540 m).

β^* [m]	crossing angle [μrad]	IP offset in x [μm]	IP beam size [μm]	IP beam divergence [μrad]
1540	0	0	450	0.3
90	0	0	213	2.3
2	92	322	32	16
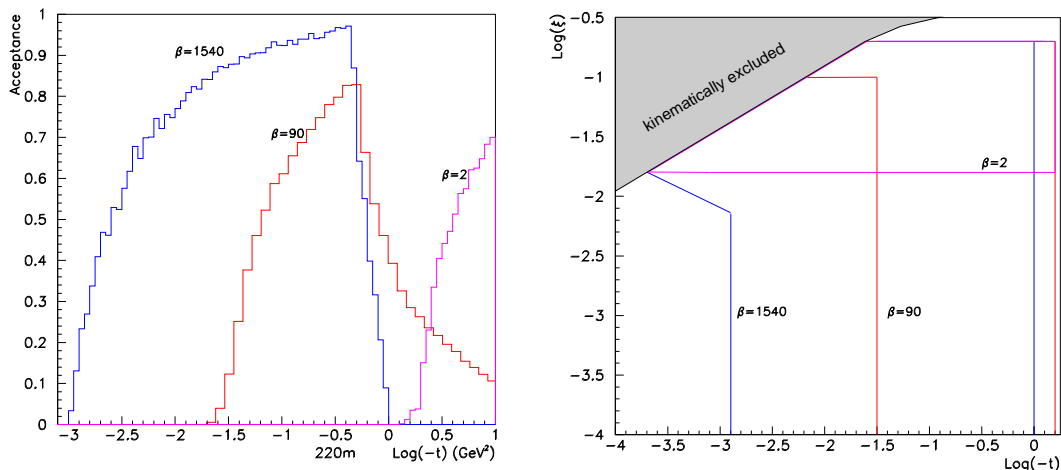
Figure 6.1: Left: acceptance in $\log_{10}|t|$ for elastically scattered protons at the Roman Pot station at 220 m for different optics settings. Right: acceptance in $\log_{10}|t|$ and $\log_{10}\xi$ for diffractively scattered protons at the same RP station for different optics settings. The contour lines represent the 10% level.

particularly optimised for accepting protons down to very low $|t|$-values and — in the diffractive case — with all kinematically allowed values of ξ (blue graphs in figure 6.1, left and right, respectively). With the $\beta^* = 90$ m optics, diffractive scattered protons are still accepted independently from their ξ-value, but the t-acceptance is reduced compared to $\beta^* = 1540$ m optics (red graphs in figure 6.1, right and left, respectively). With high luminosity optics ($\beta^* = 0.5$ m $\div$ 2 m) on the other hand, the diffractive protons are within the acceptance of the RP detectors because of their ξ value almost independently of their t value (magenta graph in figure 6.1, right). In addition, elastically scattered protons can be detected at very large t (see magenta graph in figure 6.1, left).

The complementarity of the different optics configurations in the measurement of elastic and central diffraction cross-section is shown in figure 6.2. In elastic events (figure 6.2, left), the full t-range from 0.002 up to 10 GeV^2 will be covered by combining data from runs at several optics configurations. With typical running times of 10^5 s (i.e. a bit more than a day), enough statistics can be accumulated for each interval (see table 6.2). The statistics is also sufficient for the physics alignment of the RP detectors. The overlapping regions between the acceptances of the different optics configurations will allow for cross-checks of the measurements.
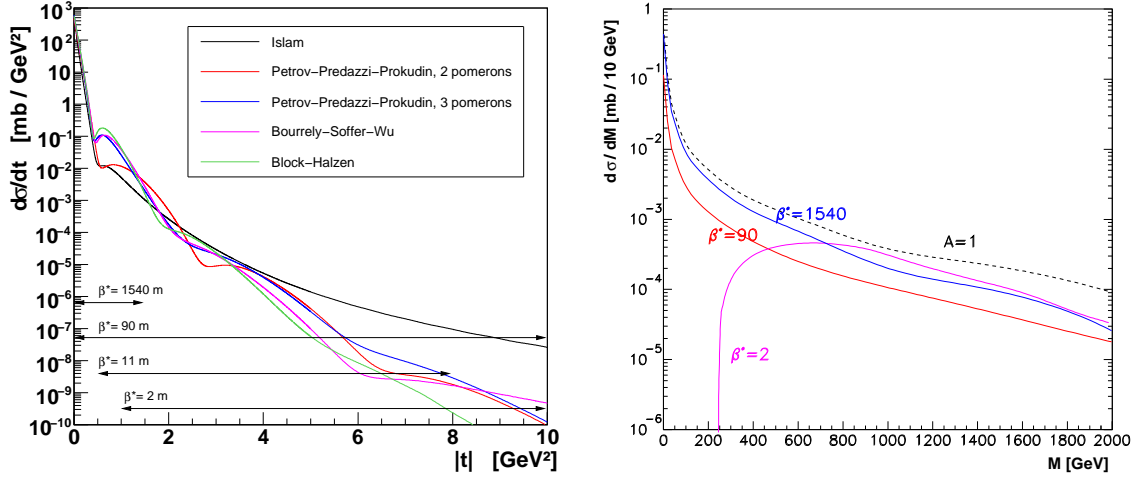
Figure 6.2: Left: differential cross-section of elastic scattering at $\sqrt{s} = 14\,\text{TeV}$ as predicted by various models together with the t-acceptance ranges of different optics settings. Right: predicted differential cross-section of central diffraction at $\sqrt{s} = 14\,\text{TeV}$ with (solid) and without (dashed) taking the proton acceptance into account for different optics settings.

Figure 6.2 (right) shows the predicted central diffractive mass distribution together with the acceptance corrected distributions for three different optics settings. With the high and intermediate β^* optics, all diffractive masses, down to the lowest values are observable. For low-β^* optics on the other hand, the acceptance starts at around 250 GeV but has the advantage of better statistics for high masses due to the higher luminosity. By combining data from runs at low-β^* optics with data from high or intermediate optics runs, the differential cross-section as function of the central diffractive mass can be measured with good precision over the full mass range.

6.1.2 Reconstruction of diffractive proton kinematics

The reconstruction procedure for diffractively scattered protons aims at a determination of the kinematics parameters $\Theta_{x,y}$ and ξ of the proton. For elastic scattering, i.e. when $\xi = 0$, the reconstruction is simpler and will be discussed more in detail in section 6.1.3. In the following, the reconstruction procedure and its performance for diffractive protons with the $\beta^* = 90\,\text{m}$ optics will be discussed in detail. The reconstruction performance for other optics will only be briefly summarised.

6.1.2.1 Diffractive proton reconstruction with the $\beta^* = 90\,\text{m}$ optics

The transverse coordinates of the proton at the IP $(x^*, y^*$, see eq. (3.2)) are considered as additional free variables since their uncertainty contribute significantly to the reconstruction uncertainty, especially for the high β^* optics characterised by large beam sizes at the IP. To reconstruct the full set of kinematic variables, $(\Theta_x, \Theta_y, x^*, y^*, \xi)$, the proton transport equations (3.2) are inverted by χ^2 minimisation procedure [48, 50].

Table 6.2: Expected number of collected elastic scattering events in different t-intervals for the BSW model in runs lasting 10^5 s (i.e. slightly more than a day) with different optics settings.

| $|t|$-range [GeV^2]	β^* [m]	typical $\mathcal{L}$ [cm^{-2}s^{-1}]	Events / 10^5 s	
$0.0012 \div 0.03$	1540	10^{28}	1×10^7	or $20 \times 10^3/10^{-3}$ GeV^2
$0.03 \div 0.5$	1540	10^{28}	1.4×10^7	or $28 \times 10^3/10^{-3}$ GeV^2
	90	10^{30}	7.5×10^8	or $1.5 \times 10^6/10^{-3}$ GeV^2
$0.5 \div 2$	90	10^{30}	5×10^5	or $300/10^{-3}$ GeV^2
	11	10^{32}	8×10^7	or $48 \times 10^3/10^{-3}$ GeV^2
	2	10^{33}	1×10^7	or $6 \times 10^3/10^{-3}$ GeV^2
$2 \div 3$	90	10^{30}	1.4×10^3	or $1.4/10^{-3}$ GeV^2
	11	10^{32}	1.4×10^5	or $140/10^{-3}$ GeV^2
	2	10^{33}	1.1×10^6	or $1100/10^{-3}$ GeV^2
$3 \div 6$	90	10^{30}	170	or $56/$GeV^2
	11	10^{32}	17×10^3	or $5600/$GeV^2
	2	10^{33}	430×10^3	or $143 \times 10^3/$GeV^2
$6 \div 10$	2	10^{33}	500	or $125/$GeV^2

The resolution in ξ of diffractively scattered protons using only information from the RP station at 220 m is shown in figure 6.3 (left). The ξ-resolution is about 6×10^{-3}, except for large $|t|$ (> 1 GeV^2), where it worsens, and large ξ (> 0.01) where it improves. If the scattering vertex can be determined to a precision of 30 μm with the central CMS detector during common data taking, the ξ-resolution improves to about 1.6×10^{-3} [2]. The corresponding t-resolution is almost independent of ξ and ranges from 3×10^{-3} GeV^2 at $t = -1 \times 10^{-2}$ GeV^2 to 1 GeV^2 at $t = -10$ GeV^2 [48]. The ξ and the t determination will e.g. be used for measuring the diffractive mass ($\approx \sqrt{s\xi}$) and t distribution for single diffractive events.

Further studies showed that including the information from a RP station at 147 m improves the performance only slightly and only for large $|t|$ due to large contributions to the uncertainty from multiple scattering in the detectors and window material of the RP station at 147 m.

In the case of central diffraction, the two protons originate from a common scattering vertex position which slightly improves the reconstruction resolution. The resolution in the diffractive mass, reconstructed purely from the proton information according to

$$M^2 = \xi_1 \xi_2 s, \qquad (6.1)$$

where $\sqrt{s} = 14$ TeV, is shown in figure 6.3 (right). The mass resolution ranges from 40 GeV for symmetric events, i.e. those with $\xi_1 \approx \xi_2$, to 180 GeV for the very asymmetric events, where one of the ξ values is three orders of magnitude larger than the ξ value of the other. If the scattering vertex can be determined to a precision of 30 μm with the central CMS detector during common running, the mass resolution improves by approximatively a factor three [2].
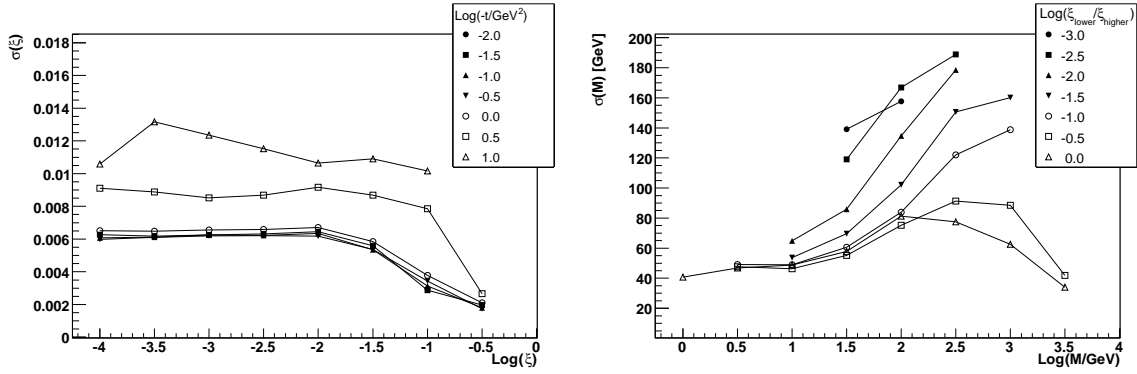
Figure 6.3: Left: resolution for the ξ reconstruction of a single diffractive proton based only on the information from the RP station at 220 m at $\beta^* = 90$ m optics. The different markers corresponds to the resolution at different $\log_{10}(-t)$ values. Right: resolution on the reconstruction of the central mass based on the measurement of the two scattered protons in central diffractive events for $\beta^* = 90$ m optics. Both protons are reconstructed with the RP stations at 220 m. The different markers corresponds to different values of the $\xi_{\mathrm{lower}}/\xi_{\mathrm{higher}}$ ratio, where ξ_{lower} (ξ_{higher}) is the ξ-value of the proton that lost less (more) momentum.

#### 6.1.2.2 Diffractive proton reconstruction performance with other optics

At low β optics only protons with a ξ above 0.02 are detected with a RP station at 220 m. The ξ resolution ranges from 1×10^{-3} at $\xi = 0.02$ to 2×10^{-3} at $\xi = 0.2$ with only a small t dependence. If both protons are detected at the 220 m location, the accepted mass of the central system in central diffractive events is larger than 250 GeV and the mass resolution ranges from 5 GeV for a central mass of 250 GeV to 20 GeV for a central mass of 2.5 TeV. All accepted events are more or less symmetric, i.e. $\xi_1 \approx \xi_2$, due to the limited ξ acceptance. For further details see ref. [2].

With $\beta^* = 1540$ m optics, protons are detected independently of their ξ but the large beam size at the IP and large L_x value complicates the disentangling of the x^*, Θ_x^* and ξ contributions to the horizontal displacement of the proton at the RP station. To constrain the parameters, information from both the RP station at 147 and 220 m are used for the reconstruction. The ξ resolution of this method ranges between 5 to 10×10^{-3} with dependencies on the azimuthal angle and the size of t. The accepted mass of the central system in central diffractive events spans the whole mass range for this optics. The resolution on the central mass ranges in the best case, for symmetric events, from 50 GeV for a mass of 50 GeV, to 80 GeV for a mass of 2 TeV. A more detailed description of the reconstruction method and the performance can be found in ref. [2, 50].

6.1.3 Reconstruction of elastic protons

Here the algorithm for the reconstruction of elastic events is briefly described. The detailed description can be found in ref. [51]. The algorithm consists in the following three steps:

- Selection of elastic proton candidates: RP detector hits belonging to the particle tracks of elastic protons (in both arms) are selected.
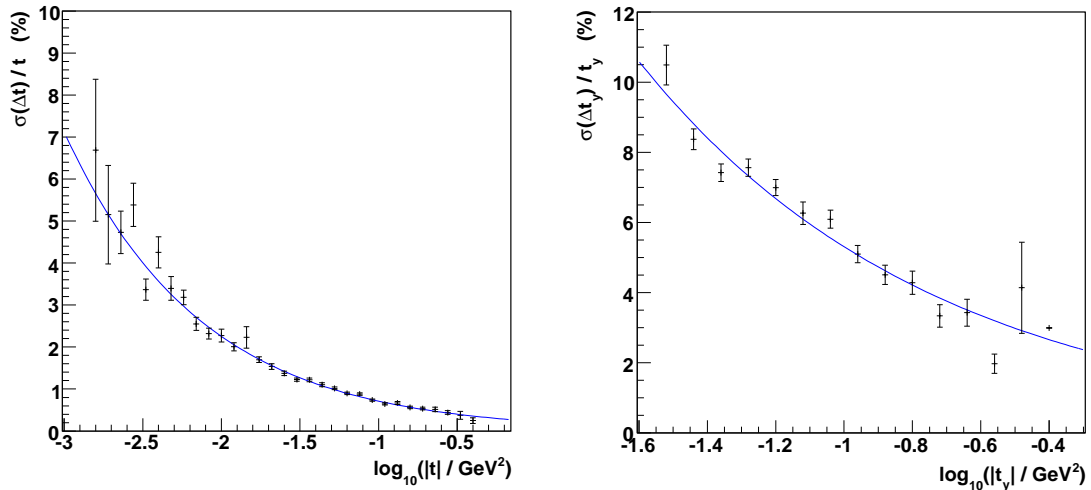
Figure 6.4: Relative resolution on t (left) and t_y (right) from the elastic event reconstruction based on the RP stations at 220 m with $\beta^* = 1540$ m and $\beta^* = 90$ m optics respectively. The solid line in the left (right) plot shows the expected $1/\sqrt{|t|}$ ($1/\sqrt{|t_y|}$) dependence.

- Fitting of the proton kinematics. Three fits made: one for the right arm fit, one for the left arm and a global one. The fits are made using a linear model approach based on the proton transport equations (3.2).

- Final selection. Fits for the left and right arm are compared. The differences in the reconstructed scattering angles Θ_x^*, Θ_y^* and vertex positions x^*, y^* are required to be within the expected uncertainties. For events passing all selections, the global fit is taken as the result.

With $\beta^* = 1540$ m, both effective lengths, L_x and L_y, are large and both magnifications, v_x and v_y, small at the RP station of 220 m enabling the measurement of both projections of the scattering angle and hence the unambiguous reconstruction of $t = t_x + t_y$, where $t_x \equiv t \cos^2 \varphi \approx (p \Theta_x^*)^2$ and $t_y \equiv t \sin^2 \varphi \approx (p \Theta_y^*)^2$. The relative precision of the t measurement with $\beta^* = 1540$ m optics is shown in figure 6.4 (left) and follows the expected $1/\sqrt{|t|}$ dependence.

With $\beta^* = 90$ m on the other hand, $L_x(220 \text{ m})$ at the RP station at 220 m is zero. Hence in this station only the y-component of the scattering angle is measured and only the t_y component reconstructed. The relative precision of the t measurement with $\beta^* = 90$ m optics is shown in figure 6.4 (right) and follows the expected $1/\sqrt{|t_y|}$ dependence.

6.2 Measurement of inelastic events

6.2.1 Track and vertex reconstruction

T1 and T2 have been designed with the goal of detecting primary particles to reconstruct the primary vertex with a precision sufficient to discriminate beam-beam events from the background (mainly beam-gas events and halo muons). Due to the very low angle with respect to the beam of
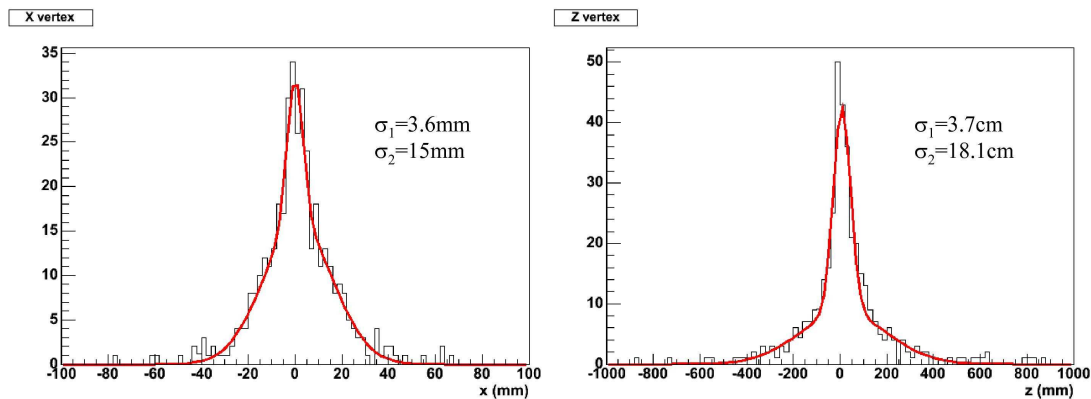
Figure 6.5: Simulated vertex reconstruction capability for T1 in the transverse plane (left) and longitudinally (right).

the charged tracks detected in the telescopes, a good spatial resolution is needed: T1 provides an average single hit resolution of ~ 0.8 mm while T2 provides a radial resolution of $\sim 100\,\mu$m. Simulations show that in presence of the CMS magnetic field, the primary vertex can be reconstructed with a precision of ~ 1.5 cm in the radial direction and ~ 20 cm in the beam direction (figure 6.5). Resolutions one order of magnitude better can be achieved running with the CMS magnetic field switched off.

The main background in the cross-section measurement comes from beam-gas events, which can be largely rejected with the obtained accuracy on the primary vertex reconstruction. Simulation studies show that only $\sim 3\%$ of the beam-gas events are misidentified as beam-beam, corresponding to a rate below 1 Hz ([1], p. 191) for a running scenario with $k = 156$ bunches à 1.15×10^{11} protons.

6.2.2 Trigger acceptance

The L1 trigger in T1 is generated combining the digital signals coming from different groups of anode wires, to maximise the signal generation speed, while in T2 the L1 trigger is generated combining the signals coming from arrays of pads from different planes. An efficient trigger is a key point in avoiding biases in the measurement of the total or diffractive cross-section. With a double-arm trigger more than 99% of non-diffractive events can be detected, while with a single arm trigger one can detect the events escaping the double-arm trigger and most of the diffractive interactions that have all visible tracks in only one arm.

Dedicated studies show that single and double diffractive events are responsible for the major loss in the inelastic rate; with a single-arm trigger, a fraction of these events, corresponding to ~ 2.8 mb, escapes detection. The lost events are mainly those with a very low mass (below ~ 10 GeV/c^2), since all their particles are produced at pseudo-rapidities beyond the T2 acceptance and escape therefore the detection. To obtain the total inelastic rate, the fraction of events lost be-
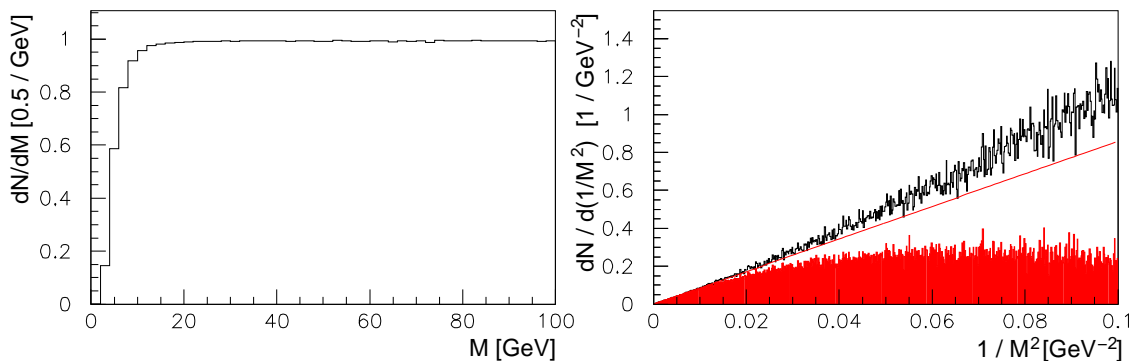
Figure 6.6: Left: ratio of detected Single Diffractive events as a function of the diffractive mass, M. Right: simulation (unshaded) and acceptance corrected (shaded) Single Diffractive distribution as function of $1/M^2$. The line shows a linear fit based on the acceptance corrected events in the mass region above $10\,\mathrm{GeV}/c^2$.

cause of the incomplete angular coverage can be estimated by extrapolation. In the case of single diffraction, the reconstructed $1/M^2$ distribution has been linearly fitted for $M > 10\,\mathrm{GeV}/c^2$, and the extrapolation to low masses has then be compared with simulation. For Single Diffraction, the extrapolated number of events differs from the simulation expectations by 4%, corresponding to a 0.6 mb uncertainty on the total cross-section (figure 6.6). The same estimation for the Double Diffraction and Double Pomeron Exchange gives a 0.1 mb and 0.2 mb uncertainty, respectively.

In the study of diffraction, the telescopes can be used to trigger and/or measure rapidity gaps. Best result are expected in combined running of the TOTEM and CMS detectors; nevertheless studies show that using only T1 and T2 telescopes, the rapidity gaps in DPE events can be measured with a precision $\lesssim 1$ unit of rapidity. Moreover, the comparison of results from SD and DPE events open the possibility of estimate the rapidity gap survival probability at LHC energies.

6.3 Total cross-section measurement

The total pp cross-section, σ_{tot}, will be measured first in runs with the $\beta^* = 90\,\mathrm{m}$ optics and later — with better precision — with the $\beta^* = 1540\,\mathrm{m}$ optics (chapter 3). The method based on the Optical Theorem and the quantities to be measured have been explained in section 2.1. The total uncertainty of σ_{tot} has the following contributions.

6.3.1 Inelastic rate

The uncertainty on the inelastic rate is dominated by the inelastic trigger losses $\delta(N_{\mathrm{inel}})/N_{\mathrm{inel}} \approx 1\%$ as discussed in section 6.2.2. The second component — trigger contamination by beam-gas background — is much smaller. This estimate is almost independent from the beam optics, exceptions being SD and DPE where for some trigger strategies leading protons are parts of the signature.
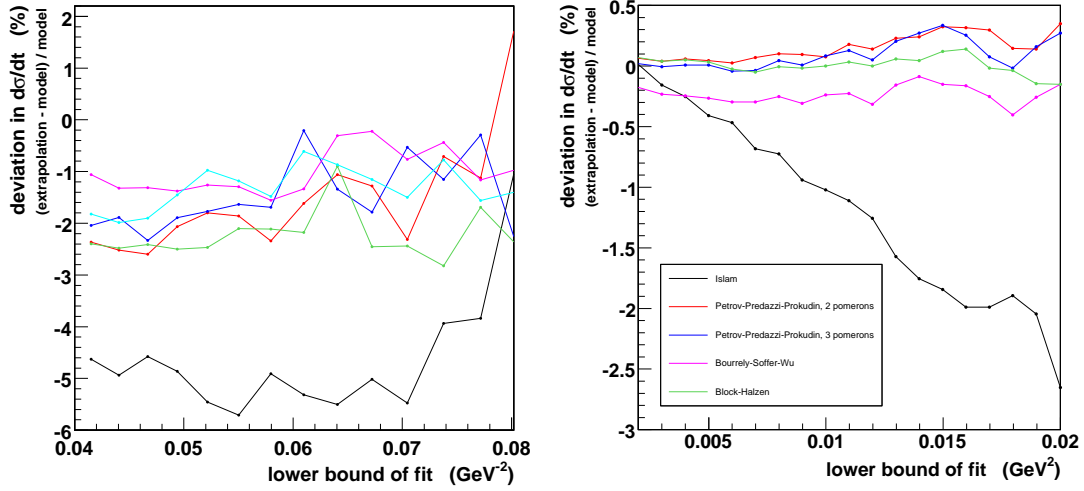
Figure 6.7: Relative deviation of the extrapolation results based on a simulation (not including an error on L_x). Left: $\beta^* = 90$ m, right: $\beta^* = 1540$ m. The t_y- and t-distributions were fitted from the indicated lower bound (abscissa) to $0.25\,\mathrm{GeV}^2$ and $0.04\,\mathrm{GeV}^2$, respectively. The different solid lines corresponds to different models.

6.3.2   Elastic rate and extrapolation of the cross-section to t = 0

The determination of σ_{tot} requires two aspects of elastic scattering to be measured: the total elastic rate and the extrapolation of the differential cross-section $d\sigma/dt$ to the Optical Point $t = 0$. Obviously, to be complete, the measured elastic rate has to be complemented by the extrapolated part, so that this extrapolation enters twice in the procedure.

At $\beta^* = 90$ m, protons with $|t| > 0.03\,\mathrm{GeV}^2$ are observed in the RP detector at 220 m (chapter 3). The starting point of the acceptance lies well above the region where the delicate effects from the interference between nuclear and Coulomb scattering play a role. Hence for the early running optics no such perturbation needs to be included in the extrapolation procedure, in contrast to the extrapolation at the $\beta^* = 1540$ m optics with $|t|_{\min} = 10^{-3}\,\mathrm{GeV}^2$.

As shown in section 2.2 (figure 2.4), most theoretical models [7] predict an almost exponential behaviour of the cross-section up to $|t| \approx 0.25$ GeV^2. For all the models considered — except for the one by Islam et al. — the deviations are small. In the t-range mentioned, the slope $B(t)$ (figure 2.4, right) can be well described by a parabola, which is therefore used for the fitting function and the extrapolation. Since this quadratic behaviour of the slope characterises all the models, the extrapolation method is valid in a model-independent way.

As explained in section 6.1.3, the extrapolation of the elastic cross-section to $t = 0$ will be based on the measurement of the $d\sigma/dt$ ($d\sigma/dt_y$) distribution for the $\beta^* = 1540$ m ($\beta^* = 90$ m) optics. For the $\beta^* = 90$ m optics, the azimuthal symmetry of the elastic scattering process, i.e. the equality of the distributions of t_y and t_x, is used to infer the distribution $d\sigma/dt$ from the $d\sigma/dt_y$ distribution.

The accuracy of the extrapolation to $t = 0$ is shown in figure 6.7. The key contributions are the following:

- Smearing effects of the t-measurement: For $\beta^* = 90$, they are dominated by the beam divergence ($\sigma(\theta_{\text{beam}}) = 2.3\,\mu$rad) and lead to a shift of -2% in the extrapolation result (figure 6.7 left). For $\beta^* = 1540\,$m with $\sigma(\theta_{\text{beam}}) = 0.29\,\mu$rad, this contribution is less than 0.1% (figure 6.7 right).

- The statistical error of the extrapolation with the $\beta^* = 90\,$m optics for an integrated luminosity of $2\,\text{nb}^{-1}$, i.e. about 5 hours running at a luminosity of $10^{29}\,\text{cm}^{-2}\,\text{s}^{-1}$, ranges between 0.6% and 4% depending on the fit interval for the extrapolation. For the $\beta^* = 1540\,$m optics, this contribution is less than 0.1% for an integrated luminosity of of $0.36\,\text{nb}^{-1}$, i.e. about 10 hours of running at a luminosity of $10^{28}\,\text{cm}^{-2}\,\text{s}^{-1}$.

- Systematic uncertainty of the t-measurement: the dominant contribution comes from the uncertainty of the effective length L_x. The currently expected precision of 2% would translate into an offset of the extrapolation of about 4%. Detector alignment and beam position accuracy are much more crucial for the $\beta^* = 1540\,$m optics with its small beam size (the vertical beam size $\sigma_{y_{\text{beam}}} = 80\,\mu$m at the 220 m RP station) than for $\beta^* = 90\,$m, where $\sigma_{y_{\text{beam}}} = 625\,\mu$m at the 220 m RP station.

- Model-dependent deviations of the nuclear elastic pp cross-section from an exponential shape lead to a bias in the extrapolation. Besides the Islam et al. model [7], which can be excluded or confirmed by the measured t-distribution at large $|t|$-values, the models are within $\pm 1\%$ ($\beta^* = 90\,$m) or $\pm 0.2\%$ ($\beta^* = 1540\,$m).

6.3.3 The ρ parameter

The ρ parameter, estimated to be about 0.14 by extrapolating measurements at lower energies [5], enters σ_{tot} in the factor $1/(1 + \rho^2) \sim 0.98$, and hence gives only a relative contribution of about 2%. Assuming a relative uncertainty of at most 33% on ρ, determined by the error of the measurements at TEVATRON [4] and the extrapolation to LHC energies, we expect an relative uncertainty contribution of less than $\delta(1 + \rho^2)/(1 + \rho^2) = 1.3\%$.

6.3.4 Combined uncertainty on total cross-section and luminosity

Combining all the above uncertainties by error propagation for the expressions

$$\sigma_{\text{tot}} = \frac{16\pi}{1 + \rho^2} \cdot \frac{dN_{\text{el}}/dt|_{t=0}}{N_{\text{el}} + N_{\text{inel}}} \quad \text{and} \tag{6.2}$$

$$\mathscr{L} = \frac{1 + \rho^2}{16\pi} \cdot \frac{(N_{\text{el}} + N_{\text{inel}})^2}{dN_{\text{el}}/dt|_{t=0}}, \tag{6.3}$$

and taking into account the correlations, yields a relative error of 4% on σ_{tot} and a relative uncertainty of 7% on $\mathscr{L}$ with $\beta^* = 90\,$m. With $\beta^* = 1540\,$m the expected precision is at the 1% level but this requires an improved knowledge of the optical functions and an alignment precision of the RP station better than $50\,\mu$m.

Chapter 7

The TOTEM electronics system

TOTEM has 3 separate and distinct detector technologies used within the three detector systems; RP, T1 and T2. Each detector system has it's own physically separate electronics system however each system is made following one common system architecture. This has the obvious benefits of reducing design effort by using common electronic components, data formats and DAQ software.

The initial requirements for the electronics system are to be able to readout the charge of the three different detectors on one side and offer full compatibility with CMS on the other.

Table 7.1 gives an overview of the three detectors with their main properties and the number of front-end chips (VFAT) needed. The gas detectors generate more signal charge, distributed over several electrodes. The silicon strips generate positive charge, T2 negative, and T1 both polarities (anodes and cathodes). The T1 and T2 detectors have a large occupancy particularly in the regions close to the beam pipe. This is due to inelastic events with a large number of particles interacting in the beam pipe and thus creating particle showers at the detector edges.

The signal properties vary considerably between detectors. However, it was decided at an early stage to design one common front-end ASIC that would be capable to provide the charge readout for all detectors. This front-end ASIC is called VFAT and is key to providing a common data format and common control and readout needs in the electronic system for all 3 detectors.

Table 7.1: Overview of electronics requirements from the different detectors.

|	RP	T1	T2
No. and type of detectors	240 Si strip detectors	60 Cathode Strip Chambers	40 Gas Electron Multipliers
No. of channels	122880	11124 anodes 15936 cathodes	62400 pads 20480 strips
No. of VFATs	960	480	680
Typical input charge	$\sim$4 fC	$\sim$50 fC	$\sim$50 fC
Occupancy	$<$1%	anodes: $<$10% cathodes: $<$20%	pads: $<$5% strips: $<$30%
Radiation Dose	$<$10 Mrad	$<$50 krad	$<$50 Mrad
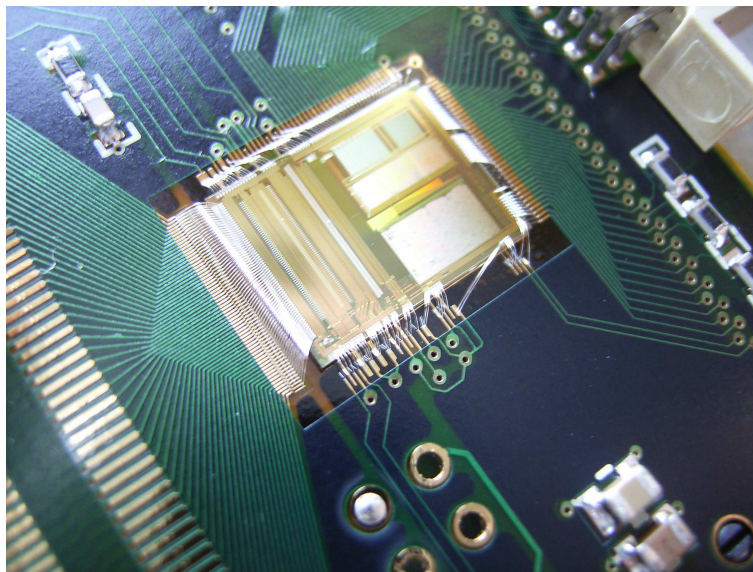
Figure 7.1: Photograph of the VFAT chip.

7.1 VFAT

The VFAT [52] (strictly "VFAT2", being the second version) is a trigger and tracking front-end ASIC, designed specifically for the readout of sensors in the TOTEM experiment at the LHC. The VFAT chip (shown in figure 7.1) has been designed in quarter micron CMOS technology and measures 9.43 mm by 7.58 mm.

It has two main functions; the first (Tracking) is to provide precise spatial hit information for a given triggered event. The second function (Trigger) is to provide programmable "fast OR" information based on the region of the sensor hit. This can be used for the creation of a level-1 trigger.

Figure 7.2 shows the block diagram for the signal path through the VFAT. It has 128 analog input channels each of which are equipped with a very low noise pre-amplifier and a 22 ns shaping stage plus comparator. A calibration unit allows delivery of controlled test pulses to any channel for calibration purposes. Signal discrimination on a programmable threshold provides binary hit information which passes through a synchronisation and monostable stage before being stored within SRAMs until a trigger is received. The monostable has a variable length from 1 to 8 clock periods. This has the effect of recording the hit in more than one clock period (useful for gas detectors which have an uncertainty on the signal charge rise time). The SRAM storage capacity enables trigger latencies of up to 6.4 μs and the simultaneous storage of data for up to 128 triggered events. Dead time free operation with up to 100 kHz Poisson distributed trigger rates is ensured. Time and event tags are added to the triggered data which are then formatted and read from the chip in the form of digitized data packets at 40 Mbps. The data packet format is defined as in figure 7.3.

VFAT has many programmable functions controlled through an I^{2}C interface. These include: internal biasing of analog blocks via 8 bit DACs, individual channel calibration via an internal test pulse with 8 bit programmable amplitude, calibration test pulse phase control, operate with positive
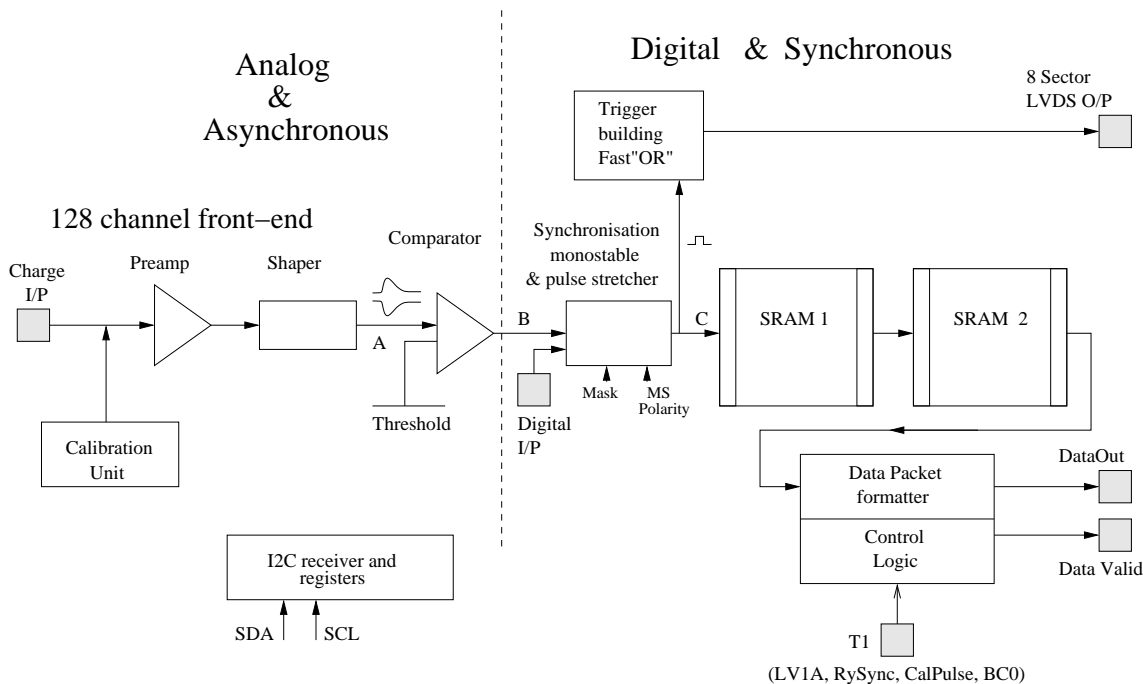
Figure 7.2: Block diagram of the signal path through the VFAT.
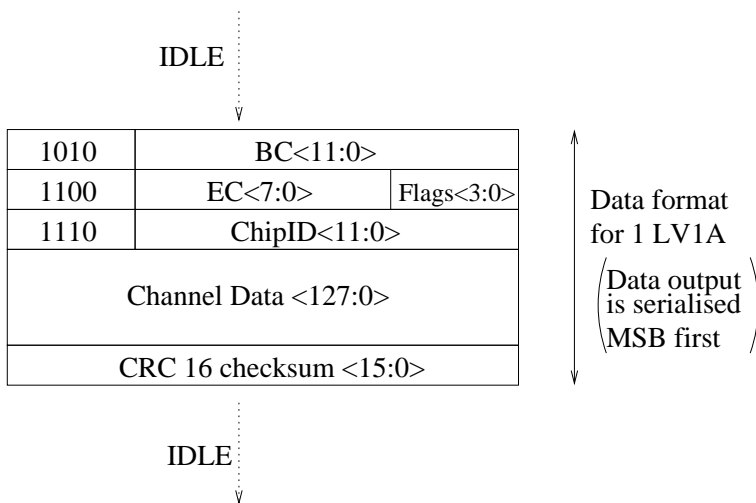
Figure 7.3: VFAT data packet format.

or negative detector charge, 8 bit global threshold plus a 5 bit trim DAC threshold adjust on each channel, multiple possibilities for channel grouping for the "Fast OR" outputs, variable latency, various test modes plus an automatic self test of the digital memories. Chip status information including occupancy and SEU rates can be read via I^{2}C.

Fast synchronous commands are applied via an encoded LVDS signal (T1) which is then decoded to 4 synchronous commands via an internal command decoder.
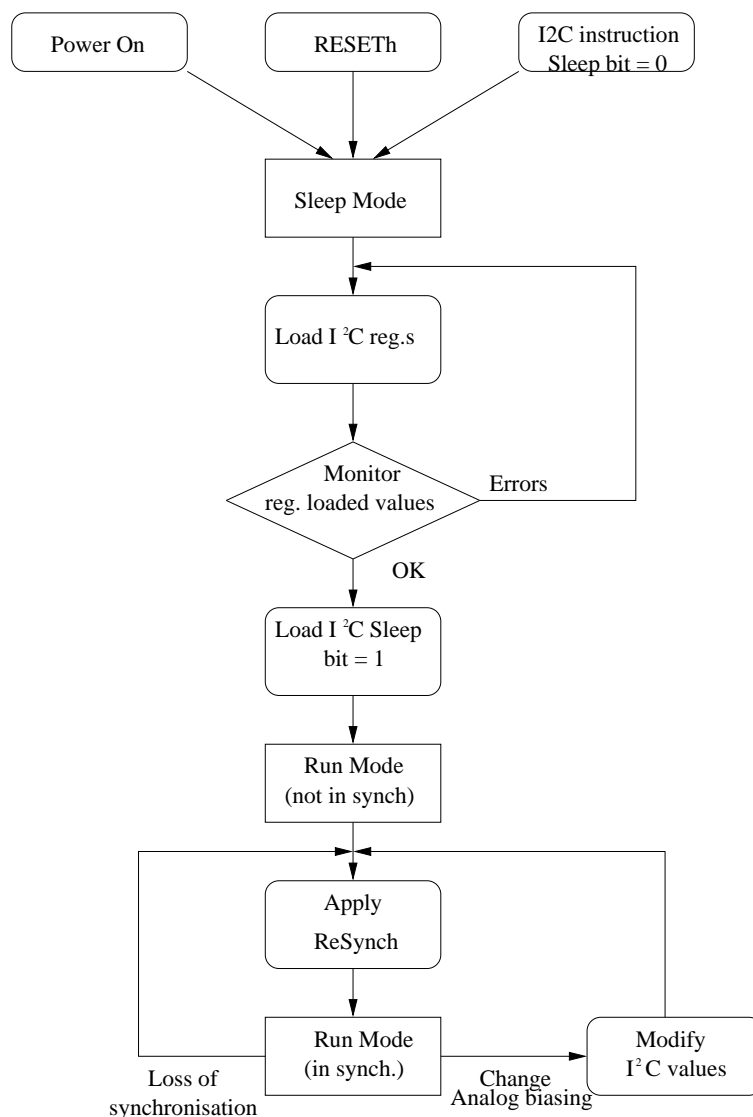
Figure 7.4: Flowchart of the operation cycle of VFAT.

For robustness against single event upsets (SEU), the digital parts of VFAT have been designed with hamming encoding for the SRAMs and triplication logic for the I^{2}C interface and control logic. All analog circuitry employs layout techniques that reduce threshold voltage shifts under ionising radiation.

The operation flow of VFAT is shown in the flowchart of figure 7.4. On applying power to the chip VFAT performs an automatic power-on reset and goes directly into "Sleep Mode". Sleep Mode sets all DACs to default values providing stable but minimum power consuming conditions to the entire chip. In Sleep Mode only the I^{2}C is active and can respond to commands. The internal registers can then be loaded with data. This data can be read back to check if loading was successful. The values loaded are not applied to the active circuits until VFAT is put into Run Mode. When VFAT is put into Run Mode, biases are applied to the analog circuits and digital circuits come out of a reset condition bringing the power consumption up to the normal level. Since
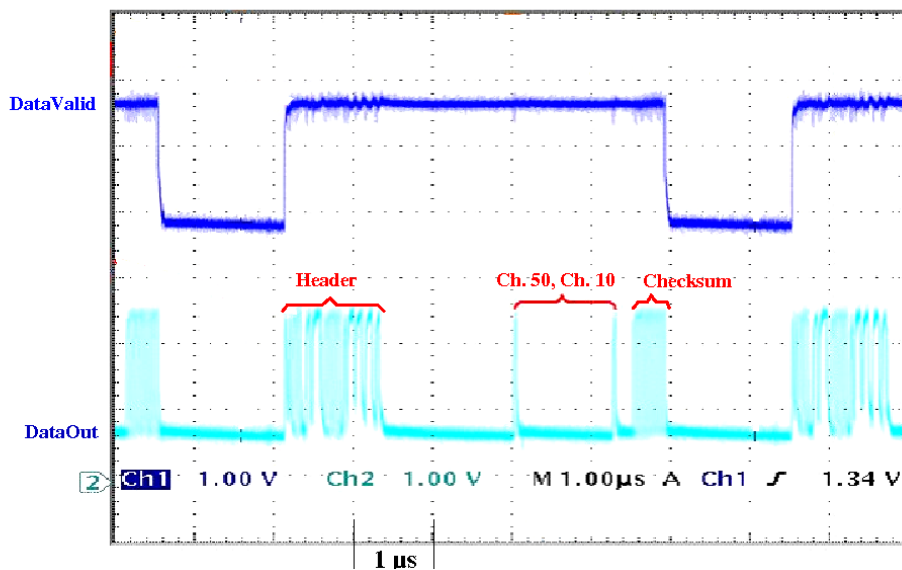
Figure 7.5: Oscilloscope view of the data packet and DataValid signal.

the I^2C is a non-synchronous slow command VFAT still requires a synchronising signal. This is applied via a ReSync signal encoded within the T1 signal. VFAT is now in a synchronous Run mode and ready for taking data. Initial functional measurements showed all functions of VFAT to be fully operational.

Measurements of the Calibration units internal test pulse generator reveal a linear charge delivery range of -2 fC to 18.5 fC with LSB of 0.08 fC.

When triggered, Data packets appear on the DataOut output as shown in figure 7.5 together with a DataValid signal which goes high for the duration of a Data Packet. The figure shows two "hit" channels, these channels received a charge pulse from the Calibration unit.

Noise measurements have been made by choosing a random threshold and then ramping the magnitude of the signal charge using the internal test pulse generator controlled via DAC (digital-to-analog converter). The range is chosen such that the test pulse amplitude VCal passes through the threshold from 0% hits to 100%. The result is an S-curve as shown in figure 7.6. The mean of an error function fit to the S-curve gives the threshold and the sigma gives the noise expressed in ENC (Equivalent Noise Charge).

S-curves have been generated for all channels. The second and third plots of figure 7.6 show histograms of the extracted thresholds and noise of 128 channels. The results show for a mean threshold of 5952 electrons there is a threshold spread (before fine adjustment with the Trim DACs) of 335 electrons rms. The mean ENC is 539 electrons with a spread of 67 electrons rms.

A major design challenge was to integrate the multitude of digital functions without having a significant impact on the analog performance. Stringent design techniques to "deafen the listener" and "silence the talker" have been employed to all analog and digital modules.

Measurements from the chip show all modules to be 100 percent functionally correct. The expected front-end noise performance of approximately 600 e + 50 e/pF of detector capacitance is maintained. The total power consumption is 572 mW.
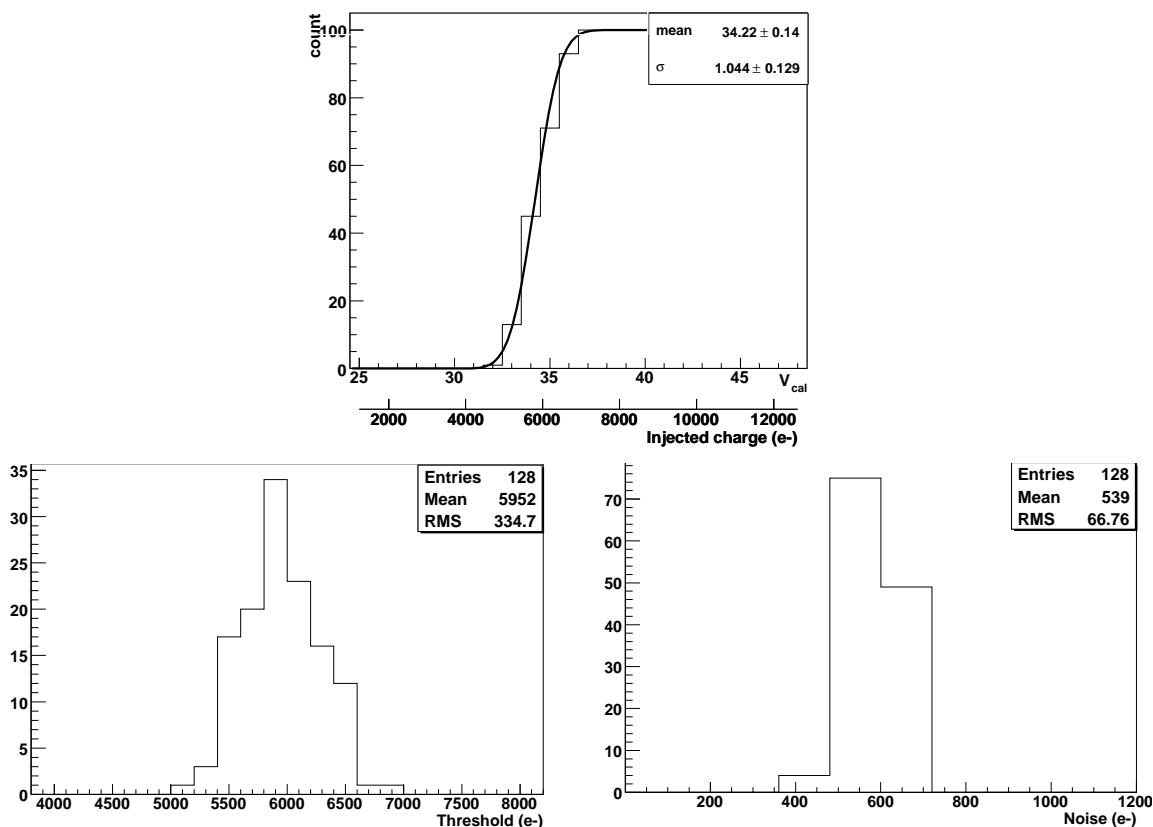
Figure 7.6: Top: S-curve (number of hits as a function of the test pulse amplitude for a fixed threshold) for one VFAT channel with a Gaussian error function fit superimposed. Bottom left: distribution of the mean thresholds (V_{cal} at 50% level of the Gaussian error function) of all 128 VFAT channels. Bottom right: distribution of the noise, i.e. the width of the fitted Gaussian error function, for all 128 channels.

VFAT has successfully integrated complex analog and digital functions into a single ASIC without compromising noise performance.

7.2 The TOTEM electronics control and readout system

The architecture of the TOTEM control and readout system is common to all 3 detector systems. This section describes the common electronics architecture and the components used.

Figure 7.7 shows a basic block diagram of the functional components used in the system. It is sub divided into physically separated regions and also data flow. The "On Detector regions" have the VFAT front-end ASIC located as close to the detector as physically possible. The "Local Detector regions" are for readout boards in the vicinity of the detector used for grouping and distributing control signals.
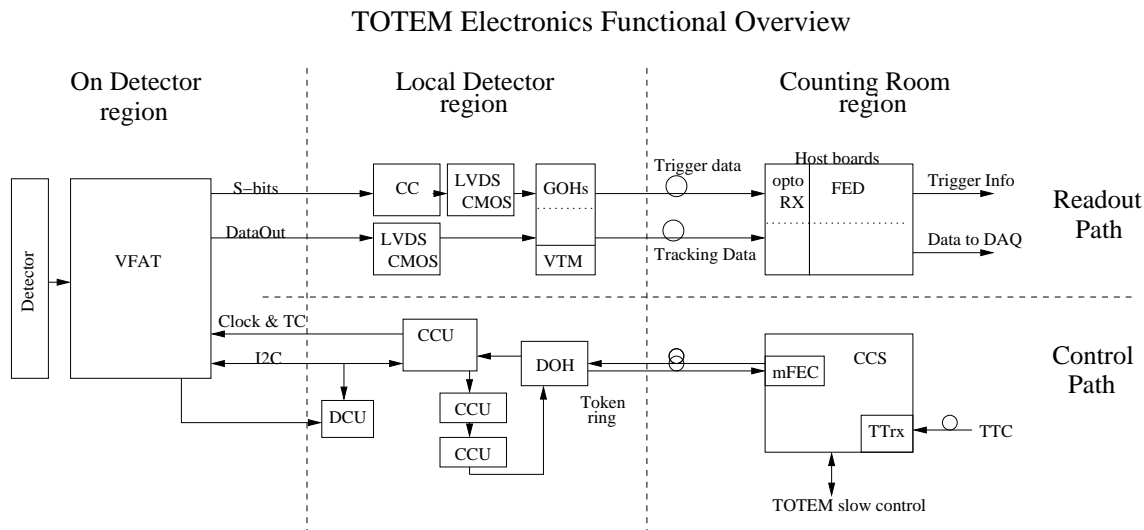
Figure 7.7: Functional block diagram of the TOTEM electronics system architecture.

7.2.1 The VFAT control path

The VFAT control path starts in the counting room with the arrival of Timing, Trigger and Control (TTC) signals [53] to the TTC receiver (TTCrx) on the Clock and Control System (CCS). The TTC signals are composed of the LHC machine clock and trigger commands (TC).

The CCS is equipped with Front End Controller (FEC) modules. TOTEM slow control instructions and TTC signals are transmitted onto a token ring via the FEC modules. The token ring starts with 40 Mb/s optical links from the FECs to the subsystems in the local detector regions. The optical signals of the token ring are converted to electrical signals in the local detector regions by a module known as the Digital Opto Hybrid Module (DOHM [54]). Communication and Control Units (CCU) sit in the token ring and are used to extract and distribute fast clock/TC signals and slow control information to and from the VFATs. The fast clock/TC signals are delivered to the VFATs via Low Voltage Differential Signals (LVDS). Slow control is achieved using the I^{2}C protocol to be able to provide write/read access to registers inside the VFATs. The Detector Control Unit (DCU) contains analog to digital converters (ADCs) which are used to measure currents and voltages within VFAT and read back these values via I^{2}C. The DCU is used during calibration of the VFATs.

The concept of the token ring and the design of the token ring ASICs ie. FEC, CCU, DCU plus associated PLLs [39] were designed by the CERN microelectronics group for use within CMS. The CMS tracker and Preshower use this concept for their control systems.

7.2.2 The VFAT readout path

VFAT produces both trigger and tracking data. These two types of data have very different timing requirements hence are treated separately.

Trigger data is used to aid the generation of the first level trigger hence has to be read out as fast as possible. The Sector outputs (S-bits) of the VFAT give the result of internal fast OR
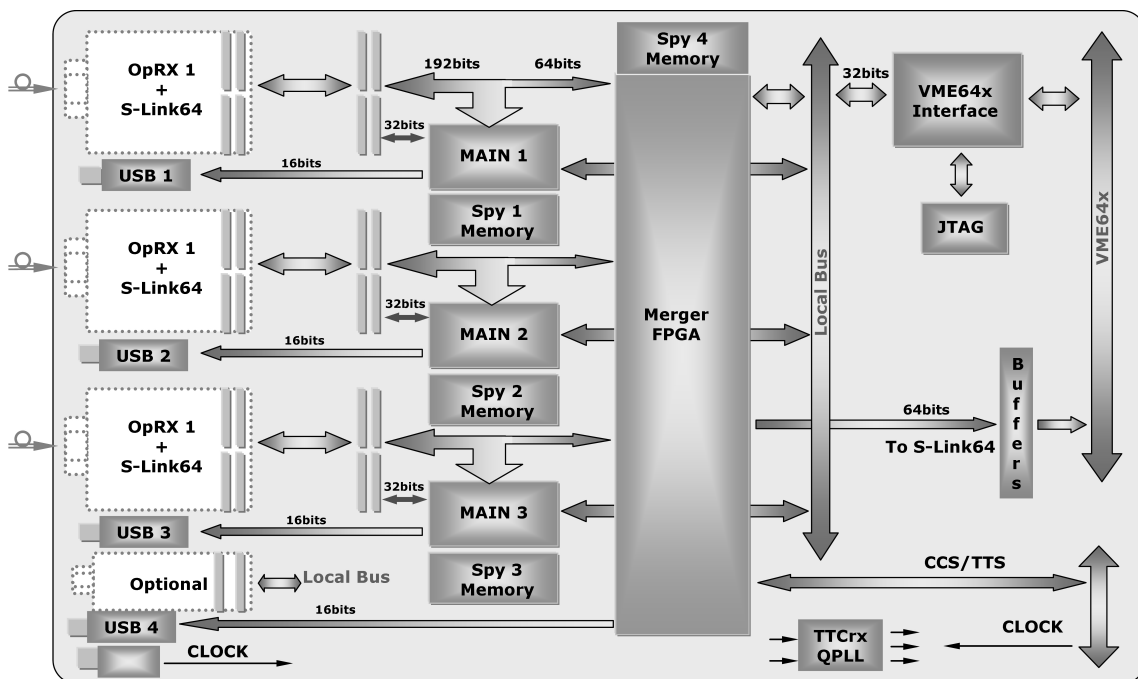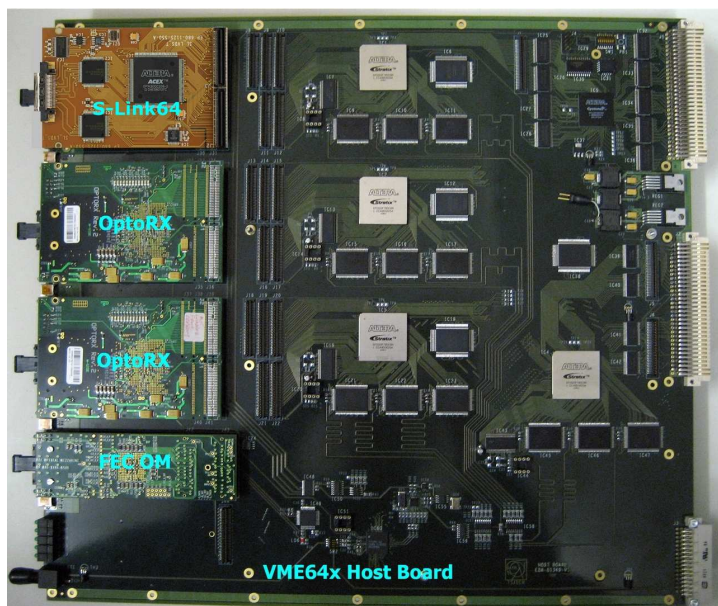
Figure 7.8: Block diagram of the TOTEM FED Host board.

operations within 1 clock cycle. These S-bits are in LVDS format. A Coincidence chip (CC, see section 8.2.1) then performs coincidence operations between VFAT sector outputs. The outputs from the CC chip (still in LVDS format) are then converted to CMOS levels by dedicated LVDS-to-CMOS converters. The trigger data are then serialised and transmitted by optical links at 800 Mb/s to the counting room. The module that performs the serialisation and optical transmission is called the Gigabit Optical Hybrid (GOH [34]).

Tracking data are data corresponding to triggered events and are buffered within VFAT for high trigger rates. Data packets are transmitted in serial LVDS form from the VFAT DataOut outputs at a bit rate of 40 Mb/s. Once again the LVDS to CMOS conversion is performed and the GOH serialises the data for transmission to the counting room via optical links. Up to 16 VFAT DataOut signals are multiplexed by one GOH into a serial stream for optical transmission. All VFATs operate synchronously, a VFAT Trigger Mezzanine (VTM) is used to control the timing of the GOH and maintain synchronisation.

Once in the counting room the optical fibres are connected to the 9U VME64x Host boards (developed by TOTEM) which contain the Front-End Drivers (FEDs [55]) used for trigger and event building. There are separate Host boards for the treatment of trigger data and tracking data. TOTEM uses 6 Host boards for the Trigger system and 8 Host Boards for the tracking data. A block diagram and photograph of the Host Board are shown in figures 7.8 and 7.9 respectively.

The incoming optical fibres (grouped in 3 bundles of 12 fibres) connect to optical receiver modules called optoRx-12. The OptoRx-12 is a plug-in module developed by the CMS preshower. It is based on a 12-channel optical receiver and a Field Programmable Gate Array (FPGA) Stratix™ GX from ALTERA. The FPGA has multiple gigabit blocks, each with four full duplex channels.

Figure 7.9: Photo of the TOTEM FED Host board.

Using clock data recovery technology, these channels can serialise or de-serialise data for transmission rates up to 3.125 Gbps. The module is compatible with the VME mechanical specification [56].

The first stage of FED data management is performed on the optoRX-12 with the de-serialisation of 32 input data streams per FPGA using the embedded high-speed deserialisers.

The second stage of data management is performed on the Host board. There are 3 Altera FPGAs Stratix^{TM} labelled "Main-1", "Main-2" and "Main-3". Each Main controller bridge receives raw data from its associated OptoRX-12 module, stores it into its corresponding memory and transfers it to the VME64x bus or to the USB for slow spy readout.

For certain FED applications the de-serialised data are processed inside the OptoRX-12 module in order to reduce their volume. Then a forth FPGA (also a Stratix^{TM}), labelled "Merger", collects the reduced data through three associated 64-bit buses in order to build the event.

In the Trigger Host boards the incoming trigger data is sent to the FPGAs where coincidence logic functions and more complex algorithms can be performed in order to prepare trigger primitives for the global L1 TOTEM trigger. There are 2 Host Boards per detector used for the trigger.

Since the TOTEM Host boards are also used for data readout, all necessary hardware is available to include the trigger data into the data stream for monitoring purposes.

In the Tracking Host boards the incoming tracking data has a format defined by the data packets of VFAT. The format is defined in figure 7.3.

The data length is organised in 16 bit words consisting of: BC$\langle 11{:}0 \rangle$ (bunch counter), EC$\langle 7{:}0 \rangle$ (event counter), Flags$\langle 3{:}0 \rangle$, Chip ID$\langle 11{:}0 \rangle$, Data$\langle 127{:}0 \rangle$, CRC 16 checksum$\langle 15{:}0 \rangle$ and four control bits for the beginning of the frame. For multiple triggers the frames for each event follow one after another.
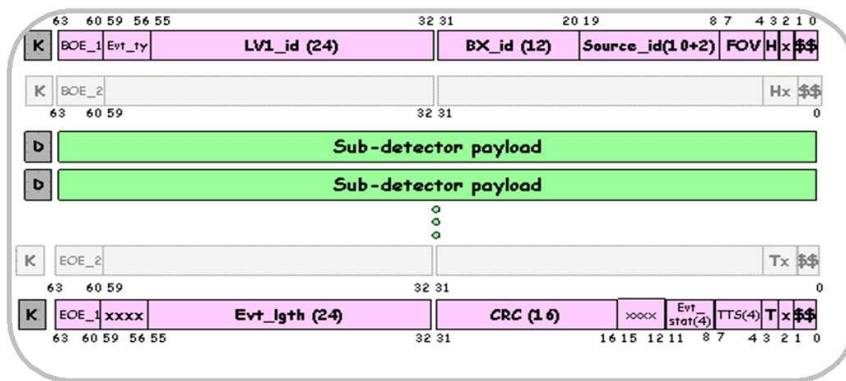
Figure 7.10: CMS FED data format.

When an event fragment is ready to be transmitted to the DAQ, the FED event builder encapsulates the data according to the common CMS FED data format [57] shown in figure 7.10.

The CMS format includes, in addition to the actual sub-detector payload, information such as event type ('Evt_ty'), event number ('LV1_id'), bunch crossing number ('BX_id'), event length ('Evt_lgth'), data source identifier ('Source_id') and CRC information.

There are 3 different possibilities implemented for sending data to the DAQ:

- VME interface: used for TOTEM operation;

- USB interface: alternative for TOTEM operation;

- S-Link64 [58] module: connection to the CMS Front-end Readout Links (FRLs) for common data taking, ensuring full compatibility with the CMS DAQ.

7.2.3 The low and high voltage power supplies

The on-detector electronics are electrically isolated from the counting room through the systematic use of floating power supplies and optical signal transmission or electrical transmission with opto-couplers. The low-voltage power supplies are located as close as possible to the detectors. The high-voltage power supplies are located in the counting-room.

7.3 Specific TOTEM detector electronics

Every effort has been made to standardise the use of components across all three detector systems. However, different geometries and segmentation have inevitably led to different board designs for the "on detector" regions and "local detector" regions.

This section aims to highlight the electronic boards used in the construction of the different detector systems.
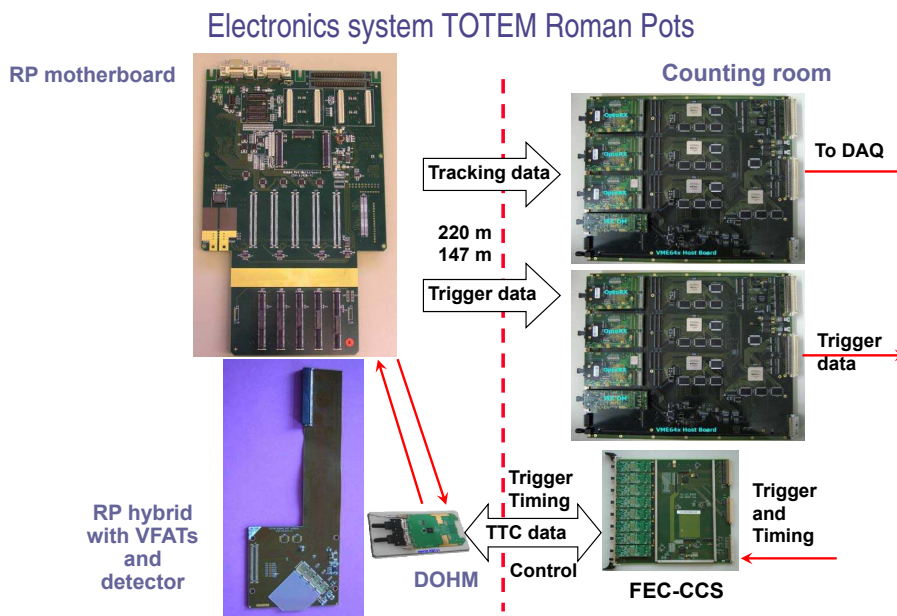
Figure 7.11: Overview of the RP electronics system.

7.3.1 TOTEM electronics boards for the Roman Pots

Figure 7.11 gives an overview of the electronics boards used for the Roman Pot system.

The Roman Pot hybrids contain one silicon detector sub-divided into 512 strips. Four VFATs are bonded directly to each strip with 128 channels per chip. There is one clock and LVDS bus on the hybrid to which each VFAT connects in parallel. In addition the clock is fed to the DCU chip which is also located on the hybrid. A single I^2C bus is delivered to the hybrid which is connected to each VFAT and the DCU.

The RP hybrids (located in the "on detector region") plug directly into the RP mother board (located in the "near detector region"). The RP mother board contains the components necessary for the token ring in the control path and the Trigger and Tracking data transmission components in the readout path. These components were described in section 7.2.

The low voltage power supplies are located approximately 70 m from the pots in the nearest alcove in the tunnel.

7.3.2 TOTEM electronics boards for T1

An overview of the electronic boards used in T1 is shown in figure 7.12.

The VFAT used for the gas detectors is a slightly different version than that used for the Roman Pots. The difference is that the VFAT inputs have internal overload protection circuits that help avoid destructive breakdown of the chip in the case of sparks (uncontrolled charge discharges) from the detector [59]. In all other respects however the VFATs are identical. T1 and T2 use also the same hybrid. This hybrid contains one VFAT chip.
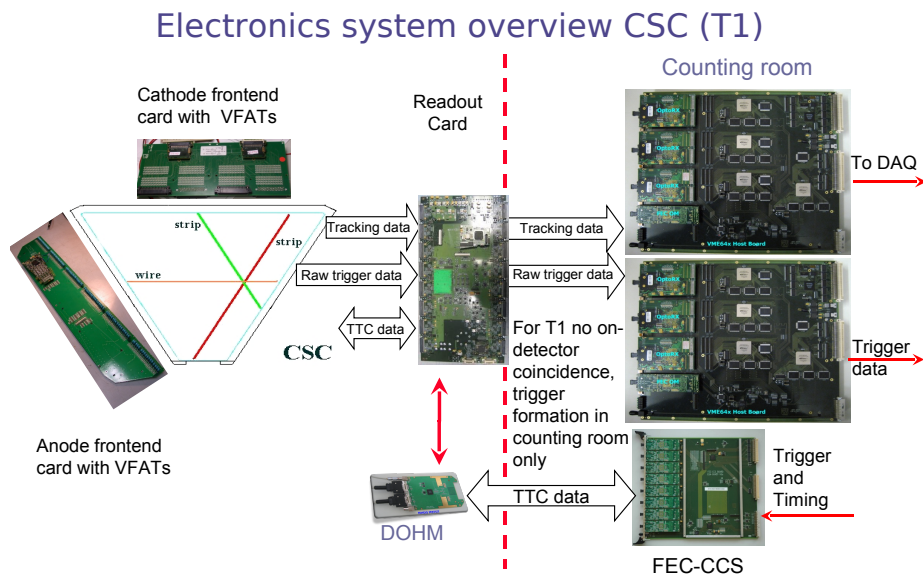
Figure 7.12: Overview of the T1 electronics system.

The connection to the T1 detector is made by plugging the hybrids into one of two readout cards adapted to the geometry of the T1 detector. One for the readout of the anodes (AFEC) and the other for the readout of cathodes (CFEC).

The "on detector region" is connected to the "local detector region" by cables. A T1 Read-Out Card (ROC) contains the components and functions shown in figure 7.7 for the local region with the exception of the CC chip. T1 will instead readout all VFAT S-bits without making any logical operations with respect to other VFATs in the system. One ROC can handle the readout of two cathode strip chambers, and can therefore be connected to up to two AFECs and up to 14 CFECs.

### 7.3.3 TOTEM electronics boards for T2

The electronics boards developed for the T2 system are shown in figure 7.13.

Similar to T1, the T2 detector also uses the VFATs designed for gas detectors which include the input protection circuits. The hybrids are also the same as the ones used for T1. The connection to the detector is made by plugging the hybrids into the horse-shoe card (so called because of its geometrical shape) which in turn is connected to the GEM strips and pads. The VFAT control and readout paths connect by a cable to a board known as the "11th Card". The 11th card receives data from 10 Horse-shoe cards and also contains a CC chip for the coincidence logic function of the trigger path S-bits.

T2 has the most severe ionising radiation environment of the 3 detectors of up to 50 Mrads (see table 7.1). Whilst VFAT and the CC chip are expected to survive these radiation levels the optical links will not. Hence the electronics of the "near detector region" will be placed in a rack near the detectors but behind a radiation shield.
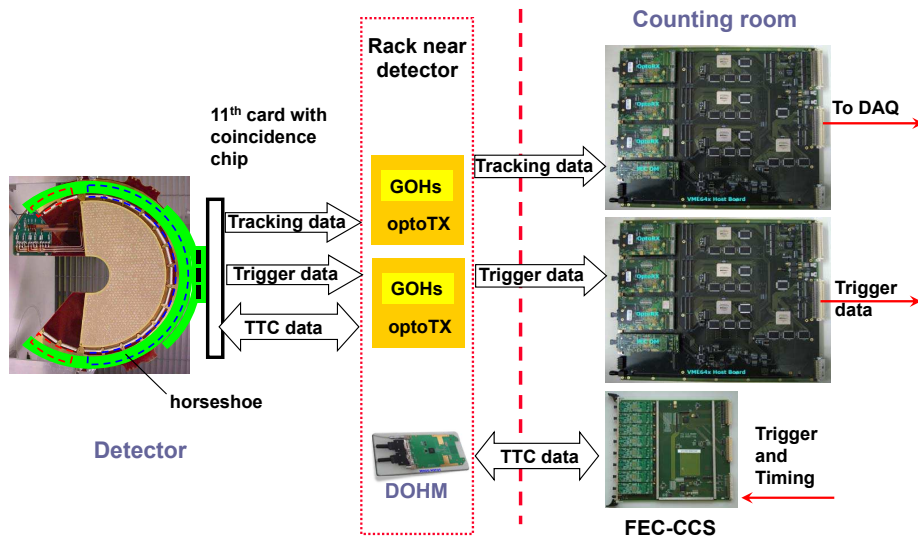
**Figure 7.13**: Overview of the T2 electronics system.

Chapter 8

Trigger

8.1 Strategy

The final triggers are constructed out of all TOTEM detectors and will critically depend on the luminosity, the running and background conditions as well as on the targeted physics. Coincidences between the different detectors on both sides of the intersection point will help to reduce the background but might introduce certain biases. As an example, the total cross-section measurement requires triggers, as unbiased as possible, on all inelastic event topologies. Particularly difficult are triggers on low mass single diffractive events where the very forward particles escape detection, but where the proton on the other side can become visible, e.g. in large β^* runs. Such a single proton trigger will not be background free, mainly due to halo protons and beam-gas collisions. The calibration of all these minimum bias triggers can be foreseen with the help of real bias-free triggers on bunch-crossings. The acceptance for elastically scattered protons is predominantly determined by the β^* (being as large as possible) at the intersection point (figure 6.1). The coincidence between the two protons and their collinearity enable a clean trigger, but overlaps with Double-Pomeron events will occur at larger momentum transfers due to the less steep differential cross-section $d\sigma/dt$ of the latter process. The triggers on Double Pomeron events depend on the machine dispersion and on the optics used. Probably more background will be present in such a trigger. In general, the triggers and backgrounds have to be studied in the various running scenarios and to be understood with the help of Monte-Carlo simulations. How the triggers are performed in the TOTEM sub-detectors with standardised electronics is described below.

It is an essential feature of the three charged particle detectors that they are actively creating the first level trigger. To minimise the development effort, the read-out and trigger strategy is common to all detectors. The trigger bits are generated by the front-end chip (VFAT) itself, which provides 8 fast outputs that are programmable in a limited number of different configurations adapted to the three sub-detectors. These trigger bits are made available within the next clock cycle (25 ns) after the detection of a hit on one of the channels. The trigger is then based either on a crude track reconstruction or on hit activities in the detectors. Coincidences between the chamber planes (for RP and T2) are performed in the "Coincidence Chip" (CC, see also next section), thus reducing the number of trigger bits by an order of magnitude before they are transmitted to the counting-room. Pseudorapidity cuts for the two telescopes, already applicable on the first level
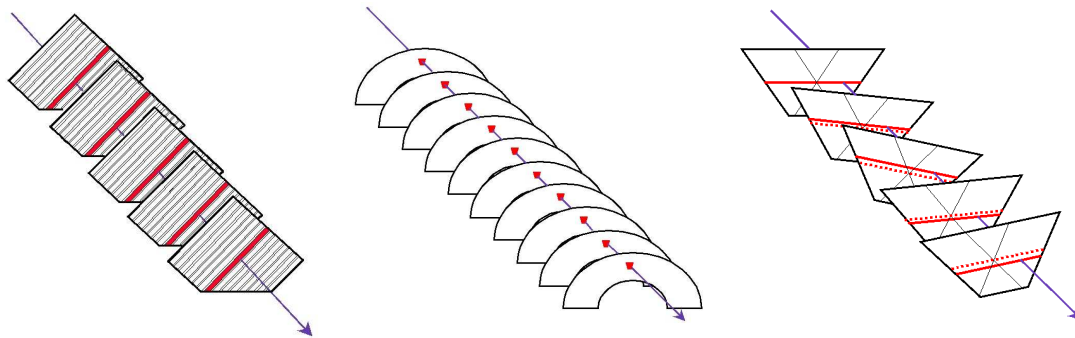
Figure 8.1: Left: RP trigger coincidence in one projection (*u* or *v*). Middle: T2 trigger coincidence in one pad. Right: due to the 3° rotation between different planes in T1 (angle exaggerated in the picture), the coincidence definition is more complicated and hence performed in the counting-room.

trigger, open the possibility to mask noisy regions, as e.g. close to the beam pipe. Cuts on hit multiplicities over larger detector areas might improve the trigger cleanliness or create a simplified trigger.

The trigger formation strategy can be explained with the aid of the principal chamber arrangements in figure 8.1.

The silicon detectors in the Roman Pots close to the beam have to trigger on protons with almost the same momentum as the beam. Consequently there is only one track that is parallel to the beam within less than 1 mrad. Altogether, 10 planes (5 planes per each strip orientation *u* and *v*), define the proton trigger in one Roman Pot station. Each detector plane is divided into 16 groups of 32 strips, defining a track road of about 2 mm per strip orientation. In a first step, the coincidence chip (CC) requires a coincidence of at least 3 out of 5 planes with hits on the same track road resulting in 32 trigger bits per pot (16 in *u* and 16 in *v*). With this loose requirement, tracks crossing the boundary of neighbour track roads are still included. Coincidences between track segments in the *u* and *v* oriented planes will further reduce the trigger rate. In the counting-room, coincidences between the two RP units with a distance of a few meters will select tracks that are parallel to the beam, and multiplicity cuts will reduce the background originating from beam-gas interactions.

For the T2 GEM chambers, the trigger is based on pads that are grouped by a fast-OR logic of 3 × 5 pads into 104 super-pads per half plane. To trigger on a straight track, the super-pads from the 10 detector planes are put into an adjustable coincidence (at least 5 out of 10). This loose coincidence again solves the problem of tracks crossing the superpad boundaries. 104 trigger bits per half arm of the T2 detector are sent to the counting-room for further trigger treatments.

For T1, the trigger is formed by the anodes which are read by two VFATs per plane. However, the more complex detector geometry (for acceptance reasons the chambers are rotated by 3° with respect to each other) makes it difficult to have on-detector coincidences. The 16 trigger outputs of the two VFATs per plane are therefore sent directly to the counting-room where the coincidences between the five planes will be performed in hardware. Simpler triggers based on hit activities in the chambers may lead to a less biased trigger at the expense of larger trigger rates.

This procedure results in 960 trigger bits for T1, 416 for T2 and 768 bits for the RPs.
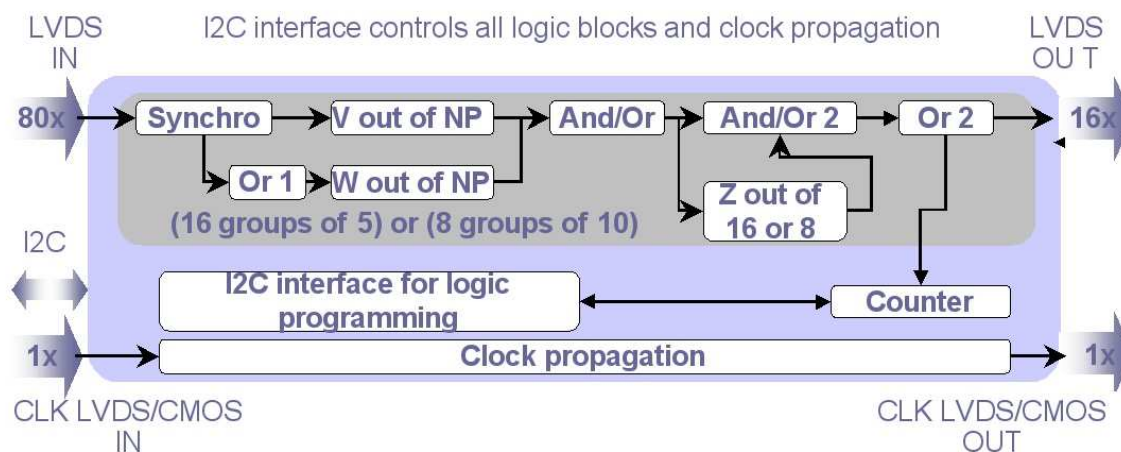
Figure 8.2: Schematic overview of the Coincindence Chip (CC).

8.2 Implementation

8.2.1 The Coincidence Chip (CC)

The Coincidence Chip provides on-detector coincidences to reduce the trigger data sent to the counting room. It is used by the RP and T2 systems, but not by T1 where the more complex geometry made its use too difficult. Figure 8.2 shows a block diagram. The chip has 80 LVDS inputs which can be grouped in two ways:

- 16 groups of 5 inputs, for 5 detector planes (RP case).

- 8 groups of 10 inputs, for 10 detector planes (T2 case).

These groups correspond to detector sectors in a similar transverse position on different detector planes.

A synchronisation block is included to synchronise the pulses to the clock and to stretch the pulses over different clock cycles for detectors with an inherent timing spread larger than a single clock cycle. Asynchronous operation is also possible. For TOTEM only synchronised operation has been adopted.

Two types of coincidences can be performed:

- A coincidence on just one group: V hits on one track road through NP detector planes.

- A coincidence which takes into account a programmable number of neighbouring groups: W hits out of NP detector planes including X neighbouring groups.

The result of these coincidences can be logically combined in a programmable way (AND/OR with possible inversion). The possibility to include neighbouring sectors or not allows a certain programmable selectivity on the direction of incoming particles.

The total number of positive coincidence results is checked (Z out of 8 or 16) and can be logically combined with the coincidence results (AND/OR2). This can be used to impose certain occupancy limits, for instance to prevent the generation of a trigger if a detector is completely filled with artificial hits, e.g. due to noise or particle showers. Finally, signals can be grouped into a smaller number (OR2) to reduce overall signal count.

The parameters of the blocks on the Coincidence Chip can be fully configured through its I²C interface. The VFAT chip also includes counters on the fast trigger outputs to monitor hit rates. This is achieved by a 24 bit counter which records the number of sector hits within a given time window. The duration of the time window can be selected from a list of 4 possible options (6.4 µs, 1.6 ms, 0.4 s, 107 s).

8.2.2 Trigger bit transmission to the counting-room

The trigger signals from all subdetectors are optically transmitted to the counting-room using the GOH optohybrid in the same way as the tracking data. However, the Roman Pot station RP220 is so far away from the counting-room that optically transmitted trigger data would not arrive within the latency allowed by the trigger of CMS. Therefore, in addition to optical transmission for TOTEM runs, electrical transmission with LVDS signals was implemented for commons runs with CMS. To maintain the electrical isolation between detector and counting room, optocouplers will be used to receive these electrically transmitted signals. At regular intervals of about 70 m along the total cable length of 270 m, repeaters based on a custom-designed LVDS repeater chip are inserted to preserve the electrical signal quality.

8.2.3 Trigger signal synchronisation

The large distances between the subdetectors — with RPs at up to 220 m from the interaction point — requires special attention to the synchronisation of the trigger information.

Since the trigger output from the RP220 station has the longest signal transmission time, the trigger signals from that station are the last to arrive in the counting-room. In order to minimise the latency of the combined trigger, the data from the trigger FEDs of the other subdetectors are transmitted via the VME back-plane to the trigger FED of the RP220 station where all the trigger information is merged. Thus the RP220 trigger FED acts as the master of the TOTEM trigger system, generating the global TOTEM L1 trigger decision and is also capable of sending 16 trigger bits to the CMS global trigger system [60] for common data taking with CMS in the future.

The synchronisation of the trigger generating bits is based on the BC0 signal (Beam Crossing Zero). This signal — related to the first bunch of a LHC beam revolution cycle — is issued every 3564 bunch crossings and broadcast by the TTC system. On the detector side, it is received via the control token ring and decoded by a VFAT Trigger Mezzanine (VTM) as shown in figure 7.7. It is then superimposed onto the trigger data stream transmitted to the counting-room. The trigger FEDs also receive the TTC signal including the BC0 signal. The trigger generating bits are then temporally aligned to the BCO signal. This scheme is also used for the 16 trigger bits sent to the CMS global trigger system.

Care also has to be taken in the synchronisation with respect to the transmission of the TOTEM first level trigger signal down to the "Local" and "On Detector" regions.

The level-1 trigger is transmitted to the detectors using the TTC system and the FEC card. The FEC card can adjust the phase of the fast commands and the clock. The latency of the VFAT can be adjusted to account for the differences in delay due to the spatial spread of the subdetectors and obtain synchronisation.

Chapter 9

DAQ

9.1 Requirements

The Data Acquisition of the TOTEM experiment will perform different tasks depending on the running conditions:

- Initialisation and calibration of the front-end hardware

- TOTEM stand-alone data taking at a rate ≈ 1 kHz;

- Data and Trigger quality monitoring;

- Data taking integrated in the CMS DAQ/Trigger system at a later stage.

9.1.1 Trigger and data rates

We consider that the upper limit of the total event size is ≈ 50 kB. This data size is fixed since no zero-suppression is applied to the data. This choice greatly simplifies the task of evaluating the data rates and the resources needed to cope with them.

The data rate is easily computed as $50\,\text{kB/event} \cdot \text{TriggerRate} = 50\,\text{MB/s} \cdot (\text{TriggerRate/kHz})$. We consider here that the standard trigger rate is 1 kHz, with an upper limit (on redundant resources) of 2 to 3 kHz.

Two operational conditions can be envisaged:

- Calibration and Setup. The VFAT chips and related front-devices need to be initialised and calibrated before a normal run can start. The parameter space of the VFAT chip is particularly large, and its calibration procedure delicate; many different parameters need to be scanned in order to compute the optimal setting in terms of threshold and latency adjustments, taking into account the specific properties of each detector in terms of signal shape and timing. In these operating conditions the rates are typically much lower than in standard running mode, the limiting factor being the time needed to re-configure all the VFAT chips at every step of the parameter scan. We assume that a typical trigger rate in this running mode will be ≈ 100 Hz, corresponding to ≈ 5 MB/s

- Once the system is properly calibrated and initialized with the computed parameters, the standard running mode can be started, and the data rate will solely be tuned by the trigger rate.

In both cases the data produced by the VFATs will flow through an infrastucture based on VME [56] and/or USB-2 (Universal Serial Bus) [61] links, independently from the one of the CMS experiment.

Irrespectively of the running mode (*standalone* or *CMS*) this *local DAQ* will always be used for setup and calibration.

9.1.2 CMS compatibility

In the special *CMS compatible* running mode, the raw data will flow through the CMS standard S-Link64 [58] lines, FRL boards and Myrinet infrastructure. The TOTEM FED boards (section 7.2.2) have been designed (as described in the relevant sections) to respect the CMS standard data format and control protocols when connected to the main CMS DAQ.

In this running mode, the *local* readout infrastructure will act as a parallel path, used for front-end initialization during the start-of-run procedures, and for data quality monitoring.

The TOTEM DAQ software is based on the same building blocks as the one of CMS. This will simplify the task of operating the TOTEM Run Control (and its end- and start-of-run procedures) system within the CMS one.

9.2 Implementation: readout chain and infrastructure

9.2.1 Readout link options

The TOTEM FED boards offer a large range of readout options.

- VME: We assume that the aggregated maximum data rate per VME crate is $\approx 40\,\mathrm{MB/s}$. Readout load splitting over > 1 VME crates is possible.
  VME is the standard communication link for hardware initialization. We decided to use a minimum 3 crates dedicated to readout FEDs to ease standalone operations of the 3 detectors during setting-up periods. One additional crate hosts the trigger FEDs. In these conditions, the minimal requirement of 1 kHz trigger is already largely satisfied.

- USB-2: Every FED carries 3 USB-2 links. If we assume the USB-2 standard to be capable of $10\,\mathrm{MB/s}$, the maximum aggregated data rate over the 20 available raw-data links amounts to $200\,\mathrm{MB/s}$, corresponding to a theoretical 4 to 5 kHz trigger rate. These numbers are challenging (although not impossible) at several levels of the DAQ system, from data transmission over the Ethernet network, to stress (and cost) of the storage system, to data mirroring in the Central Data Recording facilities. Full exploitation of these capabilities is out of the scope of the present activities, and therefore not foreseen for the moment. Suffice here to say that the TOTEM DAQ has abundant spare resources to accomodate the foreseen trigger rates.

- S-Link: This can be considered either an electrical connection to a front-end PC (useful for laboratory testing) or the entry point into the main CMS DAQ data transport via FRL boards and the Myrinet infrastructure. It is the default option for the integration of TOTEM into the CMS DAQ and Trigger system.

9.2.2 PC cluster and local data storage

The TOTEM DAQ cluster will consist of a set of a few PCs (presently 5) for raw data readout over VME (or optionally USB), and a set of event-building and storage nodes sized to the needed storage rate and capacity.

The mimimum requirements for data storage is the ability to write data at the trigger rate of 1 to 2 kHz and the capacity to store data during one full day even in case of failure of data transfer to a central data recording system.

At the rate of 2 kHz, TOTEM will produce $\approx 360\,GB\,/\,h$, corresponding to $\approx 8.6\,TB$ of data per day of running. These capacities and rates can be easily accomodated in present medium-level storage systems based on Fiber-Channel [62] or iSCSI [63] technology. To ensure that the required rate is attained and to provide redundancy, the data load will be shared between ≥ 2 storage systems.

Chapter 10

Detector Control System

10.1 Objectives

The Detector Control Systems (DCS) for LHC experiments are the evolution of slow control systems of the LEP era. Their aim is to permit the physicist on shift to operate and control various detector subsystems such as high and low voltage power supplies, gas circulation systems, cooling and so on, and monitor their performance as well as various relevant environmental parameters, for example temperature and radiation levels. All DCS systems of LHC experiments are built using the industrial PVSS control supervisory software running on networks of PCs (Windows and/or Linux), augmented with modules developed at CERN for typical HEP control functions and equipment, the JCOP framework. "Big.brother", the TOTEM DCS system, also uses the same guidelines, technology, tools and components.

10.2 Constraints

The TOTEM detector is located at the CMS intersection of the CERN LHC accelerator, and CMS and TOTEM also have a common physics program, so that TOTEM must be able to operate independently, but also take data together with CMS. For this reason TOTEM adopted a number of technological and organisational solutions that will permit interoperability at the level of electronics, DAQ, run control, offline data processing and so on. In the same fashion, the TOTEM detector control system is developed in the framework of the CMS DCS. This implies following the CMS DCS integration rules [64], liaising with CMS central controls, through participation in the CMS DCS coordination board, and adopting the same model of rack-mounted PCs.

10.3 Equipment under control

The three TOTEM subdetectors, Roman Pot silicon detectors, T1 and T2, require the monitoring and control of the usual equipment found around particle physics experiments. All three use CAEN HV power supplies, Wiener Maraton LV units, Wiener VME crates, and environmental sensors connected to ELMBs or read from the DAQ through the DCU technology. T1 and T2 are cooled with cold water loops derived from CMS rack cooling, while the Roman Pot Si detectors use a
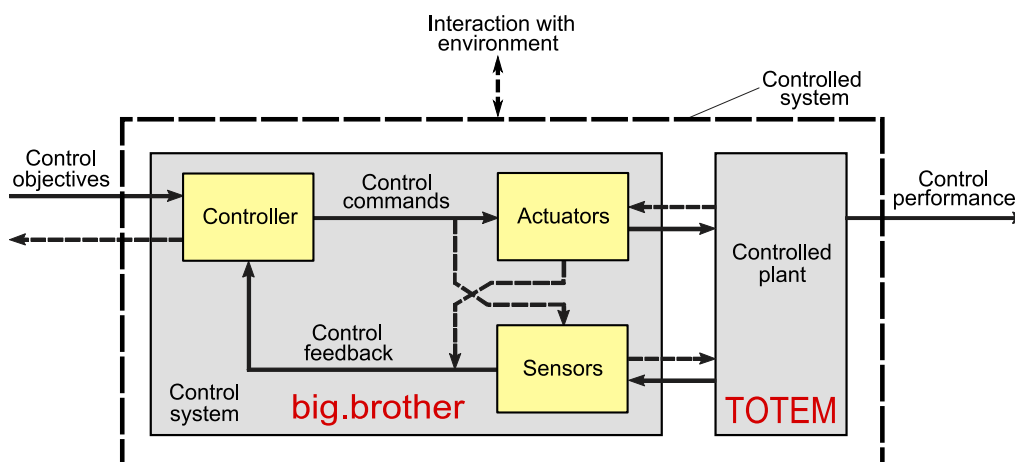
Figure 10.1: Generic control structure (adapted from [67], figure 1).

more sophisticated cooling plant. The T1 and T2 gas systems are subcontracted, including a PC running PVSS control software compliant with the GCS standard LHC gas control system [65].

The Roman Pot motor system is derived from the one of the LHC collimators, and so is the corresponding control system [66]. The front-end is based on National Instruments hardware and the Labview RealTime software, adapted to the selected sensors, and is subcontracted to PH/DT1. The high level control is also subcontracted, being derived from the Collimator Supervisory System, is integrated with the Central Collimation Application in the main control room, and sends status data and other relevant information to big.brother.

10.4 Engineering

Dealing with control, the system conforms to the standard control model of sensors, actuators and controllers depicted in figure 10.1.

The system consists of HW and SW components, therefore it requires comprehensive system engineering. As with any control system, the development process of big.brother is iterative vertically between system engineering and lower assembly engineering, and iterative horizontally between requirements engineering, design-configuration, verification-validation, and analysis (figure 10.2).

A number of HW and SW technologies have been defined already before the project started: sensors, front-end systems, the supervisory level based on PVSS and the JCOP Framework, the model of the PCs and their operating system.

The CMS DCS development model is federal, with independent subdetectors following their own engineering and project organisation, so far that as they use the agreed technology and obey the mandatory integration rules, dealing also with the definition and nesting of Finite States Machines (FSM) describing the state of the system. The situation is very different in ALICE, where the development model is centralised, and a number of engineering representations and software components have been developed centrally to be used by all subdetectors [68]. Big.brother has
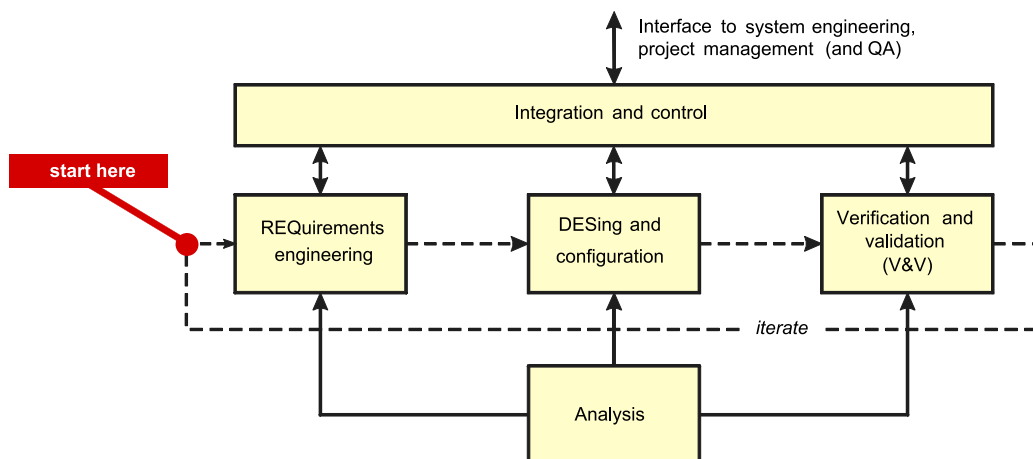
**Figure 10.2**: Horizontal development iteration.

adopted from ALICE DCS the requirements template, the format of the HW overview diagrams, and is considering to use some of the existing components, also for the user interface which is standardised across the three TOTEM subdetectors.

10.5 The Radiation Monitoring system —
an example of environmental monitoring

The Roman Pot silicon detectors, T1 and T2 together with their related readout electronics, are located in LHC areas where high radiation levels are expected (see for example figure 5.1 and ref. [69]). For this reason, the Total Ionising Dose (TID) and the 1-MeV neutron equivalent particle fluence (Φ_{eq}) will be monitored during operation in various locations of the TOTEM experiment, and they will be available on-line in the TOTEM DCS [70].

Measurements of TID and Φ_{eq} are needed to understand the radiation-induced changes on the detector performances, to survey the radiation damage on electronic components, to verify the TOTEM radiation field simulated with Monte Carlo codes and to survey anomalous increases of radiation levels that may arise from accidental radiation burst such as beam losses or unstable beams. This set of information can finally be used to better plan the detector operation scenario.

The basic unit of the TOTEM Radiation Monitoring (RADMON) system is the Integrated Sensor Carrier (ISC) that hosts radiation sensors connected to the electronics via readout cables. TID measurements are performed with different types of Radiation-sensing Field Effect Transistors (RadFETs), while Φ_{eq} measurements are performed with forward biased *p-i-n* diodes [71]. In both cases the dosimetric parameter (voltage) is measured upon constant current injection through the sensors. Selection of sensors, assembly of the ISC, as well as calibration constants are provided by the TS-LEA and PH-DT2 groups at CERN [72]. In the case of TOTEM each ISC will host four radiation sensors and a temperature probe, leading to a total of five channels to be read out per monitoring location.
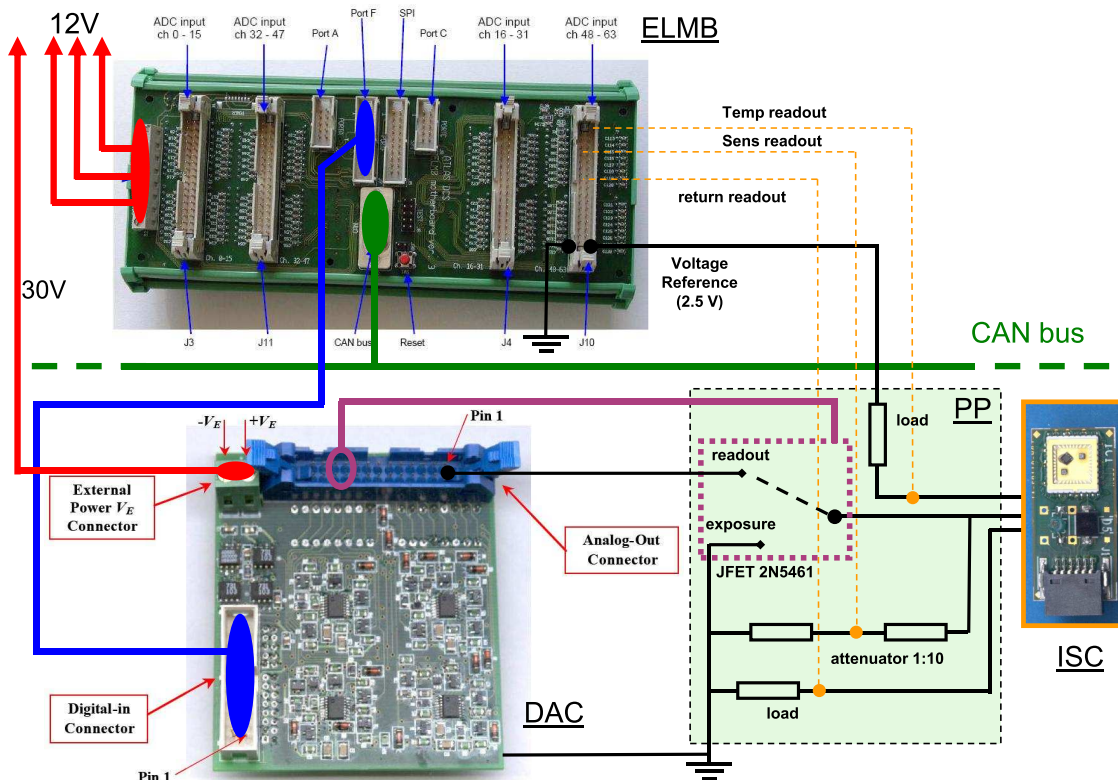
Figure 10.3: Schematic of the ELMB RADMON readout system used in TOTEM and based on the standard ATLAS electronics. This example of readout is referred to one ISC hosting 1 RADMON sensor and 1 temperature probe. On the right-hand side of the picture the ISC is visible. The readout current injected through each sensor is also monitored by measuring the voltage drop on a small resistor placed on the return line.

The design of the RADMON readout electronics in TOTEM follows the one developed by the ATLAS experiment where the sensor readout is based on Embedded Local Monitor Boards (ELMBs) [73]. As shown in figure 10.3, the readout of the ISC is based on an ELMB board, which communicate over the CAN bus with a PC running SCADA software (PVSSII) that is linked to the DCS. To drive currents through the sensors on the ISC during the readout sequence, ELMB-DAC boards are needed. The 16 channel, 12-bit DAC-module connects directly to the digital output of the ELMB motherboard. The ELMB and the ELMB-DAC finally interface with the ISC via patch panel (PP) boards. The PP host a series of JFET switches to short the sensor terminals to ground during radiation exposure and enable them for the readout. On the PP, voltage attenuators and loads to monitor the readout current sent to the radiation sensors are also present. One full readout chain consisting of 1 ELMB, 2 ELMB-DAC and 2 PP boards allows the readout of 6 ISCs in the TOTEM configuration. A total of 36 ISCs will be installed in the TOTEM experiment: one ISC will be integrated on each of the 24 RP motherboards, while 8 ISCs will be installed around T1 and 4 around T2 respectively.

Acknowledgements

TOTEM acronym list

AFEC	Anode Front-End Card of T1
BC0	Bunch Crossing Zero
BPM	Beam Position Monitor
CC	Coincidence Chip
CCMC	Coincidence Chip Mezzanine Card
CCU	Communication and Control Unit
CCUM	Communication and Control Unit Module
CFEC	Cathode Front-End Card of T1
CMM	Coordinate Measuring Machine
CNC	Computer Numerical Control
CSC	Cathode Strip Chamber
CTR	Current Terminating Ring
CTS	Current Terminating Structure
DAC	Digital-to-Analog Converter
DCS	Detector Control System
DCU	Detector Control Unit
DD	Double Diffraction
DOH	Digital Opto-Hybrid
DOHM	Digital Opto-Hybrid Module
DPE	Double Pomeron Exchange or central diffraction
ELMB	Embedded Local Monitor Board
ENC	Equivalent Noise Charge
FEC	Front-End Controller
FED	Front-End Driver
FRL	Front-End Readout Link
FPGA	Field-Programmable Gate Array
GEM	Gas Electron Multiplier
GOH	Gigabit Optical Hybrid
I^{2}C	Inter-Integrated Circuit (multi-master serial computer bus used to attach low-speed peripherals to a motherboard)
IP	Interaction Point
LVDS	Low-Voltage Differential Signalling
PCB	Printed Circuit Board

PT100	Platinum (Pt) resistance thermometer with a resistance of $100\,\Omega$ at $0°\text{C}$
ROC	Read-Out Card
RP	Roman Pot
RP Unit	Ensemble of 2 vertical and 1 horizontal RP
RP Station	Ensemble of 2 RP Units
SCR	Slow Control Ring
SD	Single Diffraction
SEU	Single Event Upset
TDC	Time-to-Digital Converter
TTC	Timing, Trigger and Control
VFAT	Historical name inherited from the predecessor chip: Very Forward ATLAS and TOTEM chip
VTM	VFAT Trigger Mezzanine

Bibliography

[1] TOTEM collaboration, V. Berardi et al., *Total cross-section, elastic scattering and diffraction dissociation at the Large Hadron Collider at CERN: TOTEM technical design report*, CERN-LHCC-2004-002, http://cdsweb.cern.ch/record/704349; *Addendum* CERN-LHCC-2004-020, http://cdsweb.cern.ch/record/743753.

[2] THE CMS AND TOTEM DIFFRACTIVE AND FORWARD PHYSICS WORKING GROUP, M. Albrow et al., *Prospects for diffractive and forward physics at the LHC*, CERN-LHCC-2006-039, http://cdsweb.cern.ch/record/1005180.

[3] CDF collaboration, F. Abe et al., *Measurement of the antiproton-proton total cross section at $\sqrt{s} = 546$ and $1800\,GeV$*, *Phys. Rev.* **D 50** (1994) 5550.

[4] E710 collaboration, N.A. Amos et al., *Measurement of the $\bar{p}p$ total cross section at $\sqrt{s} = 1.8\,TeV$*, *Phys. Rev. Lett.* **63** (1989) 2784;
E710 collaboration, N.A. Amos et al., *A luminosity independent measurement of the $\bar{p}p$ total cross-section at $\sqrt{s} = 1.8\,TeV$*, *Phys. Lett.* **B 243** (1990) 158;
E811 collaboration, C. Avila et al., *A measurement of the proton-antiproton total cross-section at $\sqrt{s} = 1.8\,TeV$*, *Phys. Lett.* **B 445** (1999) 419;
E 811 collaboration, C. Avila et al., *The ratio, ρ, of the real to the imaginary part of the $\bar{p}p$ forward elastic scattering amplitude at $\sqrt{s} = 1.8\,TeV$*, *Phys. Lett.* **B 537** (2002) 41.

[5] J.R. Cudell et al., *Benchmarks for the forward observables at RHIC, the Tevatron-Run II, and the LHC*, *Phys. Rev. Lett.* **89** (2002) 201801.

[6] TOTEM collaboration, K. Eggert et al., *TOTEM Physics*, *Proceedings of* 17th *rencontre de Blois:* 11th *International Conference on Elastic and Diffractive Scattering*, Château de Blois France (2005), hep-ex/0602025.

[7] M.M. Islam, R.J. Luddy and A.V. Prokudin, *Near forward pp elastic scattering at LHC and nucleon structure*, *Int. J. Mod. Phys.* **A 21** (2006) 1;
C. Bourrely, J. Soffer and T.-T. Wu, *Impact-picture phenomenology for $\pi^{\pm}p, K^{\pm}p$ and $pp, \bar{p}p$ elastic scattering at high energies*, *Eur. Phys. J.* **C 28** (2003) 97;
V.A. Petrov, E. Predazzi and A. Prokudinl, *Coulomb interference in high-energy pp and $\bar{p}p$ scattering*, *Eur. Phys. J.* **C 28** (2003) 525;
M.M. Block, E.M. Gregores, F. Halzen and G. Pancheri, *Photon proton and photon photon scattering from nucleon nucleon forward amplitudes*, *Phys. Rev.* **D 60** (1999) 054024.

[8] G.B. West and D. Yennie, *Coulomb interference in high-energy scattering*, *Phys. Rev.* **172** (1968) 1413.

[9] V. Kundrát, J. Kašpar and M. Lokajíček, *To the theory of high-energy elastic nucleon collisions*, *Proceedings of the Blois'07/EDS07 Workshop on Elastic and Diffractive Scattering*, Hamburg Germany (2007), arXiv:0712.1503.

[10] U. Amaldi et al., *The energy dependence of the proton proton total cross-section for center-of-mass energies between 23 and 53 GeV*, *Phys. Lett.* **B 44** (1973) 112.

[11] TOTEM collaboration, M. Deile et al., *Tests of a Roman Pot prototype for the TOTEM experiment*, *Proceedings of the 2005 Particle Accelerator Conference*, Knoxville, Tennessee U.S.A. (2005), arXiv:physics/0507080v1 [physics.ins-det];
M. Deile et al., *Beam Coupling Impedance Measurement and Mitigation for a TOTEM Roman Pot*, Proceedings of the *11th European Particle Accelerator Conference (EPAC08)*, Genova, Italy (2008), arXiv:0806.4974v1 [physics.ins-det].

[12] V. Avati et al., *First test of cold edgeless silicon microstrip detectors*, *Nucl. Instrum. Meth.* **A 518** (2004) 264.

[13] G. Ruggiero et al., *Planar edgeless silicon detectors for the TOTEM experiment*, *IEEE Trans. Nucl. Sci.* **52** (2005) 1899.

[14] E. Noschis, V. Eremin and G. Ruggiero, *Simulations of planar edgeless silicon detectors with a current terminating structure*, *Nucl. Instrum. Meth.* **A 574** (2007) 420.

[15] ISE Integrated Systems Engineering AG release 6, online at www.ise.ch.

[16] V. Vacek, G. Hallewell, S. Ilie and S. Lindsay, *Perfluorocarbons and their use in cooling systems for semiconductor particle detectors*, *Fluid Phase Equilibr.* **174** (2000) 191.

[17] E. Noschis et al., *Final size planar edgeless silicon detectors for the TOTEM experiment*, *Nucl. Instrum. Meth.* **A 563** (2006) 41.

[18] L. Jones, *APV25-S1 user guide version 2.2*,
http://www.ins.clrc.ac.uk/INS/Electronic_Systems/
Microelectronics_Design/Projects/High_Energy_Physics/CMS/APV25-S1/index.html.

[19] G. Ruggiero et al., *Planar edgeless silicon detectors for the TOTEM experiment*, *Nucl. Instrum. Meth.* **A 582** (2007) 854.

[20] H.W. Kraner, Z. Li and K.U. Posnecker, *Fast neutron damage in silicon detectors*, *Nucl. Instrum. Meth.* **A 279** (1989) 266.

[21] TOSTER project, *INTAS collaborative call with CERN 2005*, INTAS Ref. Nr. 05-103-7533.

[22] C. Kenney et al., *Active-edge planar radiation sensors*, *Nucl. Instrum. Meth.* **A 565** (2006) 272.

[23] S.I. Parker, C.J. Kenney and J. Segal, *3D — A proposed new architecture for solid state radiation detectors*, *Nucl. Instr. Meth.* **A 395** (1997) 328;
C.J. Kenney, S.I. Parker, J. Segal and C. Storment, *Silicon detectors with* 3D *electrode arrays fabrication and initial test results*, *IEEE Trans. Nucl. Sci.* **46** (1999) 1224;
C.J. Kenney, S.I. Parker and E. Walckiers, *Results from 3D silicon sensors with wall electrodes: near-cell-edge sensitivity measurements as a preview of active-edge sensors*, *IEEE Trans. Nucl. Sci.* **48** (2001) 2405.

[24] C. Da Vià et. al, 3*D active edge silicon detector tests with* 120 *GeV muons*, submitted to *IEEE Trans. Nucl. Sci.*.

[25] S. Parker and C. Kenney, *Performance of 3-D architecture silicon sensors after intense proton irradiation*, *IEEE Trans. Nucl. Sci.* **48** (2001) 1629;
C. Da Vià and S. Watts, *Can silicon detectors survive beyond* 10^{15} *neutrons* cm^{-2}?, *Nucl. Instrum. Meth.* **A 501** (2003) 138;
C. Da Vià et al., *Advances in silicon detectors for particle tracking in extreme radiation environments*, *Nucl. Instrum. Meth.* **A 509** (2003) 86;
C. Da Vià et al., *Radiation hardness properties of full-3D active edge silicon sensors*, *Nucl. Instrum. Meth.* **A 587** (2008) 243.

[26] *NEEDS Workshop Discussion* in *Very High Energy Cosmic Ray Interactions*:
L.W. Jones, *Introduction to the discussion of the "NEEDS" workshop*, Nucl. Phys. B (Proc. Suppl.)**122** (2003) 433;
R. Engel, *Extensive air showers and accelerator data — the NEEDS workshop*, Nucl. Phys. B (Proc. Suppl.)**122** (2003) 437;
K. Eggert, *The TOTEM/CMS forward experiment at the LHC*, Nucl. Phys. B (Proc. Suppl.)**122** (2003) 447;
D. Heck, *Importance of forward interactions for cosmic ray air shower simulations*, Nucl. Phys. B (Proc. Suppl.)**122** (2003) 451;
R. Jörg and R. Hörandel, *Test of high-energy hadronic interaction models with KASCADE — Particle physics with air shower detectors*, Nucl. Phys. B (Proc. Suppl.)**122** (2003) 455;
G. Schatz, *Summary of the NEEDS workshop*, Nucl. Phys. B (Proc. Suppl.) **122** (2003) 462;
Proceedings of 12th International Symposium on Very High-Energy Cosmic Ray Interactions (ISVHECRI 2002), Geneva, Switzerland, 15-20 July (2002), [NEEDS workshop: http://www-ik.fzk.de/∼needs].

[27] G. Bencze et al., *Position and timing resolution of interpolating cathode strip chambers in a test beam*, *Nucl. Instrum. Meth.* **A 357** (1995) 40.

[28] M. Huhtinen, *Radiation levels at detector*, *Presentation at TOTEM T* 1 *CSC engineering design review*, 7 March 2006, CERN, Switzerland, http://indico.cern.ch/conferenceDisplay.py?confId=a061338.

[29] D. Acosta et al., *Aging tests of full-scale CMS muon cathode strip chambers*, *Nucl. Instrum. Meth.* **A 515** (2003) 226, Fermilab-Conf-03-307, http://cdsweb.cern.ch/record/808006.

[30] ATLAS collaboration, *ATLAS muon spectrometer: Technical Design Report*, CERN-LHCC-97-022 chapter 6, http://cdsweb.cern.ch/record/331068.

[31] CMS collaboration, *The CMS muon project: Technical Design Report*, CERN-LHCC-97-032, http://cdsweb.cern.ch/record/343814.

[32] LHCB collaboration, P.R. Barbosa-Marinho et al., *LHCb technical design report* 4, CERN-LHCC-2001-010, http://cdsweb.cern.ch/record/504326.

[33] S. Minutoli, *TOTEM T1 electronics system*, *Presented at the TOTEM T1 CSC engineering design review*, 7 March 2006, CERN, Switzerland, http://indico.cern.ch/conferenceDisplay.py?confId=a061338.

[34] P. Moreira et al., *A Radiation Tolerant Gigabit Serializer for LHC data Transmission*, 7th *Workshop on Electronics for LHC Experiments*, Stockholm Sweden (2001), http://cdsweb.cern.ch/record/588665; J. Grahl, *GOL Opto-Hybrid Manufacturing Specifications*, v. 3.30, CERN-CMS ECAL (2003).

[35] CMS TRACKER collaboration, *CMS Tracker control link specification. Part 2: front-end digital optohybrid*, CERN EP/CME, CERN EDMS document archive CMS-TK-ES-0019, version 2.2.

[36] C. Paillard et al., *The CCU25: a network oriented communication and control unit integrated circuit in a* $0.25\mu m$ *CMOS technology*, 8th *Workshop on Electronics for LHC Experiments*, Colmar France (2002), http://cdsweb.cern.ch/record/593914.

[37] L.S. Durkin, *CMS muon endcap cathode FE board — Electronic system review*, CERN, Switzerland, 18 September 2000.

[38] G. Antchev et al., *A data readout module for the TOTEM experiment*, *Proceedings of NEC2005*, Varna, Bulgaria (2005), http://cdsweb.cern.ch/record/1069893.

[39] A. Marchioro et al., *A PLL-delay ASIC for clock recovery and trigger distribution in the CMS tracker*, 3rd *Workshop on Electronics for LHC Experiments*, London U.K. (1997). P. Moreira et al., *CMS Tracker PLL Reference Manual - v. 2.1*, CERN - EP/MIC, July 2000, http://cdsweb.cern.ch/record/1069705.

[40] CAEN s.p.a., *MOD. A1550: 24 channel 5kV/1mA common floating RTN board, technical information manual - rev 0*, 6 July 2007.

[41] CAEN s.p.a., *MOD. SY1527: Universal Multichannel Power Supply System, User Manual-rev.13*, 6 October 2005.

[42] WIENER GmbH, *MARATHON Power Supply System, Technical Manual — v. 00691.A0*, 20 June 2006.

[43] F. Sauli, *GEM: A new concept for electron amplification in gas detectors*, *Nucl. Instrum. Meth.* **A 386** (1997) 531.

[44] C. Altunbas et al., *Construction, test and commissioning of the triple-GEM tracking detector for compass*, *Nucl. Instrum. Meth.* **A 490** (2002) 177;
B. Ketzer et al., *Performance of triple GEM tracking detectors in the COMPASS experiment*, *Nucl. Instrum. Meth.* **A 535** (2004) 314.

[45] M. Alfonsi et al., *High-rate particle triggering with triple-GEM detector*, *Nucl. Instrum. Meth.* **A518** (2004) 106.

[46] H. Andersson et al., *Analysis of compounds released from various detector materials and their impact on aging characteristics of proportional counters*, *IEEE Trans. Nucl. Sci.* **51** (2004) 2110.

[47] The MAD-X program, Methodical Accelerator Design, http://www.cern.ch/mad.

[48] H. Niewiadomski, *Reconstruction of proton tracks in the TOTEM Roman Pot detectors at the LHC*, PhD Thesis, University of Manchester, U.K. (2008).

[49] LHC Layout, http://www.cern.ch/lhclayout/.

[50] M. Deile, *Algebraic determination of Roman Pot acceptance and resolution for the $\beta^* = 1540\,m$ optics*, TOTEM Note 2006-002.

[51] J. Kašpar, *Reconstruction of elastic events*, TOTEM Note 2007-007.

[52] P. Aspell et al., *VFAT2: a front-end system on chip providing fast trigger information, digitized data storage and formatting for the charge sensitive readout of multi-channel silicon and gas particle detectors*, *Proceedings of TWEPP-07, Topical Workshop on Electronics for Particle Physics*, Prague Czech Republic (2007), http://cdsweb.cern.ch/record/1069906.

[53] http://www.cern.ch/TTC/intro.html;
J. Troska et al., *Implementation of the timing, trigger and control system of the CMS experiment*, *IEEE Trans. Nucl. Sci.* **53** (2006) 834.

[54] F. Drouhin et al., *The control system for the CMS tracker front-end*, *IEEE Trans. Nucl. Sci.* **49** (2002) 846.

[55] G. Antchev et al., *The TOTEM front end driver, its components and applications in the TOTEM experiment*, *Proceedings of TWEPP-07, topical workshop on electronics for particle physics*, Prague Czech Republic (2007), http://cdsweb.cern.ch/record/1069713.

[56] ITA, *VME technology specifications*, VME64x 9U × 400 mm Format, ANSI/VITA 1.3-1997 (R2003), http://www.vita.com/specifications.html.

[57] CMS collaboration, *The TriDAS project: Technical Design Report. Volume* 2: *data-acquisition and high-level trigger*, CERN-LHCC-2002-026, http://cdsweb.cern.ch/record/578006.

[58] A. Racz et al., *The S-LINK* 64 *bit extension specification: S-LINK64*, CERN-EP-2003, http://cmsdoc.cern.ch/cms/TRIDAS/horizontal/docs/slink64.pdf.

[59] E. Noschis et al., *Protection circuit for the T*2 *readout electronics of the TOTEM experiment*, *Nucl. Instrum. Meth.* **A 572** (2007) 378.

[60] CMS collaboration, *CMS TriDAS project: Technical Design Report. Volume* 1*: the trigger systems*, CERN-LHCC-2000-038, http://cdsweb.cern.ch/record/706847.

[61] USB 2.0 specifications, http://www.usb.org/developers/docs/.

[62] Fiber Channel Tutorial, http://www.iol.unh.edu/services/testing/fc/training/tutorials/fc_tutorial.php.

[63] The iSCSI specification, http://tools.ietf.org/html/rfc3720.

[64] F. Glege, R. Gómez-Reino and J. Varela, *CMS DCS integration guidelines* 3.0, http://cmsdoc.cern.ch/cms/TRIDAS/DCS/central_dcs/guidelines.

[65] R. Barillère, *LHC gas control systems: a common approach for the control of the LHC experiments gas systems*, CERN-JCOP-2002-14, http://cdsweb.cern.ch/record/1070768; see also http://itcofe.web.cern.ch/itcofe/Projects/LHC-GCS.

[66] S. Redaelli, *Application software for the LHC collimators and movable elements*, CERN LHC-TCT-ES-0001, EDMS 826861, http://cdsweb.cern.ch/record/1070288.

[67] The European Cooperation for Space Standardisation, Space engineering - Control engineering, ECSS-E-60A ESA Publications (2004), http://www.ecss.nl.

[68] A. Augustinus, *ALICE DCS User Requirements Document*, http://alicedcs.web.cern.ch/AliceDCS/URD.

[69] N.V. Mokhov, I.L. Rakhno, J.S. Kerby and J.B. Strait, *Protecting LHC IP*1*/IP*5 *components against radiation resulting form colliding beam interactions*, LHC Project Report 633, http://citeseer.ist.psu.edu/609257.html.

[70] F. Ravotti et al., *Conception of an integrated sensor for the radiation monitoring of the CMS experiment at the large hadron collider*, *IEEE Trans. Nucl. Sci.* **51** (2004) 3642.

[71] F. Ravotti et al., *Radiation monitoring in mixed environments at CERN, from the IRRAD6 facility to the LHC experiments*, *IEEE Trans. Nucl. Sci.* **54** (2007) 1170.

[72] F. Ravotti, M. Glaser and M. Moll, *Sensor catalogue data compilation of solid-state sensors for radiation monitoring*, CERN-TS-NOTE-2005-002, http://cdsweb.cern.ch/record/835408.

[73] F. Ravotti, F. Lucas-Rodriguez and E. Dimovasili, *Technical and functional specification of the TOTEM on-line radiation monitoring system*, CERN EDMS 874945 https://edms.cern.ch/document/874945